Stars Versus Quasar Accretion Disks

The Effects of Stars Striking the Accretion Disks of Active Galactic Nuclei

Lucas Seaton

A Thesis submitted to the Faculty of Graduate Studies in Partial Fulfillment of the Requirements for the Degree of Master of Science

Graduate Program in Physics & Astronomy

York University, Toronto, Ontario

April 2023

Abstract

This thesis investigates the astrophysical effects of stars colliding with the accretion disks of supermassive black holes (SMBH) in active galactic nuclei (AGN). In this work, we model the AGN to have a thin accretion disk surrounded by a stellar nuclear cluster (SNC) containing stars on various orbital eccentricities and inclination angles striking the disk at periapse. An impacting star carves a tilted cylindrical tunnel out of the disk material and loses up to $6 \times 10^{-4}\%$ of its stellar mass. The time-averaged collisional luminosity is at most 10^{-2} times the entire disk's expected luminosity, while the emission profile of an impact site initially flares before quickly dimming to the brightness of the local disk. The parameters of the SMBH, accretion disk, SNC, and impacting stars are altered to reveal that star-disk collisions from a densely populated SNC can outshine the disk luminosity.

Contents

List of Tables

List of Figures

1 Introduction

Active galactic nuclei (AGNs or quasars) are a class of astronomical phenomena that reveal themselves through the spectral properties of the centres of more massive galaxies, and have been observed out to redshifts[1] of $z \leq 7.5$ (Bañados et al., 2018; Wang et al., 2021).

Supermassive black holes (SMBHs) exist at the centres of most massive galaxies (Kormendy & Ho, 2013). Those found in AGNs have masses typically ranging from $M_\bullet \sim 10^6 - 10^{10}\ M_\odot$ (e.g. Trakhtenbrot, 2021) and rarely $M_\bullet \sim 10^{12}\ M_\odot$ found in over-massive host galaxies (Hu et al., 2022).

As matter approaches the SMBH it forms a rotating gaseous disk that transports matter radially inwards and transfers angular momentum outward (Osterbrock, 1989). The conversion of some gravitational potential energy to thermal emission through viscous heating causes the disk to have a range of temperatures $T_\mathrm{d} \sim 10^3 - 10^5$ K (see §4 for calculations of the Shakura & Sunyaev (1973) disk model) that results in a strong continuum emission over a wide range of wavelengths. The area of the disk is roughly the size of our solar system, making quasars very luminous (e.g. Schindler et al., 2021).

Although the exact mechanisms underlying accretion onto the SMBH are not fully understood, different models for accretion disks have been proposed (e.g. Shakura & Sunyaev, 1973; Novikov & Thorne, 1973; Huré, 1998; Frank et al., 2002; Goodman, 2003; Gilbaum & Stone, 2022). All proposed models include a disk-like plane of gas orbiting a central compact object.

Infalling clouds of matter form accretion disks around SMBH systems (e.g. Goicovic et al., 2016; Hopkins et al., 2016). The SMBH of the supergiant elliptical galaxy in the

[1] Cosmological redshift is an increase in the wavelength of radiation due to the expansion of space,

$$z = \frac{\lambda_\mathrm{obsv} - \lambda_\mathrm{emit}}{\lambda_\mathrm{emit}} \tag{1.1}$$

where λ_obsv is the observed wavelength and λ_emit is the wavelength emitted by the source.

Virgo constellation, M87, was observed by the Event Horizon Telescope in early 2019 (Event Horizon Telescope Collaboration et al., 2019a). Also, the SMBH of Sagittarius A*, at the center of our galaxy, was imaged in the early months of 2022 (Event Horizon Telescope Collaboration et al., 2022). In both instances there appears to be a bright ring-like structure orbiting the BHs, that spans $\sim$ 50 micro-arcseconds (or $\sim 4R_{\rm Sch} = 7.3\times10^{15}$ cm) for the image of M87 (Event Horizon Telescope Collaboration et al., 2019b). This is observational evidence of SMBHs, but the ring-like structure of Sagittarius A* is too small and dim to be an accretion disk on par with those in AGNs, like M87.

Quasars have been observed to vary in their luminosity over time, with some absorption fluctuations spanning years and others only a few hours (e.g. Filiz Ak et al., 2013; Grier et al., 2015; Rogerson et al., 2018). Optical emission from the continuum region in AGN has observed variability of $\sim 0.1 - 10\%$ (Smith et al., 2018), and a collection of quasars at $z \lesssim 2.8$ have observed light curves spanning $\sim$ 7.5 years that exhibit much greater luminosity variations of $10^{42} \lesssim \lambda L_\lambda(5100\text{Å}) \lesssim 10^{46}$ (Kelly et al., 2009) [2]. Some quasars, known as 'changing look' quasars (CLQs), show extreme variability resulting in the transition from type 1 to type 2 AGN, where the former shows strong broad emission lines and continuum emission and the latter does not. The variability in CLQs, such as GSN 069 that exhibits quasi-periodic eruptions (QPEs, or flares), has been suggested to be due to an unstable zone within the disk that is dominated by radiation pressure and gives rise to disk instability (Pan et al., 2022).

Flares could also occur due to tidal disruption events (TDEs) (e.g. Sun et al., 2020), the accretion disk transitioning between a thermal state (geometrically thin and optically thick) to a hard state (geometrically thick and optically thin) (e.g. Cho & Narayan, 2022), or stars impacting the disk (Zentsova, 1983). Flares caused by star-disk impacts happen locally within the disk and could account for some of the variability, however the

[2]The specific luminosity, L_λ, is the luminosity per unit wavelength, λ, and is measured in units of erg/s/Å. Multiplying the specific luminosity at a given wavelength by that wavelength yields a reasonable approximation of the luminosity of the astronomical object.

exact level has not been characterized nor has its dependence on host galaxy mass and accretion disk properties. Thus, we want to test the hypothesis that stellar collisions with the accretion disk can account for temporal brightening of the accretion disk.

To help create a stellar nuclear cluster (SNC), which populates a quasar's host galaxy with stars around the central SMBH, globular clusters could inspiral to the center of a galaxy or be formed within the nucleus (Neumayer et al., 2020). Supermassive stars can also form within the disk (Goodman & Tan, 2004). Theoretical investigations have proposed that the density profile of the SNC could, in principle, affect the overall spectrum of AGNs (Perry & Williams, 1993).

Stars on orbits that are sufficiently close to the SMBH (but not so close that they are torn apart by the SMBH or plunge into it) will interact with the disk by passing through it at high velocity (Pariev & Colgate, 2007). The loss of velocity that a star (hereafter impactor) undergoes with each crossing of the accretion disk, results in a new orbital trajectory for the star bringing it closer to the central SMBH. This can either cause the impactor to strike the accretion disk (twice per orbit) at a different radial location than its previous pericentre and apocentre (Dai et al., 2010), cause the impactor to pass through the SMBH's event horizon, or ultimately destroy the impactor from tidal disruption events. Throughout this thesis, we consider either an impactor striking the disk once or many impactors striking the disk once during a given span of time.

As the impactor passes through the disk it initially strikes the gas with a velocity that is greater than its sound speed. A shock wave is formed and energy is deposited in the local region, resulting in a bright spot (flare) on the disk, that is roughly the size of the impactor. The energy released during the passage increases the temperature of the spot to temperatures greater than the star's surface temperature, causing the spot to appear brighter than the interacting star (Zentsova, 1983). The energy released by the impact could account for X-ray flares observed in the accretion disks of nearby black holes (BHs)

(Nayakshin et al., 2004), and quasi-periodic eruptions (QPEs) observed in 4 epochs of the Seyfert galaxy GSN069 (Miniutti et al., 2019) could be driven by repeated collisions with the core of a star that survived a TDE (Xian et al., 2021; King, 2020).

A region of the disk is carved out by the transiting star (hereafter referred to as the 'shock tunnel') as it shock heats the gas. Eventually this tunnel is filled in by hydrodynamical forces. Photons that are released by the shocked gas must travel through the optically thick disk to arrive at the surface of the disk where they can be observed.

When a star passes through an accretion disk, some of its orbital velocity is lost to the disk and some of the disk's velocity is imparted onto the star. The orbital energy released by the impactor can cause highly eccentric orbits to become more circularized (MacLeod & Lin, 2020) and over time, enough azimuthal velocity can be given to the impactor so that it ends up co-rotating with the disk (Fabj et al., 2020). These impactors experience a drag force as they repeatedly slam into the accretion disk, that can be quantified to determine how long they take to be captured by the disk given their initial inclination, eccentricity, and semi-major axis (Fabj et al., 2020).

Since interacting stars' orbits evolve to lie in the plane of the disk, stars could potentially exist within the disk. This is dependent on the rate at which stars are "captured" by the disk and how quickly they migrate towards the central SMBH. The disk gravitationally perturbs the stars causing them to migrate until they get trapped at specific radii where the gas torque changes sign (Bellovary et al., 2016). The stars will also perturb the gas of the disk as they collide with it and are brought into the disk plane, and these co-orbiting stars will further perturb the disk structure (Goodman & Tan, 2004).

Impacts involving black holes have been studied before (e.g. Pihajoki, 2016), and there is extensive work in the literature on stars and BHs embedded within accretion disks, some of which is listed below. Captured stellar mass BHs can eventually displace radiation, winds and supernovae from massive stars as the dominant feedback source (Gilbaum &

Stone, 2022). Embedded stars could accrete hydrogen from the disk material faster than their cores burn it into helium, effectively keeping them in the hydrogen burning stage (Jermyn et al., 2022). Embedded stars can also migrate towards the inner disk from binary interactions with other stars leading to TDEs that create optical/UV flares (McKernan et al., 2021). These binary mergers could lead to detectable gravitational waves once the large interferometer space array (LISA) is launched (e.g. McKernan et al., 2020). However, black hole impactors and embedded objects are not the focus of this research.

This work will: (1) investigate the effects of stars impacting the disk, (2) provide models for the accretion disk, collision, and shock tunnel geometry, (3) Estimate the temporal flare profile of a transiting star, and (4) explore extreme scenarios by altering parameters affecting the SMBH, accretion disk, SNC, and the impactors. It will not: (1) consider relativistic effects, although they have an effect in the regions of space near the central SMBH, (2) consider hydrodynamical forces in depth, that the disk matter will experience as an impactor passes through it, (3) consider any magnetic fields that arise from the movement of the protons and electrons that the disk plasma is composed of, and (4) consider spinning black holes.

The preliminary parameters will be outlined in §2, and the SNC and accretion disk models will be provided in §3 and §4, respectively. As the star plunges through the accretion disk its less dense outer atmosphere is stripped off by the more dense gaseous disk matter and its residual atmosphere pushes some of the disk material out, all of which is quantified in §5. In §6 we investigate the luminosity of a collision through a calculation of the orbital energy lost from the star combined with the rate of collisions. Given the thickness of the disk and the location of the star at any given time the geometry of the disk region carved out by the star (hereafter shock tunnel) is modelled in §7. In §8 we illustrate the flare profiles of an impactor for differing radial impact locations within the disk, that are dependent on the photon diffusion time or the sound crossing time. In §9

some of the disk, impactor, SNC, and SMBH parameters are adjusted to more extreme values to investigate what effects they may have. Finally, §10 summarizes what was found throughout this work.

2 Fiducial Values

Throughout this report cgs (centimeter, gram, second) units are employed, in order to align with the current literature within this field of astronomy, and relevant quantities are calculated using a set of fiducial parameters, unless otherwise mentioned. For those quantities pertaining to the SMBH and its orbiting accretion disk, they are assumed to be more typical of AGNs at large.

Since quasars have central SMBH masses ranging from $M_\bullet \sim 10^6 - 10^{10}\ M_\odot$, a moderate mass has been chosen to be $M_\bullet = 10^8\ M_\odot$. This mass is also the typical value found in many of the adopted models used throughout this report.

The rate at which mass accretes onto the quasar's SMBH is called the accretion rate $\dot{M}_\mathrm{d}$ and it can range from $\dot{M}_\mathrm{d} \sim (0.01-1)\dot{M}_\mathrm{Edd}$[3]. Thus, the fiducial value of $\dot{M}_\mathrm{d} = 0.1\dot{M}_\mathrm{Edd}$ is chosen so that it lies in between these two extremes.

Although the exact mechanism underlying the transport of angular momentum outwards (in order for the disk matter to spiral inwards) is not fully understood it is most often referred to as the 'viscosity' parameter α. Observational evidence and theoretical estimates put the viscosity parameter in the range of $\alpha \sim 0.1 - 0.4$ ($\lesssim 0.02$) (King et al., 2007). Thus, the fiducial value used in this report is chosen to be $\alpha = 0.1$, which is more in agreement with the lower end of the observational evidence.

The impactor is assumed to be a sun-like star with a solar mass and radius of $M_\star = M_\odot$ and $R_\star = R_\odot$, respectively, which will be slightly relaxed to better approximate the density of the impactor's atmosphere and outer envelope in section 5.

The impactor is modelled to be travelling its fastest when it strikes the disk at its periapse.

[3]The Eddington accretion rate $\dot{M}_\mathrm{Edd}$ is the accretion rate for which the black hole radiates at the Eddington luminosity L_Edd,

$$\dot{M}_\mathrm{Edd} = \frac{L_\mathrm{Edd}}{\epsilon c^2} = \frac{10^{38}}{\epsilon c^2}\frac{M_\bullet}{M_\odot}\frac{\mathrm{erg}}{\mathrm{s}} \tag{2.1}$$

where ϵ is the radiative efficiency and $c = 2.99792458 \times 10^{10}$ cm s^{-1} is the speed of light.

It is assumed to be on a parabolic orbit with an eccentricity of $e = 1$, which gives it an impact velocity of $v_\star = \sqrt{2GM_\bullet/r}$, where $G = 6.674 \times 10^{-8}$ cm^3 g^{-1} s^{-2} is Newton's gravitational constant and r is the radial impact location.

Furthermore, it strikes the disk with a fiducial inclination angle, relative to the accretion disk, of $I = \pi/2$ and, in the reference frame of the SMBH, it travels vertically through the disk.

In §9, these parameters will be expanded to more extreme cases to investigate their effects.

2.1 Schwarzschild Radius

The Schwarzschild radius $R_{\rm Sch}$ is a general relativistic (GR) term that describes the spatial location of a BH's event horizon, which increases with $M_\bullet$.

$$R_{\rm Sch} = 2\frac{GM_\bullet}{c^2} \tag{2.2}$$

The relation $R_{\rm g}$ is worked out to provide a fiducial Schwarzschild radius,

$$R_{\rm g} = 2\frac{G}{c^2}10^8 M_\odot \sim 2.95 \times 10^{13} \text{ cm} \sim 2 \text{ AU} \tag{2.3}$$

The Schwarzschild radius defines a sphere within which light cannot escape from a non-rotating BH, such that no information can be obtained by an outside observer. For the purposes of this report, $R_{\rm g}$ is frequently used as a radial unit of spatial measurement when considering various quantities, instead of the more appropriate cgs distance measurement of centimeters. It also provides a minimum radius to take into account when making assumptions, such that the approximations made do not breach the relativistic realm. The description and discussion of $R_{\rm g}$ here is intentionally brief, due to this report ignoring a lot of relativistic effects, but more thorough explanations can be found in general relativity

texts.

3 Stellar Nuclear Cluster & Star-Disk Collision Rate

In the central region, close to and surrounding the SMBH, are orbiting stars which are collectively refered to as the stellar nuclear cluster (hereafter SNC). A density profile of the SNC, $n_{\rm SNC}$, provided by Pariev & Colgate (2007) is adopted in this work. The profile introduces two new boundaries that are dependent on the central stellar population. One of these boundaries is dependent on the tidal radius (defined below in §3.1.1) of the SMBH, and required a brief recalculation in order to be in agreement with this work's proposed scenario. This recalculation leads into a discussion of how the tidal radius and the boundary are related. Under the assumption that these stars are on parabolic orbits that intersect the accretion disk, the average time between collisions and the average collisional rate is worked out.

3.1 Stellar Density Profile

When considering stars that collide with an accretion disk it is useful to approximate where stars can reside around a SMBH. A density profile of the stars in the SNC, $n_{\rm SNC}$ is adopted from the work of Pariev & Colgate (2007) (hereafter PC07), who modelled their profile after the work of Rauch (1995). Rauch (1995) examines how star clusters orbiting BHs dynamically evolve while interacting with an accretion disk. PC07 select a model that resembles a steady state system, where two-body relaxation of the outer stars is able to replenish and balance the loss of stars closer to the SMBH due to TDEs, orbital ejections, collisions, or being swallowed by the BH. PC07 model their stellar profile around a $10^8 M_\odot$ SMBH, which is in agreement with the fiducial values chosen in this work. The

profile is broken up into three distinct regions,

$$n_{\rm SNC} = \begin{cases} n_5 10^5 \ \frac{M_\odot}{\rm pc^3} \left(\frac{r}{1 \ \rm pc}\right)^{-7/4} & \text{for } r > r_2 \\ n_5 \left(3.16 \times 10^8\right) \ \frac{M_\odot}{\rm pc^3} & \text{for } r_1 < r \leq r_2 \\ 0 & \text{for } r \leq r_1 \end{cases} \tag{3.1}$$

where $r_1 = 10 r_t$, r_t is the tidal radius, $r_2 = 10^{-2}$ pc, and $n_5 = n(1 \text{ pc})/(10^5 \ M_\odot/\text{pc}^{-3})$ with $n(1 \text{ pc}) \sim (10^4 - 10^6) \ M_\odot \text{ pc}^{-3}$ is the stellar density at 1 pc inferred from observations from M32 and M31 (Lauer et al., 1995). A parsec is defined as pc $= 3.086 \times 10^{18}$ cm $\sim 1.05 \times 10^5 R_{\rm g}$ for our fiducial SMBH, and note that the coefficient for the middle region differs slightly from PC07 to ensure continuity.

An observer following a radial trajectory towards the SMBH would begin to see an increase in the number of stars orbiting the BH in the outer regions, until reaching r_2 where the number of stars would cease to increase and remain constant until they reached r_1 and no longer saw stars at the same radius from the BH. The crude approximation of no stars within the innermost region is due to star-star collisions, tidal disruption events, and stars that become captured by the disk.

Figure 3.1 depicts the profile of the SNC around the SMBH.

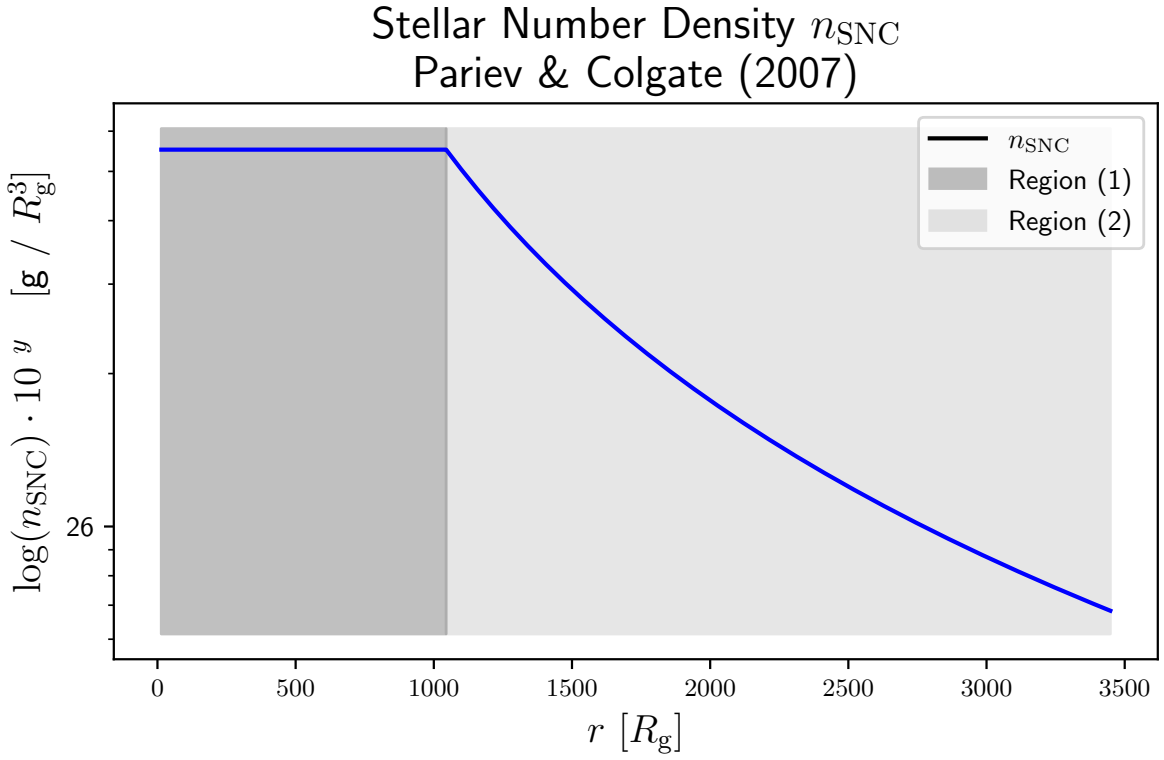

Figure 3.1: The logarithmic stellar number density of the stellar nuclear cluster around a SMBH of mass $M_\bullet = 10^8 M_\odot$. Where $r < r_1 = 10\ r_t$ (region 0) it is assumed that there are no stars due to TDEs, two-body relaxation between the stars, and stars that become "captured" by the disk. Where $r_1 < r < r_2$ (region 1, dark gray) the stellar number density is constant, before it drops off by $r^{-7/4}$ where $r > r_2 = 10^{-2}$ pc (region 2, light gray).

A central starless core (hereafter, region 0) at radii less than r_1 is surrounded by a region (hereafter, region 1) filled by a steady amount of stars that extends out to r_2 where the number of stars begins to rapidly decreases as $r^{-7/4}$ (hereafter, region 2).

3.1.1 Tidal Radius

Since the inner bound r_1 that defines where the SNC is void of stars is dependent on the tidal radius of the SMBH r_t, a derivation and description of tidal radius is. This section will first guide the reader through a derivation of the tidal radius and conclude with a calculation for the fiducial values used throughout this report.

The tidal radius r_t, also known as the Roche radius, of a spherical body is the point

at which an object within this radius will be torn apart due to the tidal force of the body overcoming the self-gravitation of the object. To clarify this, consider a rigid spherical body with mass M and radius R (hereafter the 'primary' body) separated by a distance ℓ from an orbiting satellite of mass m and radius r (hereafter the 'secondary' body). A particle of mass μ lies on the surface of the satellite that is closest to the primary body. The gravitational force F_G on μ due to the satellite is given by Newton's law of universal gravitation.

$$F_G = G\frac{m\mu}{r^2} \tag{3.2}$$

The tidal force F_T on μ due to the primary body is determined by evaluating the difference between the gravitational force on a surface particle and a central particle of the satellite, both with mass μ.

$$F_T = G\frac{M\mu}{(\ell - r)^2} - G\frac{M\mu}{\ell^2} = GM\mu\left(\frac{\ell^2 - (\ell - r)^2}{\ell^2(\ell - r)^2}\right) = GM\mu\left(\frac{2r\ell - r^2}{\ell^4 - 2r\ell^3 + r^2\ell^2}\right) \tag{3.3}$$

If $r \ll R$ and $R < \ell$ then $r \ll \ell$. In this approximation terms where r is to some power greater than unity will vanish and the tidal force expression is simplified.

$$F_T \approx GM\mu\left(\frac{2r\ell}{\ell^4}\right) = 2G\frac{M\mu}{\ell^3}r \tag{3.4}$$

The tidal radius is reached at the distance ℓ where the primary's approximated tidal force on μ is balanced by the satellite's gravitational force.

$$F_G = F_T \;\rightarrow\; G\frac{m\mu}{r^2} = 2G\frac{M\mu}{\ell^3}r \;\rightarrow\; \ell^3 = 2\frac{M}{m}r^3 \;\rightarrow\; \ell = r\left(2\frac{M}{m}\right)^{1/3}. \tag{3.5}$$

This distance is the tidal radius $\ell = r_t$, and is dependent on the ratio of the two masses

and the radius of the satellite. By applying the density relation,

$$\rho_i = \frac{M_i}{V_i} = \frac{M_i}{\frac{4}{3}\pi R_i^3} \ , \tag{3.6}$$

the tidal radius can also be expressed in terms of the primary's radius and the density ratio of the two bodies:

$$r_t = r\left(2\frac{M}{m}\right)^{1/3} = r\left(2\frac{\rho_M R^3}{\rho_m r^3}\right)^{1/3} = R\left(2\frac{\rho_M}{\rho_m}\right)^{1/3} \ . \tag{3.7}$$

For this work a SMBH of mass $M_\bullet = 10^8 M_\odot$ assumed to be the primary body, while an impactor of mass $M_\odot$ is taken as the secondary body. Inputting the fiducial values and introducing some dimensionless quantities for convenience yields,

$$r_t = r\left(2\frac{M}{m}\right)^{1/3} = R_\odot\left(2\frac{10^8 M_\odot}{M_\odot}\right)^{1/3}\left(\frac{M_\bullet}{10^8 M_\odot}\right)^{1/3}\left(\frac{M_\star}{M_\odot}\right)^{-1/3}\frac{R_\star}{R_\odot} \ . \tag{3.8}$$

Evaluating the constants gives

$$r_t \sim 4.07\times 10^{13}\ \text{cm}\left(\frac{M_\bullet}{10^8 M_\odot}\right)^{1/3}\left(\frac{M_\star}{M_\odot}\right)^{-1/3}\frac{R_\star}{R_\odot} \tag{3.9}$$

which is calculated to be $\sim 1.4 R_{\rm g}$ when using the fiducial values. In terms of $R_{\rm g}$, the inner boundary r_1, that describes where the SNC is void of stars, is determined to be

$$r_1 = 10\ r_t \sim 14\ R_{\rm g} \ . \tag{3.10}$$

Due to the tidal radius' dependence on the physical properties of the primary and secondary bodies, its influential domain is restricted by these quantities. We will now consider how the SNC and r_1 are affected when $M_\bullet$, $M_\star$, and $R_\star$ take on other, non-fiducial, values. If the orbiting stars surround a much more massive SMBH ($M_\bullet > 10^8 M_\odot$), the

gravitational force exerted by this SMBH will be stronger, r_t will radially extend further out and produce an enlarged starless core of the SNC. Stars close to the SMBH would be in a deep potential well within r_1 and possess larger orbital velocities. These larger speeds increase their likelihood of colliding with another star, undergoing a TDE, or being flung out of the system or into the SMBH. Thus, this region of greater stellar activity would result in a larger, crudely approximated, core being carved out of the SNC. If central SMBH was less massive ($M_\bullet < 10^8 M_\odot$), the same reasoning can be used to show how the spatial extent of the core would be smaller than the fiducial value due to the stellar system having less orbital energy.

Conversely, if the mass of the SMBH is fiducial ($M_\bullet = 10^8 M_\odot$) but the orbiting stars are more massive than ($M_\star > M_\odot$), the gravitational force exerted by an individual star is greater, r_t will be less expansive, and the stellar void of the SNC *may* be smaller. As far as Eq.(3.8) is concerned, a larger m creates a smaller r_t, but does not necessarily create a smaller r_1. Unlike the first case, the stars will possess the same orbital velocity but will instead have a stronger self-gravitational influence making them more resistant to the SMBH's gravitational pull. Neighbouring stars would have a greater gravitational influence on one another and potentially alter each other's orbital trajectories. These trajectories could send them hurtling towards other stars, the SMBH, or out of the system, thereby increasing the chaotic nature of this region. Since this stellar activity constitutes the approximations made in defining the starless core, whether or not the spatial extent of the core would be larger or smaller is difficult to discern.

A SNC with sufficiently less massive stars $M_\star < M_\odot$, everything else fiducial, would mathematically produce a larger r_t as the self-gravitational influence of the stars would be weaker. This decrease in the star's gravitational influence weakens their ability to self-gravitate and resist the SMBH's influence, thus increasing the likelihood of experiencing a TDE. Although the rate of stellar collisions, orbital ejections, or star's flung into the

SMBH is unlikely to be grander, it is assumed that the greater number of TDEs would result in a greater spatial extent of the SNC core.

Similarly, if the SNC were to have sufficiently larger (smaller) stars $R_\star > R_\odot$, r_t would be larger (smaller). In these cases the gravitational influence of either body takes on their fiducial values, but instead the stars have larger (smaller) stellar atmospheres. A larger atmosphere would be weakly bound to its host star and be more easily torn off by the larger r_t, while a smaller atmosphere would be tightly bound to its host star and better resist the shearing effects of a smaller r_t. This leads to a faster (slower) rate of TDEs, and by using the aforementioned argument for less massive stars, the spatial extent of the starless core would also be larger (smaller).

3.2 Average Collisional Time

If the stars orbiting the SMBH are isotropically distributed with a parabolic velocity of

$$v_\star = \sqrt{2}(r\Omega_K) \ , \tag{3.11}$$

where $\Omega_K = \sqrt{GM_\bullet/r^3}$, Pariev & Colgate (2007) give the flux of stars through one side of the disk, $F_\star$, as 0 for $r \leq r_1$ and

$$F_\star = \frac{n_{\rm SNC} v_\star}{4} = \begin{cases} \frac{2.4\times10^{-39}\ n_5}{\rm cm^2\ s}\left(\frac{r}{r_2}\right)^{-9/4} & \text{for} \quad r > r_2 \\ \frac{2.4\times10^{-39}\ n_5}{\rm cm^2\ s}\left(\frac{r}{r_2}\right)^{-1/2} & \text{for} \quad r_1 < r \leq r_2 \end{cases} \ , \tag{3.12}$$

where $n_{\rm SNC}$ is the stellar density profile. The flux of stars passing through both sides of the disk is twice this value, $F = 2F_\star$. To convert from the flux of stars to the number of stars passing through the disk, F must first be integrated over the area of a flat disk with its origin at the center of the SMBH. The azimuthal angle, θ, is swept about the entire

unit circle and the radius extends out to a given r within each region.

$$I_f = \int_A F \; dA = \int_0^{2\pi} \int_0^r F \; r dr d\theta \tag{3.13}$$

The inverse of this integral is defined as the average time between collisions $\Delta T_c(r)$ for both sides of the disk within the radius r, which is ∞ for $r \leq r_1$ and

$$\Delta T_c(r) = \begin{cases} \frac{2\pi}{\Omega_K(r)} \frac{2.94\times10^{-5}}{n_5} \left(\frac{r}{r_2}\right)^{-3/2} \left[1.15 - \left(\frac{r}{r_2}\right)^{-1/4}\right]^{-1} & \text{for } r > r_2 \\ \frac{2\pi}{\Omega_K(r)} \frac{1.91\times10^{-2}}{n_5} \left(\frac{r}{r_1}\right)^{-3/2} \left[\left(\frac{r}{r_1}\right)^{3/2} - 1\right]^{-1} & \text{for } r_1 < r \leq r_2 \end{cases} \tag{3.14}$$

Figure 3.2 illustrates the behaviour of $\Delta T_c(r)$.

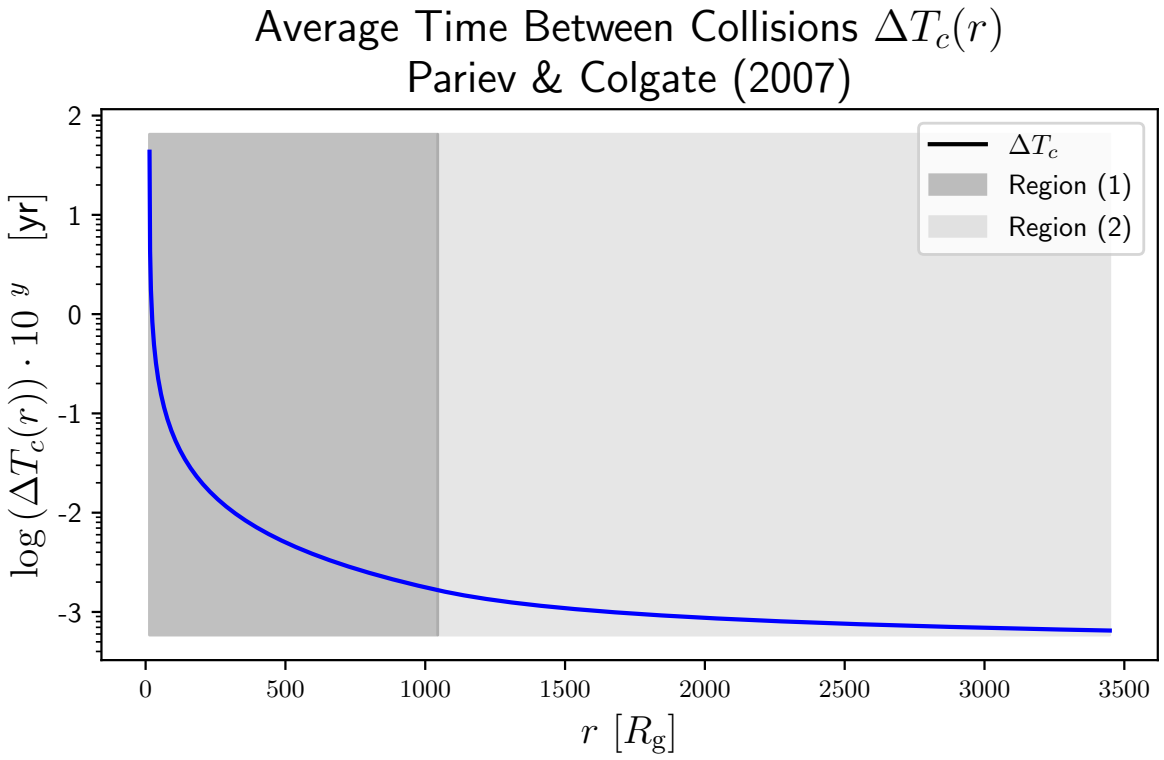

Figure 3.2: The average time between star-disk collisions for all impactors within a given radius. The impactors are assumed to pass through both sides of the disk. Within 2000 R_g there are roughly 3 collisions per day.

It is important to note that the average time $\Delta T_c(r)$ takes into account all stars within the radius r. Such that, as r increases the amount of stars within r increases and the average time between stars colliding with the disk decreases. For example within 2000 $R_{\rm g}$ there are roughly 3 collisions per day. Since the SNC profile is assumed to be void of stars within r_1 there are no collisions and $\Delta T_c(r)$ approaches infinity as r approaches r_1.

3.3 Average Collisional Rate

The average time between collisions within a given radius r can be reinterpreted as an average collisional rate $\mathcal{R}_{\rm c}$.

By multiplying by any differential area dA, we can figure out the rate $\mathcal{R}_{\rm c} \equiv F\ dA$ of star-disk collisions in that area. If we choose $dA = 2\pi r\ dr$, then we have the rate of star-disk collisions as a function of radius:

$$\mathcal{R}_{\rm c} = 4\pi n_5\ (2.4 \times 10^{-39}\ {\rm cm}^{-2}\ {\rm s}^{-1})\ \times \begin{cases} r_2^{9/4} r^{-5/4}\ dr & \text{for } r > r_2 \\ r_2^{1/2} r^{1/2}\ dr & \text{for } r_1 < r \leq r_2 \end{cases} \tag{3.15}$$

where r and dr are taken to be in unit cm. Figure 3.3 illustrates the behaviour of the $\mathcal{R}_{\rm c}$.

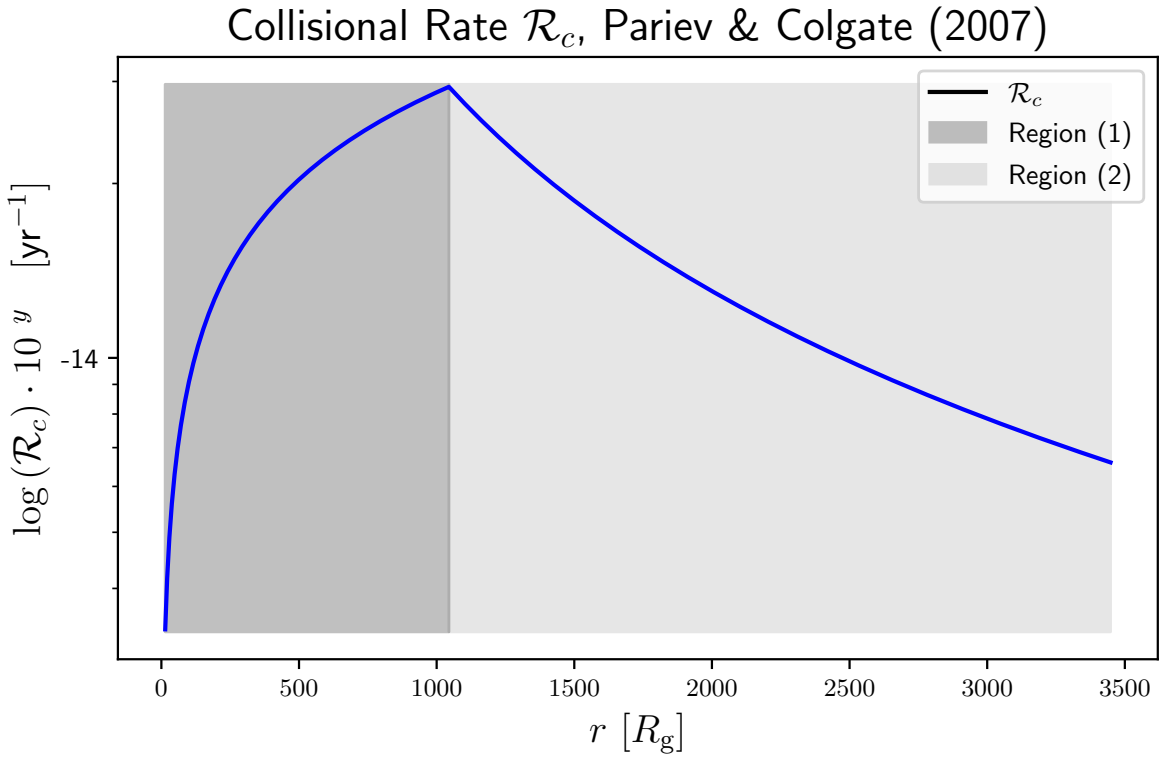

Figure 3.3: The logarithmic rate of star-disk collisions $\mathcal{R}_c$ as a function of radius in units of R_g, where the impactors are assumed to pass through both sides of the disk. In region (1) (dark gray) the rate increases with radius as $r^{1/2}$, and decreases with radius in region (2) (light gray) as $r^{-5/4}$. It is assumed that there are no stars present in region (0), so $\mathcal{R}_c = 0$ and the plotted curve does not extend into this region.

3.4 Summary

The stellar profile of the $n_{\rm SNC}$ has a starless void at its centre, region (0), that is surrounded by a isotropic sphere of stars, region (1), that begins to taper off as $r^{-7/4}$ beyond r_2, region (2). The crude approximation of a core, is from the assumption that stars within region (0) would be destroyed from star-star collisions and TDEs, or tossed out of the system and into the black hole by stellar two-body relaxation. The spatial extent of region (2) is fixed due to the its inner bound r_2 having a fixed radial location of 10^{-2} pc. Conversely, the radial extent of both the core and isotropic sphere are determined by the location of the inner most boundary r_1, which is dependent on the tidal radius $r_1 = 10r_t$. Larger

values of r_1 increase the core while decreasing the isotropic sphere, while smaller values of r_1 have shrunken cores encased by larger isotropic spheres.

The tidal radius has a grander range for large values of $M_\bullet$ and $R_\star$ and small values of $M_\star$. When r_t is interpreted by considering the ratio of the densities it is found that increasing the density of the SMBH, or decreasing the density of the orbiting stars, is what increases the expanse of r_t and thus r_1.

The average collisional time $\Delta T_c(r)$ is the mean time for all star-disk collisions that take place within a given radius r. Because of this as r increases the mean time between collisions rapidly decreases in region (1), where the stellar population is constant with radius, and slowly decreases in region (2) where the number of stars begin to become more sparse. The assumed lack of stars within region (0) cause $\Delta T_c(r)$ to be approximated as infinity.

Much like the average collisional time, the star-disk collisional rate $\mathcal{R}_c$ accounts for all collisions within a specified differential area of $2\pi r\ dr$. Thus, the collisional rate increases quite rapidly with radius as in region (1) where the number of stars is constant with r, and begins to decrease in region (2) as the number of stars begin to reduce with r. Again, a lack of stars in the core results in R_c being zero in region (0).

Formally, there are 3 distinct regions that define the stellar profile of the SNC, but due to the starless core in region (0) interpretations of star-disk interactions here, such as $\mathcal{R}_c$ and $\Delta T_c(r)$, are non-physical. The subsequent sections, and derivations therein, will take region (0) into consideration by ignoring any phenomena that occurs at radii within the core, i.e. $r \leq r_1$.

4 Accretion Disk Model

Shakura & Sunyaev (1973) provide a model for the accretion disk surrounding a supermassive black hole (hereafter SMBH). They assume the disk has a finite thickness that is balanced by the gravitational influence of the SMBH and a pressure force generated by the gaseous disk material and/or the radiative photons within the disk. Along with differing sources for the opacity of the disk, these differences in pressure give rise to distinct regions with differing sound speeds $v_{\rm s}^2$. These regions are used throughout this work to help model the effects of a star impacting the accretion disk. In this section we show how the surface density of the disk $\sigma_{\rm d}$, the half-thickness of the disk $H_{\rm d}$, the surface temperature $T_{\rm d}$, and the mass and electron number density $\rho_{\rm d}$ and n_e, respectively, change with radius in each region.

4.1 Basic Structure

Shakura & Sunyaev (1973) (hereafter SS73) describe various properties pertaining to accretion disks orbiting BHs, providing a model for the accretion disk.

In this model it is assumed that the central BH has a mass of $M_\bullet$ that creates an accretion disk with an accretion rate of $\dot{M}_{\rm d}$ and mid-plane height of $H_{\rm d}$. The efficiency of the mechanism of angular momentum is characterized by the parameter α, more commonly referred to as the 'viscosity' parameter. It is governed by the relation

$$\alpha = \frac{v_t}{v_s} + \frac{\mathcal{H}_{\rm d}^2}{4\pi\rho_{\rm d}v_s^2} \tag{4.1}$$

where

$$\frac{\rho_{\rm d}v_s^2}{2} = \frac{3}{2}\rho_{\rm d}\frac{k_B T_{\rm d}}{m_p} + \epsilon_r \tag{4.2}$$

is the thermal energy density of matter, ϵ_r is the energy density of radiation, v_t is the turbulent velocity, v_s is the sound speed, $\mathcal{H}_{\rm d}$ is the magnetic field, $\rho_{\rm d}$ is the density,

$k_B = 1.381 \times 10^{16}$ cm^2 g s^{-2} K is Boltzmann's constant, $T_{\rm d}$ is the surface temperature of the disk, and m_p is the proton mass. It is important to realize that α is a dimensionless mean quantity, that is averaged orthogonal to the disk plane. It is well defined for thin disks (i.e., $H_{\rm d} \ll r$), but has little meaning for thick disks (i.e., $H_{\rm d} \sim r$) if the quantities that determine α vary greatly with height.

For convenience SS73 introduce dimensionless parameters to aid in describing the disk's properties, which in this paper include the subscript 'ss' to be easily distinguished from other variables. These parameters are the accretion disk's relative mass $m_{\rm ss}$, accretion rate $\dot{m}_{\rm ss}$, radial position $r_{\rm ss}$, and a radial parameter $\tilde{\phi}_{\rm ss}$, which are all defined below.

$$m_{\rm ss} = \frac{M_\bullet}{M_\odot}, \quad \dot{m}_{\rm ss} = \frac{\dot{M}_{\rm d}}{\dot{M}_{\rm cr}}, \quad r_{\rm ss} = \frac{r}{3R_{\rm Sch}}, \quad \tilde{\phi}_{\rm ss} = (1 - r_{\rm ss}^{-1/2}) \tag{4.3}$$

where r is the radial position within the disk, and the critical accretion rate (flux of matter) $\dot{M}_{\rm cr}$ is given by the relation:

$$\dot{M}_{\rm cr} = 3 \times 10^{-8} m_{\rm ss} \frac{0.06}{\eta} \frac{M_\odot}{\rm year} \tag{4.4}$$

where η is the efficiency of gravitational release (which is $\eta \backsimeq 0.06$ for a Schwarzschild BH). It is important to choose appropriate radial positions when approximating relevant quantities, since some are dependent on $\tilde{\phi}_{\rm ss}$. When $r_{\rm ss} = 1$ the term $\tilde{\phi}_{\rm ss} = 0$ causing the quantities to equate to zero or become infinite. Furthermore, Newtonian physics breaks down at $r_{\rm ss} < 1$ which is located beyond the BH's event horizon. When $\dot{M}_{\rm cr} = 1$ the disk luminosity is that of the Eddington luminosity,

$$L_{\rm Edd} = 10^{38} \frac{M_\bullet}{M_\odot} \frac{\rm erg}{\rm s} \tag{4.5}$$

This is the maximum luminosity that an astrophysical body can achieve at hydrostatic equilibrium, when the gravitational and radiative forces balance. Typical values for $\dot{m}_{\rm ss}$

are in the range $\sim (0.1 - 1)$ resulting in accretion disk luminosities of $L \sim (10^{45} - 10^{46})$ erg s^{-1} when $M_\bullet = 10^8 M_\odot$.

The accretion disk is nearly flattened by the gravitational influence of the BH, but a counteracting pressure force, due to gaseous $P_{\rm g}$ or radiative $P_{\rm r}$ pressures, is able to extend the disk out vertically providing it with a finite thickness. The opacity of the disk is dominated by Thompson scattering $\sigma_{\rm T}$ or free-free absorption $\sigma_{\rm ff}$. These differences in pressures and opacities give rise to distinct regions with differing sound speeds $v_{\rm s}^2$, Table 4.1.

Region	**Pressure**	**Opacity**	$v_{\rm s}^2$	**Range**
(a)	$P_{\rm r} \gg P_{\rm g}$	$\sigma_{\rm T} \gg \sigma_{\rm ff}$	$\epsilon/(3\rho_{\rm d})$	$r < r_{\rm ab}$
(b)	$P_{\rm r} \ll P_{\rm g}$	$\sigma_{\rm T} \gg \sigma_{\rm ff}$	$(k_B T_{\rm d})/m_p$	$r_{\rm ab} \leq r < r_{\rm bc}$
(c)	$P_{\rm r} \ll P_{\rm g}$	$\sigma_{\rm T} \ll \sigma_{\rm ff}$	$(k_B T_{\rm d})/m_p$	$r \geq r_{\rm bc}$

Table 4.1: Three separate regions that make up an accretion disk according to Shakura & Sunyaev (1973). They are defined by the pressure dominance, either radiation pressure $P_{\rm r}$ or gas pressure $P_{\rm g}$, and the dominant type of photon scattering, either Thompson scattering $\sigma_{\rm T}$ or free-free absorption $\sigma_{\rm ff}$. The radial sound speed for each region is given as well as their respective boundaries.

According to SS73, the innermost and outermost regions of the disk have the parameters of region (c), region (a) is a middle region, and there are two regions (b) that act as borders between (a) and (c). However for this report, we approximate the disk as having only three regions where (a) is the innermost region, (c) is the outermost region, and (b) is an intermediate region between (a) and (c). The boundaries between these regions are worked out in terms of the dimensionless parameters where the dimensionless parameter $\tilde{\phi}_{\rm ss}$ has its subscript altered to reflect the different relative radii. The boundary between regions (a) and (b) is located at $r_{\rm ab}$ and depends on α and all relative parameters.

$$r_{\rm ab} = 150\,(\alpha\; m_{\rm ss})^{2/21} \left(\dot{m}_{\rm ss}\; \tilde{\phi}_{\rm ab}\right)^{16/21} \approx 150\,(\alpha\; m_{\rm ss})^{2/21}\;\; \dot{m}_{\rm ss}{}^{16/21}\; R_{\rm g} \tag{4.6}$$

While the boundary between regions (b) and (c) is located at $r_{\rm bc}$, and only depends on the relative accretion rate and radial position.

$$r_{\rm bc} = 6.3 \times 10^3 \left(\dot{m}_{\rm ss} \, \tilde{\phi}_{\rm bc} \right)^{2/3} \approx 8000 \, \dot{m}_{\rm ss}^{2/3} \, R_{\rm g} \tag{4.7}$$

For these relations the final approximation term, expressed in units of $R_{\rm g}$, was taken from SS73's tenth figure illustrating the disk regions with differing physical conditions, presented in Figure 4.1. It is important to note that region (a) only exists if

$$\dot{m}_{\rm ss} \gtrsim \frac{(\alpha m_{\rm ss})^{-1/8}}{85} \, . \tag{4.8}$$

The right hand side of this inequality is calculated to be $\sim (3.3 - 1.9) \times 10^{-4}$ for all combinations of $\alpha = (0.01 - 1)$ and $M_\bullet = (10^6 - 10^{10}) M_\odot$. Thus, region (a) always exists because this is always less than the lowest value of $\dot{m}_{\rm ss} = 0.01$ used throughout this report.

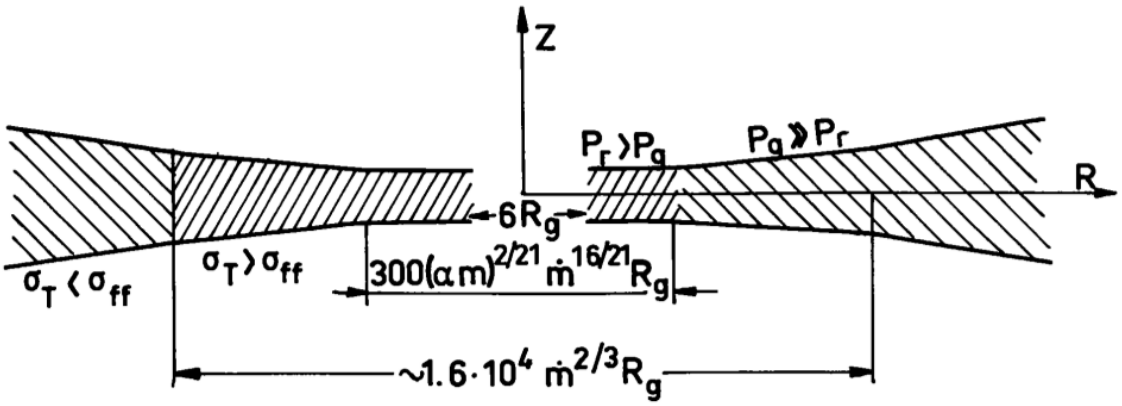

Fig. 10. The regions of disk having different physical conditions

Figure 4.1: The tenth figure from SS73 used to approximate the boundaries between each region. Note that the numerical values for the boundaries between the regions in this illustration represent diameters, causing them to be twice the value of what is discussed in the grander text.

4.2 Disk Half-Thickness

The half-thickness $H_{\rm d}$ of the accretion disk for each region in the α-disk model is:

$$H_{\rm d}\,[\rm cm] = \begin{cases} 3.2 \times 10^{6}\ \dot{m}_{\rm ss}\ m_{\rm ss}\ \tilde{\phi}_{\rm ss} & r < r_{\rm ab} \\ 1.2 \times 10^{4}\ \alpha^{-1/10}\ \dot{m}_{\rm ss}^{1/5}\ m_{\rm ss}^{9/10}\ r_{\rm ss}^{21/20}\ \tilde{\phi}_{\rm ss}^{2/5} & r_{\rm ab} \leq r < r_{\rm bc} \\ 6.1 \times 10^{3}\ \alpha^{-1/10}\ \dot{m}_{\rm ss}^{3/20}\ m_{\rm ss}^{9/10}\ r_{\rm ss}^{9/8} & r \geq r_{\rm bc} \end{cases} \tag{4.9}$$

Since these values are half-thicknesses, or mid-plane heights, the full thickness of the disk at any distance r away from the SMBH is twice this value: $2H_{\rm d}$. In general, the thickness of the disk increases with r and in the case of a thin disk (considered in this report) the half-thickness of the disk is much less than its radial distance from the SMBH: $H_{\rm d} \ll r$.

The thickness of the disk is weakly dependent on the viscosity and accretion rate of the disk. It will thicken as the viscosity and accretion rate of the disk decrease and increase, respectively. Disks that accrete onto the BH at the Eddington accretion rate with $\alpha \sim 0.01$ will be the most thick of the disks we consider.

Dividing the solar radius $R_{\odot} = 6.95 \times 10^{10}$ cm by $H_{\rm d}$ yields the relative size of a sun-like star to the half-thickness of the disk for all r and our fiducial values, which is illustrated in Figure 4.2.

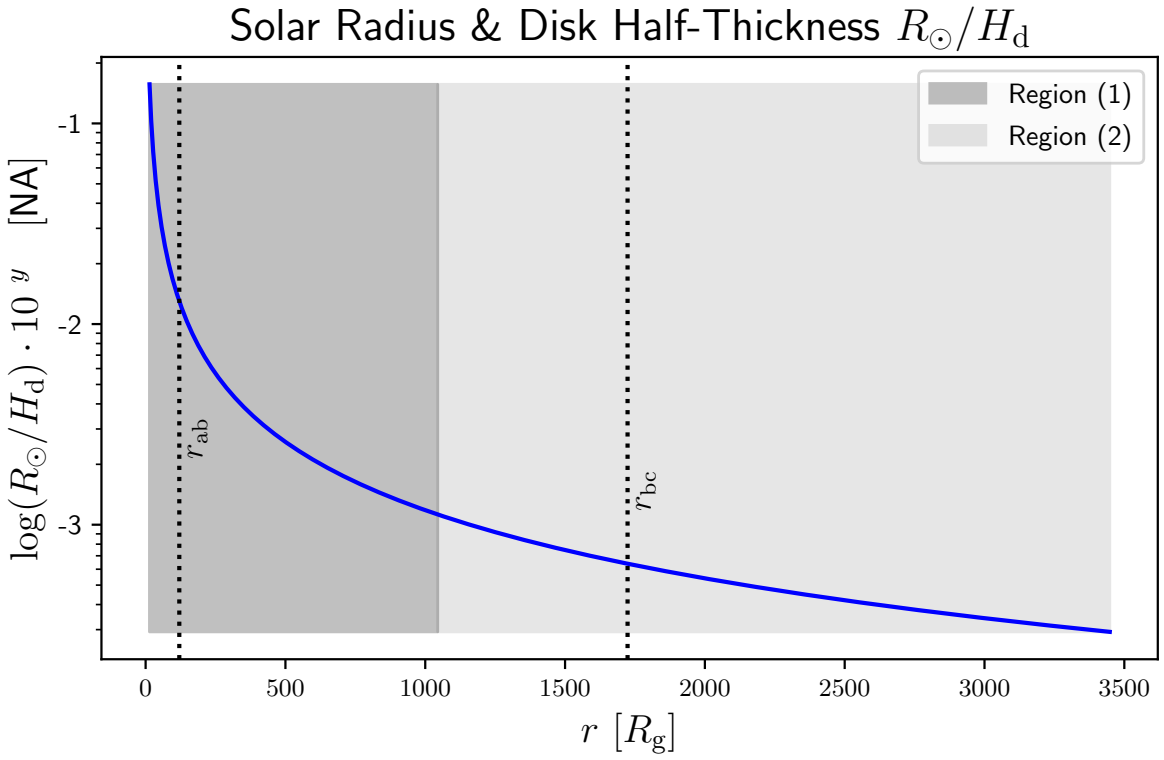

Figure 4.2: The relative size of a sun-like star $R_\odot$ compared to the α-disk model's half-thickness H_d provided by SS73. The fiducial disk parameters are assumed to be $\alpha = 0.1$, $\dot{M}_\mathrm{d} = 0.1\ \dot{M}_\mathrm{Edd}$, and $M_\bullet = 10^8\ M_\odot$. The dotted vertical black lines indicate the r_ab and r_bc boundaries of the accretion disk regions, while the shaded areas define the SNC regions (1) (dark gray) and (2) (light gray).

4.3 Densities

4.3.1 Surface Density

The accretion disk's central surface density σ_d is also defined differently for each region and can be approximated using the following equations.

$$\sigma_\mathrm{d}\left[\frac{\mathrm{g}}{\mathrm{cm}^2}\right] = \begin{cases} 4.6\ (\alpha\ \dot{m}_\mathrm{ss}\ \tilde{\phi}_\mathrm{ss})^{-1}\ r_\mathrm{ss}^{3/2} & \text{for } r < r_\mathrm{ab} \\ 1.7 \times 10^5\ \alpha^{-4/5}\ (\dot{m}_\mathrm{ss}\ \tilde{\phi}_\mathrm{ss})^{3/5}\ m_\mathrm{ss}^{1/5}\ r_\mathrm{ss}^{-3/5} & \text{for } r_\mathrm{ab} \leq r < r_\mathrm{bc} \\ 6.1 \times 10^5\ \alpha^{-4/5}\ (\dot{m}_\mathrm{ss}\ \tilde{\phi}_\mathrm{ss})^{7/10}\ m_\mathrm{ss}^{1/5}\ r_\mathrm{ss}^{-3/4} & \text{for } r \geq r_\mathrm{bc} \end{cases} \tag{4.10}$$

Figure 4.3 shows $\sigma_{\rm d}$ for the fiducial values of the SMBH and accretion disk. There are discontinuities at the boundaries $r_{\rm ab}$ and $r_{\rm bc}$, due to there being insufficient significant digits in the equations of SS73.

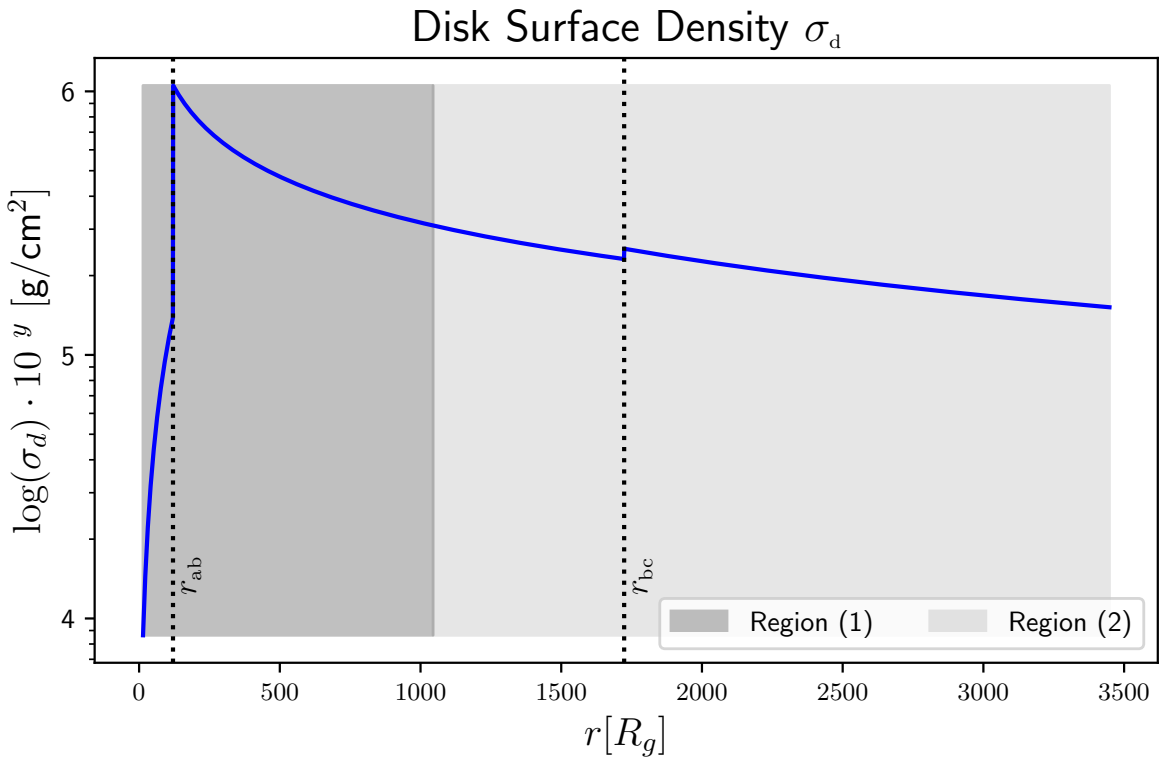

Figure 4.3: The surface density of an α-model SS73 accretion disk as a function of r in unit $R_{\rm g}$ for $M_\bullet = 10^8\ M_\odot$, $\alpha = 0.1$, and $\dot{M}_{\rm d} = 0.1\ \dot{M}_{\rm Edd}$. The dotted vertical black lines indicate the $r_{\rm ab}$ and $r_{\rm bc}$ boundaries of the accretion disk regions, while the shaded areas define the SNC regions (1) (dark gray) and (2) (light gray).

Since the $\tilde{\phi}_{\rm ss}$ term causes $\sigma_{\rm d}$ to approach infinity when $r_{\rm ss} \leq 1$, it is useful to consider the boundaries between each region that were given in Equations (4.6) and (4.7). The equations for $\sigma_{\rm d}$ can be recast into terms of $r_{\rm ab}$ and $r_{\rm bc}$ by expressing $r_{\rm ss}$ and $\tilde{\phi}_{\rm ss}$ as their respective radii. Region (a) is bordered by region (b), so only the $r_{\rm ab}$ boundary applies.

The substitution of $r_{\rm ab}$ into $\sigma_{\rm d(a)}$ is:

$$\begin{aligned}
\sigma_{\rm d(a)} \Big|_{r=r_{\rm ab}} &= 4.6\ (\alpha\ \dot{m}_{\rm ss}\ \tilde{\phi}_{\rm ab})^{-1}\ r_{\rm ab}^{3/2} \\
\sigma_{\rm d(a)}(r=r_{\rm ab}) &= \left(4.6\times 150^{3/2}\right)\ \alpha^{\left(\frac{1}{7}-1\right)}\ \dot{m}_{\rm ss}^{\left(\frac{8}{7}-1\right)}\ m_{\rm ss}^{1/7}\ \tilde{\phi}_{\rm ab}^{\left(\frac{8}{7}-1\right)} \\
\sigma_{\rm a}(r_{\rm ab}) &= 8.45\times 10^3\ \alpha^{-6/7}\left(\dot{m}_{\rm ss}\ m_{\rm ss}\ \tilde{\phi}_{\rm ab}\right)^{1/7} \\
\longrightarrow \quad \sigma_{\rm a}(r_{\rm ab})\left[\tfrac{\rm g}{\rm cm^2}\right] &= 8.45\times 10^3\left(\tfrac{\dot{m}_{\rm ss}\ m_{\rm ss}\ \tilde{\phi}_{\rm ab}}{\alpha^6}\right)^{1/7}
\end{aligned} \tag{4.11}$$

Region (c) is bordered by region (b), so only the $r_{\rm bc}$ boundary applies. The substitution of $r_{\rm bc}$ into $\sigma_{\rm d(c)}$ is:

$$\begin{aligned}
\sigma_{\rm d(c)} \Big|_{r=r_{\rm bc}} &= 6.1\times 10^5\alpha^{-4/5}(\dot{m}_{\rm ss}\ \tilde{\phi}_{\rm bc})^{7/10}m_{\rm ss}^{1/5}r_{\rm bc}^{-3/4} \\
\sigma_{\rm d(c)}(r=r_{\rm bc}) &= 6.1\times 10^5\left(6.3\times 10^3\right)^{-3/4}\ \alpha^{-4/5}\ \dot{m}_{\rm ss}^{\left(\frac{7}{10}-\frac{1}{2}\right)}\ m_{\rm ss}^{1/5}\ \tilde{\phi}_{\rm bc}^{\left(\frac{7}{10}-\frac{1}{2}\right)} \\
\sigma_{\rm c}(r_{\rm bc}) &= 8.63\times 10^2\ \alpha^{-4/5}\left(\dot{m}_{\rm ss}\ m_{\rm ss}\ \tilde{\phi}_{\rm bc}\right)^{1/5} \\
\longrightarrow \quad \sigma_{\rm c}(r_{\rm bc})\left[\tfrac{\rm g}{\rm cm^2}\right] &= 8.63\times 10^2\left(\tfrac{\dot{m}_{\rm ss}\ m_{\rm ss}\ \tilde{\phi}_{\rm bc}}{\alpha^4}\right)^{1/5}
\end{aligned} \tag{4.12}$$

Region (b) is bordered by both regions (a) and (c), so both regional boundaries apply. The substitution of the boundaries into $\sigma_{\rm d(b)}$ yield identical parameters as derived previously, thus confirming their nature of being boundaries. However, the constant is slightly different so only the end results will be shown.

$$\sigma_{\rm b}(r_{\rm ab})\left[\frac{\rm g}{\rm cm^2}\right] \sim 8.41\times 10^3\left(\frac{\dot{m}_{\rm ss}\ m_{\rm ss}\ \tilde{\phi}_{\rm ab}}{\alpha^6}\right)^{1/7} \tag{4.13}$$

$$\sigma_{\rm b}(r_{\rm bc})\left[\frac{\rm g}{\rm cm^2}\right] \sim 8.93\times10^2\left(\frac{\dot{m}_{\rm ss}\ m_{\rm ss}\ \tilde{\phi}_{\rm bc}}{\alpha^4}\right)^{1/5} \tag{4.14}$$

Choosing values for the dimensionless parameters $m_{\rm ss}$, $\dot{m}_{\rm ss}$, α, allows the surface-density to be determined. Using the fiducial parameters previously outlined and $\eta = 0.06$ for non-rotating SMBH, the dimensionless parameters have the values of:

$$m_{\rm ss} = 10^8\ ,\ \dot{m}_{\rm ss} = 0.1\ ,\ \alpha = 0.1 \tag{4.15}$$

The values for $\tilde{\phi}_{\rm ab}$ and $\tilde{\phi}_{\rm bc}$ are calculated using the boundary approximations in terms of $R_{\rm g}$ in Equations (4.6) and (4.7). Substituting these values into the derived equations for $\sigma_{\rm d}$, and letting $\alpha = (0.01, 0.1, 1)$ and $\dot{m}_{\rm ss} = (0.1, 1)$, the accretion disk's surface densities in units of g/cm^2, along the regional boundaries are calculated to be:

$\dot{m}_{\rm ss}$	$\sigma_{\rm d}$	$\alpha = 0.01$	$\alpha = 0.1$	$\alpha = 1$
–	–	[g/cm^2] $\times 10^6$	[g/cm^2] $\times 10^5$	[g/cm^2] $\times 10^4$
0.1	$\sigma_{\rm a}(r_{\rm ab})$	4.31	5.99	8.35
	$\sigma_{\rm b}(r_{\rm ab})$	4.29	5.97	8.31
	$\sigma_{\rm b}(r_{\rm bc})$	0.89	1.41	2.23
	$\sigma_{\rm c}(r_{\rm bc})$	0.86	1.36	2.16
1	$\sigma_{\rm a}(r_{\rm ab})$	6.04	8.40	11.7
	$\sigma_{\rm b}(r_{\rm ab})$	6.02	8.36	11.6
	$\sigma_{\rm b}(r_{\rm bc})$	1.41	2.24	3.55
	$\sigma_{\rm c}(r_{\rm bc})$	1.36	2.16	3.43

Table 4.2: Surface densities of an accretion disk for each region at the radial boundaries, $r_{\rm ab}$ and $r_{\rm bc}$, for different values of α and $\dot{m}_{\rm ss}$. Here $m_{\rm ss} = 10^8$ and $\eta = 0.06$.

4.3.2 Volumetric Mass Density

The volumetric mass density ρ_{d} for each disk region is determined by dividing the disk's surface density σ_{d} by the thickness of the disk $2H_{\mathrm{d}}$,

$$\rho_{\mathrm{d}}\left[\frac{\mathrm{g}}{\mathrm{cm}^3}\right] = \frac{\sigma_{\mathrm{d}}}{2H_{\mathrm{d}}} \approx \begin{cases} 7.2\times10^{-7}(\alpha m_{\mathrm{ss}})^{-1}(\dot{m}_{\mathrm{ss}}\tilde{\phi}_{\mathrm{ss}})^{-2}r_{\mathrm{ss}}^{3/2} & r < r_{\mathrm{ab}} \\ 7.1(\alpha m_{\mathrm{ss}})^{-7/10}(\dot{m}_{\mathrm{ss}}\tilde{\phi}_{\mathrm{ss}})^{2/5}r_{\mathrm{ss}}^{-33/20} & r_{\mathrm{ab}} \le r < r_{\mathrm{bc}} \\ 50(\alpha m_{\mathrm{ss}})^{-7/10}(\dot{m}_{\mathrm{ss}}\tilde{\phi}_{\mathrm{ss}})^{11/20}r_{\mathrm{ss}}^{-15/8} & r \ge r_{\mathrm{bc}} \end{cases} \tag{4.16}$$

Figure 4.4 illustrates this density as a function of Schwarzschild radii R_{g}.

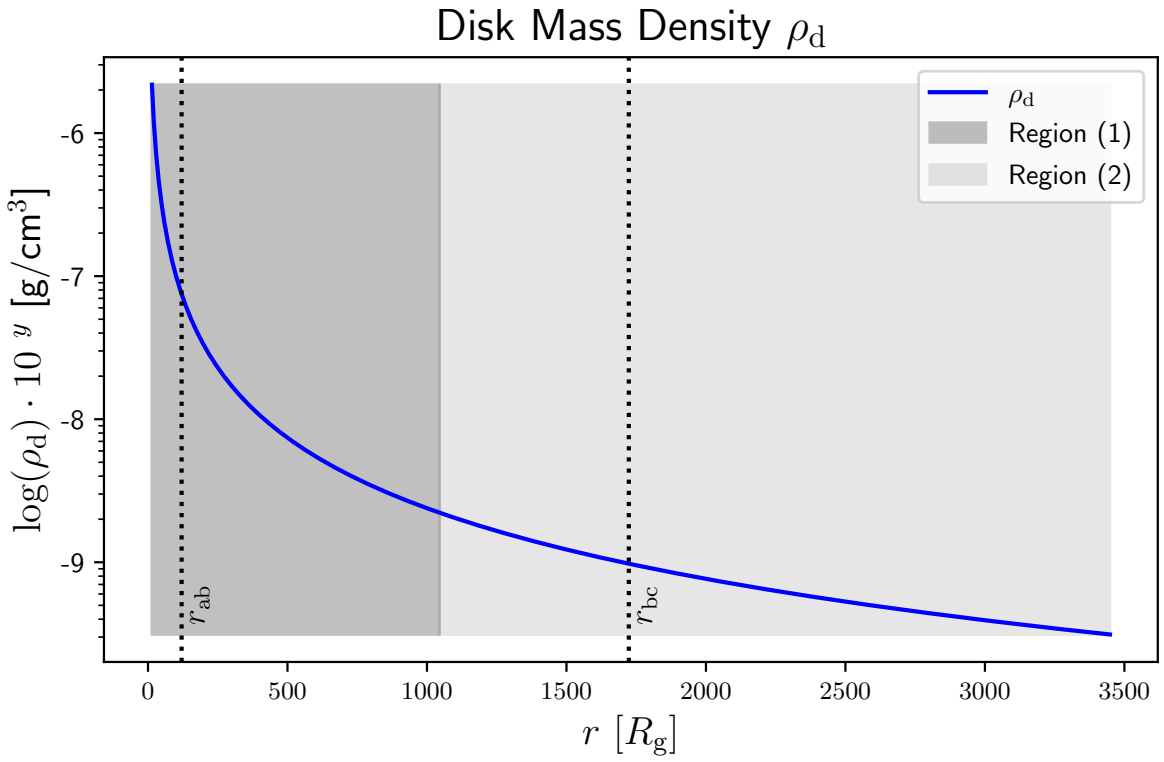

Figure 4.4: Accretion disk volumetric mass density ρ_{d} for an α-model disk (Shakura & Sunyaev, 1973). The density is found by dividing the accretion disk's surface density σ_{d} by $2H_{\mathrm{d}}$ for each region. The dotted vertical black lines indicate the r_{ab} and r_{bc} boundaries of the accretion disk regions, while the shaded areas define the SNC regions (1) (dark gray) and (2) (light gray).

4.3.3 Electron Number Density

Since the disk is assumed to be comprised of hydrogen atoms, which consist of a single proton and electron, the electron number density n_e has the same relation as the particle number density:

$$n_e \left[\mathrm{cm}^{-3}\right] = \begin{cases} 4.3 \times 10^{17} (m_{\mathrm{ss}}\alpha)^{-1} (\dot{m}_{\mathrm{ss}}\tilde{\phi}_{\mathrm{ss}})^{-2} r_{\mathrm{ss}}^{3/2} & r < r_{\mathrm{ab}} \\ 4.2 \times 10^{24} (m_{\mathrm{ss}}\alpha)^{-7/10} (\dot{m}_{\mathrm{ss}}\tilde{\phi}_{\mathrm{ss}})^{2/5} r_{\mathrm{ss}}^{-33/20} & r_{\mathrm{ab}} \leq r < r_{\mathrm{bc}} \\ 3 \times 10^{25} (m_{\mathrm{ss}}\alpha)^{-7/10} (\dot{m}_{\mathrm{ss}}\tilde{\phi}_{\mathrm{ss}})^{11/20} r_{\mathrm{ss}}^{-15/8} & r \geq r_{\mathrm{bc}} \end{cases} \tag{4.17}$$

4.4 Disk Surface Temperature & Luminosity

Under the assumption that the disk is optically thick, the surface temperature of the plasma and the radiation of the disk T_{d} is:

$$T_{\mathrm{d}}[\mathrm{K}] = 2.952 \times 10^{7} (\dot{m}_{\mathrm{ss}}\tilde{\phi}_{\mathrm{ss}})^{1/4} m_{\mathrm{ss}}^{-1/4} r_{\mathrm{ss}}^{-3/4} \tag{4.18}$$

This temperature can be reinterpreted as a luminosity by taking the product of the Stefan-Boltzmann constant $\sigma_{\mathrm{sb}} = 5.67 \times 10^{-5}$ g K^{-4} s^{-3} and T_{d} to the fourth power, and then multiplying the result by the area of an annulus at radius r with unit width dr. This quantity is the luminosity of the disk per unit radius dL_{d} in concentric rings:

$$dL_{\mathrm{d}} = 2\pi r \cdot dr \left(\sigma_{\mathrm{sb}} T_{\mathrm{d}}^{4}\right) \tag{4.19}$$

4.5 Summary

The α-model disk, as described by SS73, is a geometrically thin disk of plasma that orbits a central SMBH with mass $M_{\bullet}$. The gravitational influence of the SMBH and a counteracting pressure force generated by the disk material balance to give the disk a

finite thickness of $2H_{\rm d}$. The rate at which the innermost disk region accretes onto the SMBH is characterized by the parameter $\dot{M}_{\rm d}$ and the dimensionless viscosity parameter α characterizes the outward transfer of angular momentum. The disk can be described by three distinct radial regions that differ in their dominant pressure ($P_{\rm g}$ or $P_{\rm r}$) and opacity ($\sigma_{\rm ff}$ or $\sigma_{\rm T}$). The disk's half-thickness $H_{\rm d}$, surface density $\sigma_{\rm d}$, surface temperature $T_{\rm d}$, luminosity $L_{\rm d}$, mass density $\rho_{\rm d}$, and electron number density n_e, vary for each region and are dependent on α, $\dot{M}_{\rm d}$, $M_\bullet$, and their distance r from the SMBH.

5 Impactor's Mass Gain & Loss from Collision

This section covers an investigation into how much mass is stripped from the impactor by the disk as it completes its transit. An initial attempt to quantify the star-disk collision was made by projecting the star and the disk into 2-dimensions. A model was adapted from Demarque et al. (2008) (hereafter D98) that envisions the Sun as a sphere constructed out of concentric spherical shells, each with their respective densities. The amount of disk material 'swept up' by the impactor was also determined, including a brief look into how much of this material remained bound to the star by calculating the emerging impactor's escape velocity. The surface density of the disk is at its densest when the SMBH is accreting at the Eddington-limit, $\dot{m}_{\rm ss} = 1$, and the viscosity parameter is $\alpha \sim 0.01$. It is at this extreme where the greatest amount of the impactor's outer envelope will be lost to the disk, but the accretion disk does not strip off more than a hundredth of a percent of the impactor's total mass.

5.1 Application - 2D Projection

The Yale Rotating Stellar Evolution Code (hereafter YREC) is a continuously evolving research tool originally developed by Pinsonneault (1988). The model has been evolved from a zero age main sequence (ZAMS) model to the near-age of the Sun (4.5 Gyr) in 50 equal temporal steps. By adjusting the helium abundance and mixing length [4] parameters the model is successfully tuned to achieve almost identical solar radii and masses, such that

$$R_{\odot}^{D98} = 6.96 \times 10^{10} \text{ cm} \qquad \text{and} \qquad M_{\odot}^{D98} = 1.99 \times 10^{33} \text{ g} \tag{5.1}$$

The YREC solar model is used in this work to create a surface mass density profile of a

[4]The mixing length is analogous to the mean-free path for thermodynamics. It is the characteristic length that a fluid parcel will travel, while conserving its initial properties, before mixing with the surrounding fluid.

sun-like star which can be used to estimate the amount of mass removed from the impactor in the event that it collides with an accretion disk. It is assumed that an accretion disk with a given surface density will remove the less dense external regions of the star as it passes through the disk. The point at which the disk's density matches the impactor's density, at that radius, is referred to as the impact parameter, which carves through the entirety of the star to create a path that can be used to infer a stellar column density that determines the stellar mass loss.

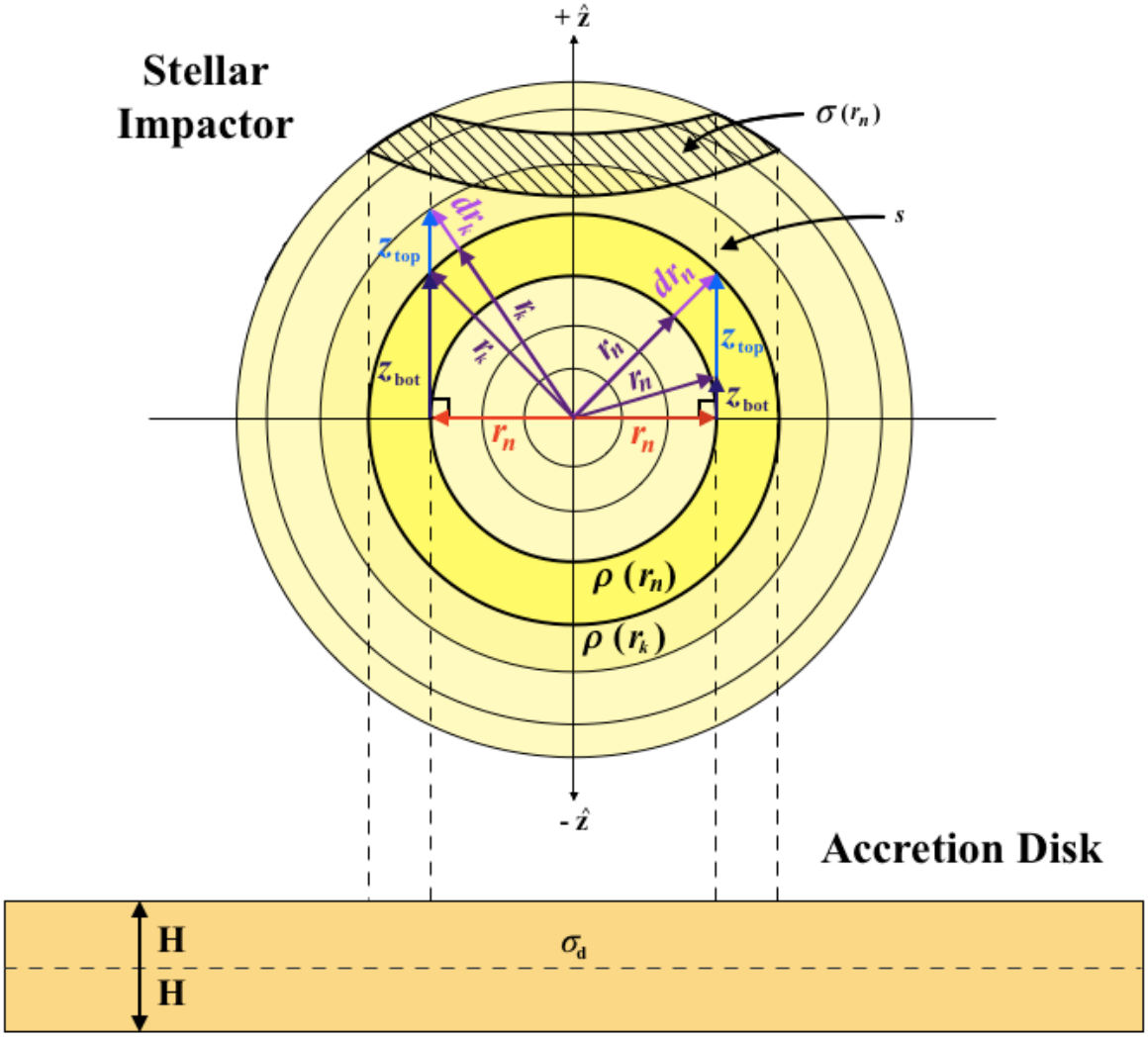

Figure 5.1: Diagram depicting a YREC modelled star colliding with an accretion disk (not to scale) with a mid-plane surface density of $\sigma_{\rm d}$ and a thickness of 2H. The accretion disk removes the outer layers of the star at an impact parameter r_n where $\sigma_{\rm d} < \sigma(r_n)$ at that point, indicated by the dashed line labelled s. The column density $\sigma(r_n)$ through the star is the summation of volume density $\rho(r_k)$ at each radius $r_k \geq r_n$ times the z axis path length s through each radial bin at a given radius $r_k \geq r_n$ with thickness dr_k. The index k is used to indicate the parameters of the shells external to the minimum shell at r_n, such that at the minimum shell the index $k = n$. The spherical shells are projected onto the z axis by applying the Pythagorean theorem to each shell's base r_k and top $r_k + dr_k$, and it is important to note that $z_{\rm bot}$ equates to zero for the minimum shell r_n.

The solar model can be imagined as having a finite number N of normalized radial bins (hereafter shells) r_n with respective densities $\rho(r_n)$, where the subscript n is used to

indicate which shell is being considered. The normalization of these shells was achieved by dividing the radial position r by the YREC model parameter for the solar radius $R_{\odot}^{D98}$.

$$r_n = \frac{r}{R_{\odot}^{D98}} \qquad \text{with} \quad n = 0, 1, 2, \ldots, N \tag{5.2}$$

Each shell has an inner radius of r_n, an outer radius of r_{n+1}, and a thickness of dr_n, such that

$$dr_n = r_{n+1} - r_n \qquad \text{with} \qquad n = 0, 1, 2, \ldots, N \tag{5.3}$$

Since the outermost shell r_N has no upper bound, its thickness dr_N was taken to be that of the second outermost shell dr_{N-1}.

$$dr_N = dr_{N-1} = r_N - r_{N-1} \tag{5.4}$$

The path length s for an impact parameter intersecting a minimum radial bin located at r_n must take into account all shells including and external to r_n. Thus, a summation is required to compute the normalized column density $\sigma(r_n)$ through each external shell r_k with thickness dr_k, where the dummy variable k is used to distinguish between the external and minimum shells.

$$\sigma(r_n) = \sum_{r_k \geq r_n} \rho(r_k) s(r_n, r_k, dr_k) \tag{5.5}$$

The path length s projected onto the z-axis is defined as the difference between the top and bottom z values of the shell, z_{top} and z_{bot}, respectively.

$$s(r_n, r_k, dr_k) = z_{\text{top}} - z_{\text{bot}} \tag{5.6}$$

Projection onto the z-axis is achieved by applying the Pythagorean theorem to the

increasing radial components r_k, as the outer shells are added, and a lower static radial component r_n where the impact parameter intersects.

$$z_{\text{bot}}^2 + r_n^2 = r_k^2 \;\rightarrow\; z_{\text{bot}}^2 = r_k^2 - r_n^2 \;\rightarrow\; z_{\text{bot}} = \sqrt{r_k^2 - r_n^2} \tag{5.7}$$

Here, z_{bot} has a non-zero value for all radii where $r_k > r_n$, and the z value for the top part of the shell is then,

$$\begin{gathered} z_{\text{top}}^2 + r_n^2 = (r_k + dr_k)^2 \;\rightarrow\; z_{\text{top}}^2 = r_k^2 + 2r_k dr_k + dr_k^2 - r_n^2 \\ \rightarrow\; z_{\text{top}} = \sqrt{r_k^2 + 2r_k dr_k + dr_k^2 - r_n^2} \end{gathered} \tag{5.8}$$

When the star passes through the accretion disk, we assume that the portion of the star that is stopped by the disk is that which has a lower column density than the disk. This location, determined by the impact parameter, occurs at some given minimum shell and all shells including and external to r_n are removed from the star. A single shell contains mass $M(r_n)$ proportional to the product of its annular surface area $A(r_n)$ and $\sigma(r_n)$, due to a path intersecting it and all external shells r_k.

$$M(r_n) = \sigma(r_n)A(r_n) = \sigma(r_n)\pi\left(r_{n+1}^2 - r_n^2\right) \tag{5.9}$$

Due to the nature of the outermost shell not having a finite upper bound at r_{N+1}, the thickness of the second outermost shell was used to estimate an upper bound.

$$r_{N+1} = r_N + dr_N = r_N + dr_{N-1} = r_N + (r_N - r_{N-1}) = 2r_N - r_{N-1} \tag{5.10}$$

Since each shell has distinct density profiles and thicknesses, each shell contributes a different amount of mass to the total mass lost $M_s(r_n)$. Thus a summation is required to

add each external mass portion $M(r_k)$ to the minimal mass portion located at r_n, where the dummy variable k is again used to distinguish between the minimum and external portions.

$$M_s(r_n) = \sum_{r_k \geq r_n} M(r_k) = \sum_{r_k \geq r_n} \sigma(r_k) A(r_k) \tag{5.11}$$

A reference table containing r_n, $\sigma(r_n)$, and $M(r_n)$ can be used to compare an accretion disk's surface-mass density σ_d to the column densities through the star at each projected radius r_n, and to read off the associated mass lost for each r_n. The minimum r_n with $\sigma(r_n) > \sigma_d$ is the largest r_n that survives the star-disk collision without being stripped off the star. Since $\sigma(r_n)$ was determined using normalized radial values, the normalization must be removed to ensure a more accurate value $\sigma_s(r_n)$ for comparison. This is done by multiplying each result by the YREC model parameter for the solar radius $R_\odot^{D98}$.

$$\sigma_s(r_n) \left[\frac{\mathrm{g}}{\mathrm{cm}^2}\right] = \sigma(r_n) R_\odot^{D98} \tag{5.12}$$

These normalized radial values are also propagated into the mass equations, yielding nonsensical results. The total mass lost can be given in proper units of mass, $M_l(r_n)$, by removing the propagated normalization from $M_s(r_n)$, which is achieved by multiplying the results by the cube of $R_\odot^{D98}$.

$$M_l(r_n)\,[\mathrm{g}] = M_s(r_n) \left(R_\odot^{D98}\right)^3 \tag{5.13}$$

It may be useful to have $M_l(r_n)$ normalized to easily see the fractional mass lost from the star. This normalization $\mathring{M}_l(r_n)$, where the accent $\circ$ has been used to denote normalization, is achieved by dividing $M_l(r_n)$ by the YREC model parameter for the solar mass $M_\odot^{D98}$.

$$\mathring{M}_l(r_n) = \frac{M_l(r_n)}{M_\odot^{D98}} \tag{5.14}$$

Using these newly adjusted quantities the reference table for stellar-disk collisions can be redrawn to list the minimum shell r_n, the projected column density through the star $\sigma_s(r_n)$, the total amount of mass stripped from the star $M_l(r_n)$, and the fractional (normalized) amount of mass stripped from the star $\mathring{M}_l(r_n)$. The table's format is illustrated in Table 5.1

n	r_n	$\sigma_s(r_n)$	$M_l(r_n)$	$\mathring{M}_l(r_n)$
–	–	[g/cm^2]	[g]	–
0	r_0	$\sigma_s(r_0)$	$M_l(r_0)$	$\mathring{M}_l(r_0)$
1	r_1	$\sigma_s(r_1)$	$M_l(r_1)$	$\mathring{M}_l(r_1)$
$\vdots$	$\vdots$	$\vdots$	$\vdots$	$\vdots$
N	r_N	$\sigma_s(r_N)$	$M_l(r_N)$	$\mathring{M}_l(r_N)$

Table 5.1: Illustration of the formatting for the reference table used to determine the amount of mass stripped from a star when it collides with an accretion disk. The accretion disk's surface density $\sigma_{\rm d}$ is compared to the column-density $\sigma_s(r_n)$ through the star at a projected radius r_n, a value which decreases at all $r_n > 0$. The smallest r_n where $\sigma_s(r_n) > \sigma_{\rm d}$ is the largest r_n that survives the collision without being removed from the star. The amount of mass removed from the star at r_n is listed in the final two columns as either the total mass lost $M_l(r_n)$ or the fractional mass lost $\mathring{M}_l(r_n)$

The total mass gained by the star from the accretion disk, $M_g(r_n)$ is the amount "pushed" out of the disk by the remaining inner shells of the star. This amount of mass added to the star is determined by taking the product of the disk's mid-plane surface density $\sigma_{\rm d}$, the area of a circle with radius $r_n = r_{min}$, and the square of the YREC model solar radius $R_\odot^{D98}$ to remove the normalization.

$$M_g(r_n) = \pi\sigma_{\rm d}\left(r_n R_\odot^{D98}\right)^2 \tag{5.15}$$

The fractional (normalized) mass gained, $\mathring{M}_g(r_n)$, can be found by dividing M_g by the YREC model solar mass.

$$\mathring{M}_g = \frac{M_g(r_n)}{M_\odot^{D98}} \tag{5.16}$$

With the accretion disk surface densities for the radial region boundaries, $r_{\rm ab}$ and $r_{\rm bc}$, derived in Table 4.2, the corresponding mass that is stripped away from the star can be determined. It was assumed that the central Schwarzschild SMBH ($\eta = 0.06$) had a mass of $M_\bullet = 10^8 M_\odot$, while the accretion disk had $\dot{m}_{\rm ss} = (0.1, 1)$ and $\alpha = (0.01, 0.1, 1)$. The amount of mass lost and gained by the star that is associated with these parameters are provided in Table 5.2, and Figure 5.2 provides a graphical representation of the fractional mass lost.

$\dot{m}_{\rm ss}$	α	Region	r_n	$M_l(r_n)$ [g] $\times 10^{25}$	$\mathring{M}_l(r_n)$ $\times 10^{-8}$	$M_g(r_n)$ [g] $\times 10^{26}$	$\mathring{M}_g(r_n)$ $\times 10^{-8}$	n
0.1	0.01	$\sigma_{\rm a}(r_{\rm ab})$	0.9858	197	41.4	637	3200	169
		$\sigma_{\rm b}(r_{\rm ab})$	0.9858	197	414	634	3190	169
		$\sigma_{\rm b}(r_{\rm bc})$	0.9917	24.0	50.5	133	669	186
		$\sigma_{\rm c}(r_{\rm bc})$	0.9917	24.0	50.5	129	646	186
	0.1	$\sigma_{\rm a}(r_{\rm ab})$	0.9927	14.6	30.7	90.0	452	190
		$\sigma_{\rm b}(r_{\rm ab})$	0.9927	14.6	30.7	89.5	450	190
		$\sigma_{\rm b}(r_{\rm bc})$	0.9952	2.51	5.29	21.2	107	204
		$\sigma_{\rm c}(r_{\rm bc})$	0.9953	2.22	4.67	20.5	103	205
	1	$\sigma_{\rm a}(r_{\rm ab})$	0.9959	1.34	2.81	12.6	63.3	209
		$\sigma_{\rm b}(r_{\rm ab})$	0.9959	1.34	2.81	12.5	63.0	209
		$\sigma_{\rm b}(r_{\rm bc})$	0.9973	0.253	0.533	3.38	17.0	222
		$\sigma_{\rm c}(r_{\rm bc})$	0.9973	0.253	0.533	3.27	16.4	222
1	0.01	$\sigma_{\rm a}(r_{\rm ab})$	0.9843	286	602	891	4480	166
		$\sigma_{\rm b}(r_{\rm ab})$	0.9843	286	602	867	4460	166
		$\sigma_{\rm b}(r_{\rm bc})$	0.9904	44.6	93.9	211	1060	181
		$\sigma_{\rm c}(r_{\rm bc})$	0.9904	44.6	93.9	204	1020	181
	0.1	$\sigma_{\rm a}(r_{\rm ab})$	0.9918	24.0	50.5	126	632	186
		$\sigma_{\rm b}(r_{\rm ab})$	0.9920	21.2	44.6	125	630	187
		$\sigma_{\rm b}(r_{\rm bc})$	0.9946	4.16	8.77	33.7	169	200
		$\sigma_{\rm c}(r_{\rm bc})$	0.9946	4.16	8.77	32.6	164	200
	1	$\sigma_{\rm a}(r_{\rm ab})$	0.9955	1.95	4.11	17.6	88.6	206
		$\sigma_{\rm b}(r_{\rm ab})$	0.9955	1.95	4.11	17.5	88.2	206
		$\sigma_{\rm b}(r_{\rm bc})$	0.9969	0.424	0.892	5.36	27.0	218
		$\sigma_{\rm c}(r_{\rm bc})$	0.9969	0.424	0.892	5.18	26.1	218

Table 5.2: The amount of mass lost from a star that collides with a Shakura & Sunyaev (1973) α-model accretion disk at the radial region boundaries $r_{\rm ab}$ and $r_{\rm bc}$. It is assumed that a central SMBH with a mass of $M_\bullet = 10^8 M_\odot$ is orbited by an accretion disk with a relative accretion rate of $\dot{m}_{\rm ss} = (0.1, 1)$, and an angular momentum transfer efficiency of $\alpha = (0.01, 0.1, 1)$. Three significant figures have been used for most values, except for r_n where four have been used to show the differing values.

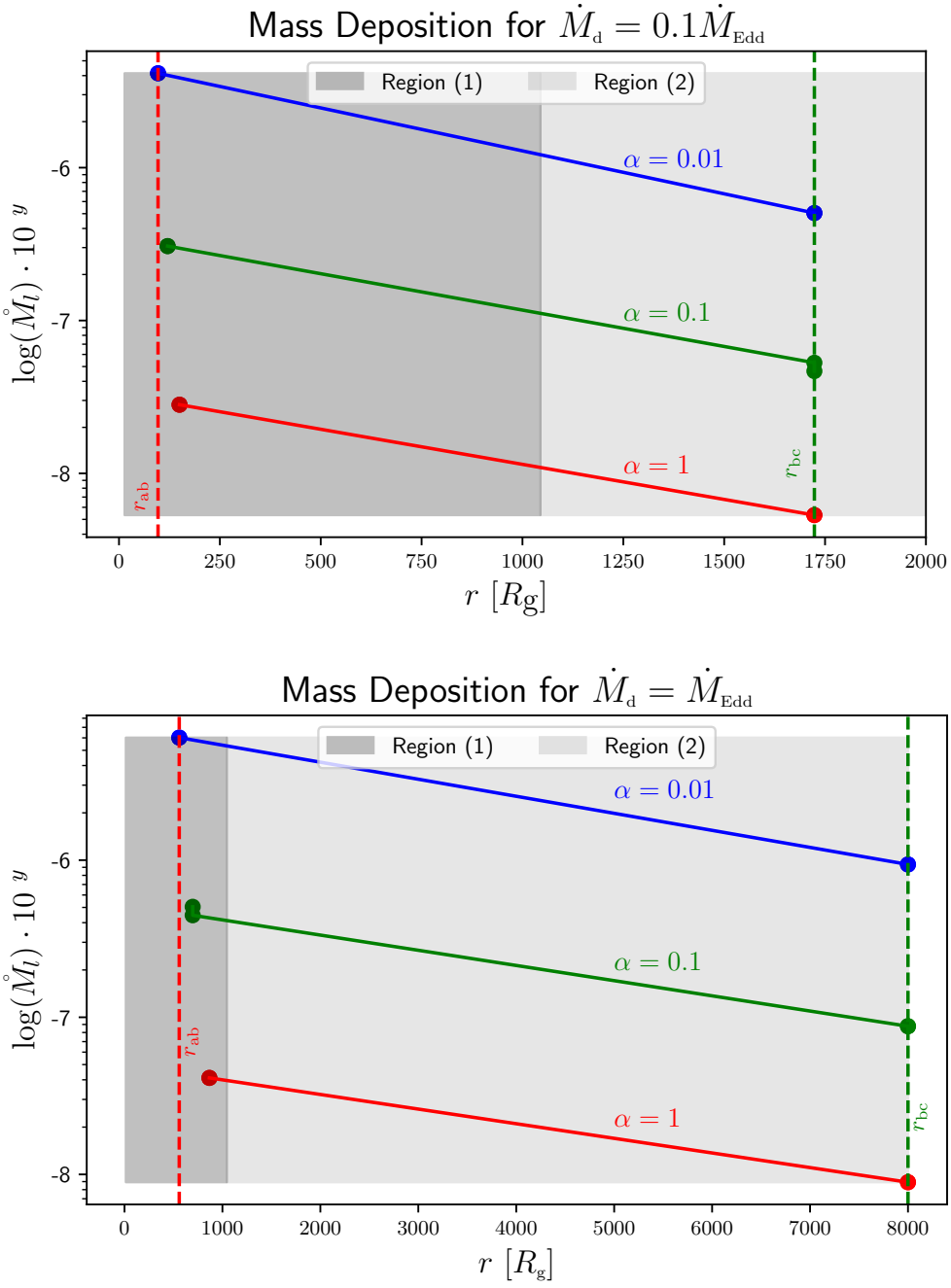

Figure 5.2: The logarithmic fractional amount of mass stripped from a star colliding with a SS73 α-model accretion disk at the radial region boundaries $r_{\rm ab}$ and $r_{\rm bc}$, represented in Schwarzschild radii $R_{\rm g}$, for different values of the α parameter, a non-rotating SMBH ($\eta = 0.06$) mass of $M_\bullet = 10^8 M_\odot$, and a relative mass accretion rate of $\dot{m}_{\rm ss} = 0.1$ (first panel) and $\dot{m}_{\rm ss} = 1$ (second panel). The coloured circles represent the amount lost at each boundary, with the leftmost being at $r_{\rm ab}$ and the rightmost being $r_{\rm bc}$, and the solid lines provide a visual aid to connect these points. The dashed vertical lines represent the disk's regional boundaries, $_{\rm ab}$ and $r_{\rm bc}$, and the shaded regions represent the SNC regions (1) (dark gray) and (2) (light gray) in the work of PC07.

The dotted vertical black lines indicate the $r_{\rm ab}$ and $r_{\rm bc}$ boundaries of the accretion disk regions, while the shaded areas define the SNC regions (1) (dark gray) and (2) (light gray).

5.2 Escape Velocity

The disk material that is 'swept up' by the impactor may be too energetic to be gravitationaly bound to the emerging star. Thus, the temperature of the matter is approximated for the impactor after it has completed its transit of the disk by taking into account the Maxwell-Boltzmann distribution and the escape velocity.

The escape velocity v_∞ for a spherically symmetric body of mass M and radius R is

$$v_\infty = \sqrt{2\frac{GM}{R}} \tag{5.17}$$

For a star with solar parameters the escape velocity is

$$v_\infty = \sqrt{2\frac{GM_\odot}{R_\odot}} \sim 6.176747 \times 10^7 \ \frac{\rm cm}{\rm s} \tag{5.18}$$

While the different solar parameters of the YREC model, $M_\odot^{D98}$ and $R_\odot^{D98}$, are not enough to make a significant difference.

$$v_\infty = \sqrt{2\frac{GM_\odot^{D98}}{R_\odot^{D98}}} \sim 6.176754 \times 10^7 \ \frac{\rm cm}{\rm s} \tag{5.19}$$

A star that collides with an accretion disk would emerge with a change in its mass and shape (see Table 5.2). For the fiducial values, a YREC model star impacting the disk at region (a) along the $r_{\rm ab}$ boundary with surface density $\sigma_{\rm a}(r_{\rm ab})$ would result in a net gain

of mass but loss of radial extent. The resultant escape velocity would then become

$$v_\infty = \sqrt{2\frac{GM_\odot^{D98}\,(1+2.786\times10^{-5})}{R_\odot^{D98}\cdot 0.9858}} \sim 6.22\times10^7\ \frac{\text{cm}}{\text{s}} \sim 622\ \frac{\text{km}}{\text{s}} \tag{5.20}$$

The Maxwell-Boltzmann distribution is a probability distribution that describes the velocity v of a particle with mass m in an idealized gas of temperature T. The particle's motion can be described by its mean speed $\langle v\rangle$, most probable speed v_p, and root-mean-squared speed v_rms. The temperature associated with each speed can be determined by solving for T in each of the relations.

$$T = \begin{cases} m\pi\langle v\rangle^2/(8k_B) \\ mv_\text{p}^2/(2k_B) \\ mv_\text{rms}^2/(3k_B) \end{cases} \tag{5.21}$$

The escape velocity of the sun-like star, v_∞, before crossing the accretion disk was determined in Equation (5.18), here it is referred to as the initial escape velocity v_0. The temperature associated with this velocity is found for each differing speed value, where m is taken to be the mass of a proton $m_\text{p} = 1.672\times10^{-24}$ g.

$$T(v_0) \approx \begin{cases} 1.815\times10^7\ \text{K} & \text{if } v_0 = \langle v\rangle \\ 2.311\times10^7\ \text{K} & \text{if } v_0 = v_\text{p} \\ 1.541\times10^7\ \text{K} & \text{if } v_0 = v_\text{rms} \end{cases} \tag{5.22}$$

These temperatures are about four orders of magnitude larger than the surface (photospheric) temperature of the Sun, $T_\odot = 5778$ K.

The escape velocity of the star after crossing the accretion disk was determined in Equation (5.20), here it is referred to as the final escape velocity v_f. The associated

temperatures are determined as they were for the initial condition and have nearly the same values.

$$T(v_{\rm f}) \approx \begin{cases} 1.841 \times 10^7 \text{ K} & \text{if } v_{\rm f} = \langle v \rangle \\ 2.344 \times 10^7 \text{ K} & \text{if } v_{\rm f} = v_{\rm p} \\ 1.563 \times 10^7 \text{ K} & \text{if } v_{\rm f} = v_{\rm rms} \end{cases} \tag{5.23}$$

Thus protons that are hotter than these final temperatures would escape the emerging impactor and not contribute to the total amount of mass swept up by the star.

For the fiducial parameters at radii $r = (100, 500, 2000) R_{\rm g}$, the surface temperature of the disk is

$$T_{\rm d}[{\rm K}] = 2.952 \times 10^7 (\dot{m}_{\rm ss} \tilde{\phi}_{\rm ss})^{1/4} m_{\rm ss}^{-1/4} r_{\rm ss}^{-3/4} \sim (11.4, 3.51, 1.25) \times 10^3 \text{ K} , \tag{5.24}$$

and the characteristic temperature of the shock, Eq. (6.2), is

$$T_{\rm char} = \frac{2}{3} \frac{\mu v_{\rm rel}^2}{2 k_B} \sim (181, 36.3, 9.07) \times 10^8 \text{ K} \tag{5.25}$$

where $\mu = m_{\rm p}/2$ is the mean particle mass in the shocked gas. Clearly, $T_{\rm char} > T(v_{\rm f}) > T(v_0) > T_{\rm d}$ and some large portion (which is not worked out in this report) of the mass (modelled as protons) would escape the emerging impactor.

5.3 Summary

The amount of mass that the accretion disk is able to strip off a sun-like impactor passing through the disk's regional boundaries, $r_{\rm ab}$ and $r_{\rm bc}$ is at most $\sim 0.0004\%$ and $\sim 0.00009\%$ of the star's total mass, respectively, which occurs when the disk has a viscosity parameter of $\alpha = 0.01$ and is accreting at $\dot{m}_{\rm ss} = 0.1$ and 1. Lower values of α and larger values of $\dot{m}_{\rm ss}$ tear more matter away from the star and thus help to generate a denser disk.

No matter what the disk parameter is set to, more gas is pushed out of the disk from a star passing through the disk than what it loses to the disk, and more mass is stripped from a star passing through the disks inner boundary $r_{\rm ab}$ than its outer boundary $r_{\rm bc}$.

The amount of disk material that is pushed out of the disk by the star does not all stay bound to the star. For a star impacting the disk at $100R_{\rm g}$, the disk material, which is assumed to be made up of protons, is shock heated to a temperature of $T_{\rm char} \sim 181$ K. After the star emerges from the disk, with a slightly smaller radius and larger mass, its escape velocity for protons having the most probable speed $v_{\rm p}$ is associated with a temperature of $T(v_{\rm p}) \sim 2.3 \times 10^7$ K. Since $T_{\rm char} > T(v_{\rm p})$, most of the shocked protons will possess temperatures that are greater than that of the star's escape temperature, and thus full back onto the disk.

This model is designed for a sun-like star, and thus cannot be extended to other spectral classes of stars on the main sequence. It also does not account for different orbital inclination angles or eccentricities of the impactor. Furthermore, the travel time through the disk is not considered as the two-dimensional collision is modelled as an instantaneous impact. However, the travel time and its effects are calculated in §7 where the collisional model is three-dimensional.

6 Collisional Model

A 3-dimensional model details a thin circular disk lying along the xy-plane being struck by a star with given orbital parameters. This collision, due to the thickness of the disk and the relative velocity between the two objects, occurs in three distinct stages: (1) a bright initial flare, (2) a dimmer glow while the star is embedded within the disk, and (3) a fading afterglow after the star has emerged from the disk. The orbital energy lost by the star along with the rate of stellar-collisions is used to determine a time-averaged collisional luminosity that can be compared to the accretion disk's surface luminosity. The relative velocity and loss of orbital energy are more affected by the orbital inclination. The eccentricity of the impactor's orbit does not seem to play a significant role in the transfer of energy, whereas the orbital inclination influences the orbital energy loss by ~ 1.5 orders of magnitude. Depending on the radial impact location, the time-averaged collisional luminosity is significantly brighter than our sun-like star's surface, $L_c \sim 10^{50} - 10^{55}$ erg s^{-1} $R_{\rm g}^{-1}$, but still a couple of magnitudes dimmer than the accretion disk's surface. However, this luminosity is a result of many star-disk collisions occuring within a specified area of the disk.

The stars populating the SNC are assumed to share a single stellar mass $M_\star$ and stellar radius $R_\star$, and a spherical, power-law stellar distribution (see §3). The stellar orbits within the cluster are defined by a basis of orbital elements with respective ranges:

- semimajor axis, $a = (0, \infty)$
- eccentricity, $e = [0, 1)$
- longitude of ascending node, $\Omega = (-\pi, \pi]$
- argument of periapsis, $\omega = (-\pi, \pi]$
- inclination, $I = [0, pi)$, where $0 \leq I < \pi/2$ are "prograde", implying that both the

angular momentum of the disk and stellar orbit have positive Z-components, and $\pi/2 < I < \pi$ are "retrograde".

- true anomaly, $f = -\omega$ and $f = -\omega + \pi$, since only the positions and velocities at the node crossings are of concern.

Figure 6.1 illustrates a star impacting the accretion disk. The star has an orbital inclination of $I \approx \pi/2$ and a bound orbital eccentricity of $e = 1$.

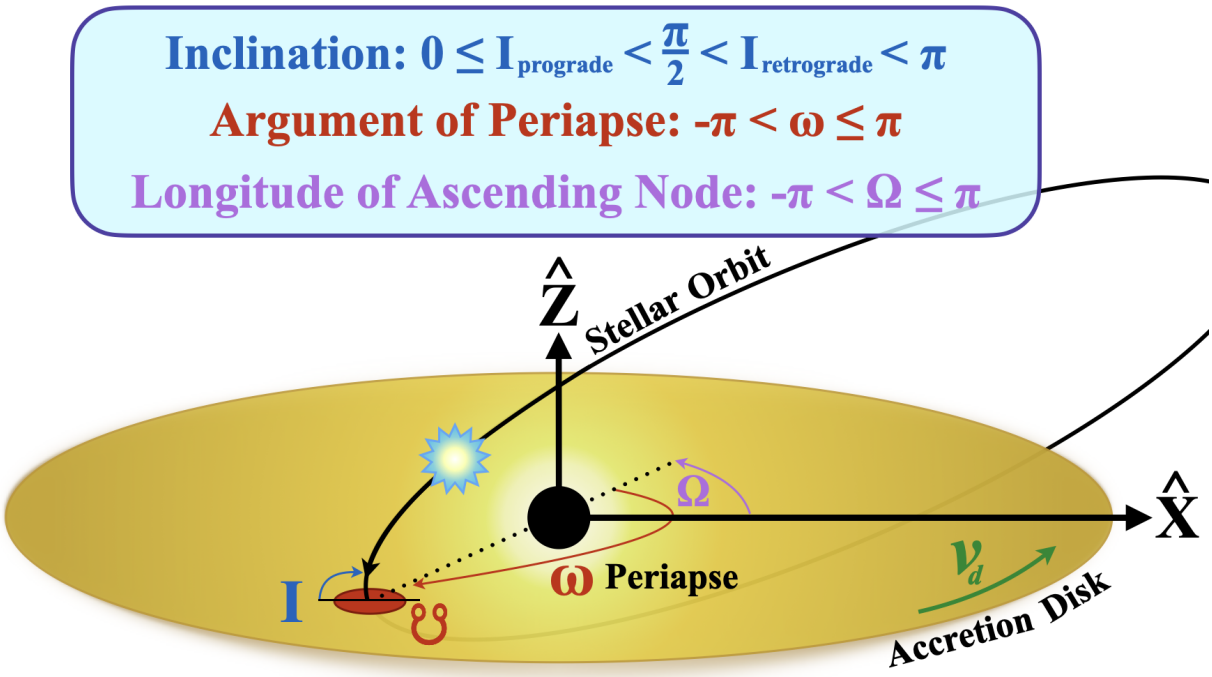

Figure 6.1: The depicted impactor strikes the disk while on a parabolic orbit ($e = 1$), and due to its inclination ($I \approx \pi/2$) its motion relative to the disk is neither prograde nor retrograde. Since the disk is azimuthally symmetric, the location of Ω is insignificant for all collisions.

6.1 Stages

The star-disk collision can be divided up into distinct stages (Nayakshin et al., 2004). It is assumed that the impactor is a rigid solid body, and both the accretion of gas onto the impactor and the tidal interactions between the impactor and the gas in impactor's wake

are neglected. The star drives a bow shock into the disk with Mach number of

$$\mathcal{M} = \frac{v_\star}{v_\mathrm{s}} \simeq \sqrt{\frac{T_\mathrm{char}}{T_\mathrm{d}}} \simeq 10^3 \tag{6.1}$$

where T_char is the characteristic temperature, defined as the max temperature to which the gas is shock heated:

$$T_\mathrm{char} = \frac{2}{3}\frac{\mu v_\mathrm{rel}^2}{2k_B} = 1.8 \times 10^8 \left(\frac{10^4\ R_\mathrm{g}}{R_\mathrm{d}}\right)\ \mathrm{K} \tag{6.2}$$

where mean particle mass in shocked gas is $\mu = m_\mathrm{p}/2$ and $R_\mathrm{d} \sim 10^4\ R_\mathrm{g}$ is the outermost disk radius.

For an optically thick disk the collision can be divided into 3 distinct stages:

1. X-ray Flare: The impactor is within the accretion disk's photosphere where the X-rays generated from the shocked gas are visible to an outside observer. The shock may be obscured by the impactor itself depending on whether the impactor is entering or exiting the disk. If the star is moving away from the observer then the leading edge of the bow shock is obscured from the observer by the star, and vice versa if the impactor is moving towards the observer.

2. Thermal Burst: The impactor is within the optically thick part of disk, where the X-rays generated from the shocked gas are absorbed within the disk and re-emitted as thermal radiation in the infrared (IR) and the visual (V) parts of the electromagnetic spectrum.

3. Afterglow: The impactor has emerged from the accretion disk and is many $R_\star$ away from it, and the X-ray emitting gas has cooled down to $T < 10^7$ K and is no longer observable due to absorption from the interstellar medium (ISM). The patch of the disk around the track of the impactor is "hot" relative to the unperturbed disk, and

most of the cooling is by black-body emission.

It is important to recognize that if the accretion disk is optically and spatially thin $H_{\rm d} \ll r$ the X-rays generated from the shock will always be visible to an outside observer, and the second collisional stage will not occur.

6.2 Relative Velocity

Starting at apoapse, the stellar orbit makes an initial pass through the disk on the way to its periapse passage and a secondary passing after (illustrated in Figure 6.1).

It is assumed that the disk is thin ($H_{\rm d} \ll r$), such that disk crossings (at $z = 0$ in the disk reference frame) occur over a small arc length of the stellar orbit near the nodes. The stellar orbital elements are used to compute the position $\vec{x}_\star$ and velocity $\vec{v}_\star$ of the star at the node crossings, and the relative velocity $\vec{v}_{\rm rel}$ between the disk and star velocities, $\vec{v}_\star$ and $\vec{v}_{\rm d}$ respectively, is:

$$\vec{v}_{\rm rel} = \vec{v}_\star - \vec{v}_{\rm d} \tag{6.3}$$

The calculated relative velocities of a single stellar crossing as a function of r for varying inclination angles (where $e = 0$) and eccentricities (where $I = \pi/2$) are both plotted in Figure 6.2.

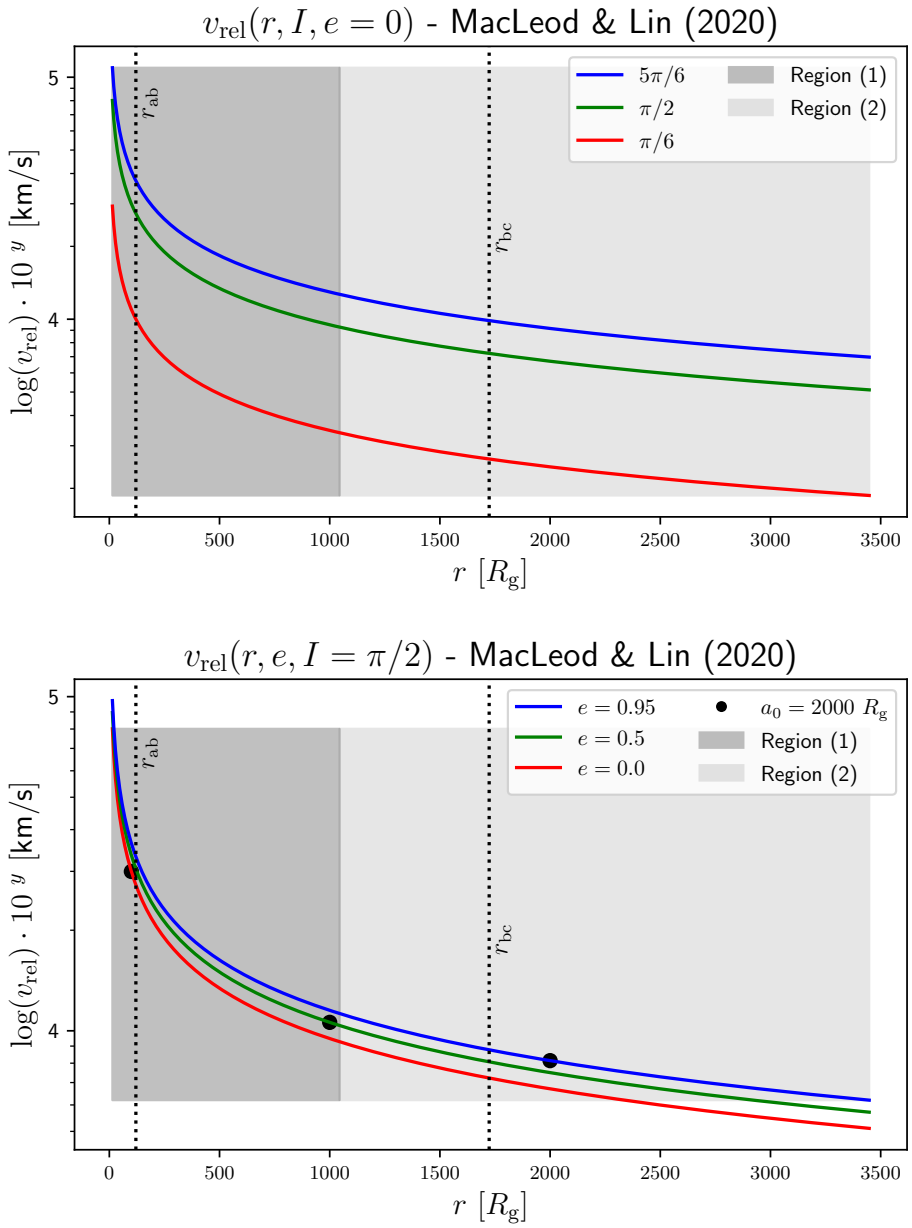

Figure 6.2: Logarithmic relative velocity of a stellar impact for varying inclination angles I (first-panel) and eccentricities e (second-panel), as functions of the radial collision site in terms of Schwarzschild radii $R_{\rm g} \sim 3 \times 10^{13}$ cm. The impactors are assumed to have an argument of periapsis $\omega = 0$ (impact location is at the star's periapse), and the BH mass is $M_\bullet = 10^8 M_\odot$. For the first plot, the stars are assumed to be descending into the disk with eccentricity $e = 0$ (circular orbits). Whereas for the second plot, the stars are assumed to be descending into the disk with inclination $I = \pi/2$ (face-on or perpendicular impacts), and the black dots represent the radial position for a fixed semimajor axis of $a = 2000\ R_{\rm g}$ for the different eccentricities, which are 2000 $R_{\rm g}$ for $e = 0$, 1000 $R_{\rm g}$ for $e = 0.5$, and 100 $R_{\rm g}$ for $e = 0.95$. The dotted vertical black lines indicate the accretion disk's regional boundaries, $r_{\rm ab}$ and $r_{\rm bc}$, while the shaded areas are the SNC's regions (1) (dark gray) and (2) (light gray). The code to generate the plot was provided by the authors MacLeod & Lin (2020).

It is found that different orbital inclination angles have a greater effect on the relative velocity than different orbital eccentricities. While keeping the impactor's orbital eccentricity fixed at $e = 0$, those following retrograde orbits have the largest $v_{\rm rel}$ and those following prograde orbits have the smallest $v_{\rm rel}$. The angular difference between the face-on ($I = \pi/2$) collision and the prograde and retrograde collisions is the same at $\Delta I = \pi/3$. However, these two cases differ in $v_{\rm rel}$, where the prograde orbits experience a far weaker $v_{\rm rel}$ than retrograde orbits for the same angular deviation from $I = \pi/2$. The disk's velocity is assumed to be entirely in the xy-plane of the disk in the azimuthal θ-direction. Thus, stars along prograde orbits share similar xy-velocity components with the disk matter which explains the much slower $v_{\rm rel}$, as opposed to stars along retrograde orbits having xy-velocity components directed oppositely to that of the accretion disk's.

While keeping the orbital inclination angle fixed at $I = \pi/2$ impactors with circular Keplerian orbits ($e = 0$) have smaller relative velocities than those with highly eccentric orbits ($e = 0.95$), where it is assumed that the star-disk collision happens at periapse when the impactor has an eccentric orbit. For an impactor with a fixed semi-major axis of $a = 2000R_{\rm g}$, its radial position is $r = (2000, 1000, 100)R_{\rm g}$ for orbital eccentricities of $e = (0, 0.5, 0.95)$, respectively, which is indicated in the bottom plots of Figure 6.2 by the black dots.

An orbiting body travels fastest at its periapse, so the speed at which an impactor transits the disk is greater for more eccentric orbits. With an impact of $I = \pi/2$ most of the stellar velocity is in the z-direction, which is the direction where the disk's velocity component is zero, and larger values of e will increase the impactor's z-velocity component and reduce its xy-velocity components. Before $v_{\rm rel}$ is calculated the stellar velocity is projected into the plane of the disk using Euler angle transformations and its z-velocity component is set to zero. Thus, the stars with more eccentric orbits, and hence smaller xy-velocity components, have faster $v_{\rm rel}$ due to their larger z-velocity components.

6.3 Specific Orbital Energy

For a collision at a given orbital inclination I, the change in a star's velocity is given by MacLeod & Lin (2020) as

$$\Delta\vec{v}_\star = -\frac{F_{\rm drag}}{M_\star}\frac{2H_{\rm d}}{v_{\star,z}\sin(I)}\frac{\vec{v}_{\rm rel}}{|\vec{v}_{\rm rel}|} \tag{6.4}$$

where $H_{\rm d}$ is the mid-plane disk height, $\Delta\vec{v}_\star$ is the stellar change in velocity after passing through the disk, and $F_{\rm drag}$ is the drag force felt by the star. The author's also provide a relationship for the change in specific orbital energy experienced by a star striking the disk with a periapse velocity $v_{\rm per.}$ as

$$\Delta\mathcal{E} \approx 2H_{\rm d}\frac{F_{\rm drag}}{M_\star} = \frac{\Delta m}{M_\star}v_{\rm per.}^2 \tag{6.5}$$

However, if the stellar crossing is assumed to occur over a small arc length the interaction is more like an impulse where $r_i \approx r_f$, such that the change in specific orbital energy can be written as,

$$\Delta\mathcal{E} = \frac{v_f^2}{2} - \frac{GM_\bullet}{r_f} - \frac{v_i^2}{2} + \frac{GM_\bullet}{r_i} \approx \frac{1}{2}\left(v_f^2 - v_i^2\right) = \frac{\Delta v_\star}{2}\left(v_f + v_i\right) \tag{6.6}$$

Due to the impulse approximation the final bracketed term is assumed to be twice the vertical stellar velocity,

$$\Delta\mathcal{E} \approx \frac{\Delta v_\star}{2}\left(v_f + v_i\right) \approx \frac{\Delta v_\star}{2}\,2v_{\star,z} = (\Delta v_\star)(v_{\star,z}) \tag{6.7}$$

Thus the change in specific orbital energy can be substituted into for the change in velocity as follows,

$$\Delta\mathcal{E} \approx -\frac{F_{\rm drag}}{M_\star}\frac{2H_{\rm d}}{\sin(I)}\frac{\vec{v}_{\rm rel}}{|\vec{v}_{\rm rel}|} \tag{6.8}$$

where the $v_{\star,z}$ terms have cancelled.

The orbital energy of an impactor is reduced after a successful transit of the disk, so the change has a negative value. Impactors, with highly inclined orbits that strongly deviate from $I = 90°$ without being in the disk plane, passing through disks with a large $H_{\rm d}$ will be slowed down the most and thus experience the greatest loses in their specific orbital energy. A substantial drag force and relative velocity will also greatly reduce an emerging impactor's specific orbital energy and velocity, but these two quantities are somewhat intertwined.

The drag force experienced by the star is either the geometric or gravitational cross-section of the impacting star, depending on the magnitude of the relative velocity,

$$F_{\rm drag} \approx \begin{cases} \pi R_\star^2 \rho_{\rm d} |\vec{v}_{\rm rel}|^2 & \text{Geometric when } |\vec{v}_{\rm rel}| \gg \sqrt{GM_\star/R_\star} \\ 4\pi (GM_\star)^2 \rho_{\rm d}/|\vec{v}_{\rm rel}|^2 & \text{Gravitational when } |\vec{v}_{\rm rel}| \ll \sqrt{GM_\star/R_\star} \end{cases} \tag{6.9}$$

The initial $\mathcal{E}_i$ and final $\mathcal{E}_f$ energies to compute $\Delta\mathcal{E}_{M_\star}$ are calculated as so,

$$\Delta\mathcal{E}_{M_\star} = \mathcal{E}_f - \mathcal{E}_i = \left(-G\frac{M_\bullet}{2a_f}\right) - \left(-G\frac{M_\bullet}{2a_i}\right) \tag{6.10}$$

where a_i and a_f are the initial and final semimajor axes of the stellar orbit. By employing $\Delta\vec{v}_\star$, the final stellar velocity $\vec{v}_f = \vec{v}_\star + \Delta\vec{v}_\star$ is computed before combining it with the final radial position $\vec{r}_f$, to calculate a_f

$$a_f = \left(\frac{2}{|\vec{r}_f|} - \frac{|\vec{v}_f|}{GM_\bullet}\right)^{-1} \tag{6.11}$$

Since the $\Delta\mathcal{E}_{M_\star}$ is the *specific* orbital energy, the absolute change in orbital energy

$|\Delta\mathcal{E}|$ is equal to the change in specific orbital energy multiplied by unit solar mass.

$$|\Delta\mathcal{E}| \quad \left[\frac{\mathrm{g\ cm^2}}{\mathrm{s^2}}\right] = |\Delta\mathcal{E}_{M_\star}| \times M_\star \tag{6.12}$$

Figure 6.3 illustrates the absolute change in orbital energy due to a single stellar impact for varying inclination angles and orbital eccentricities, as a function of the radial position of the impact site within the disk for the fiducial parameters.

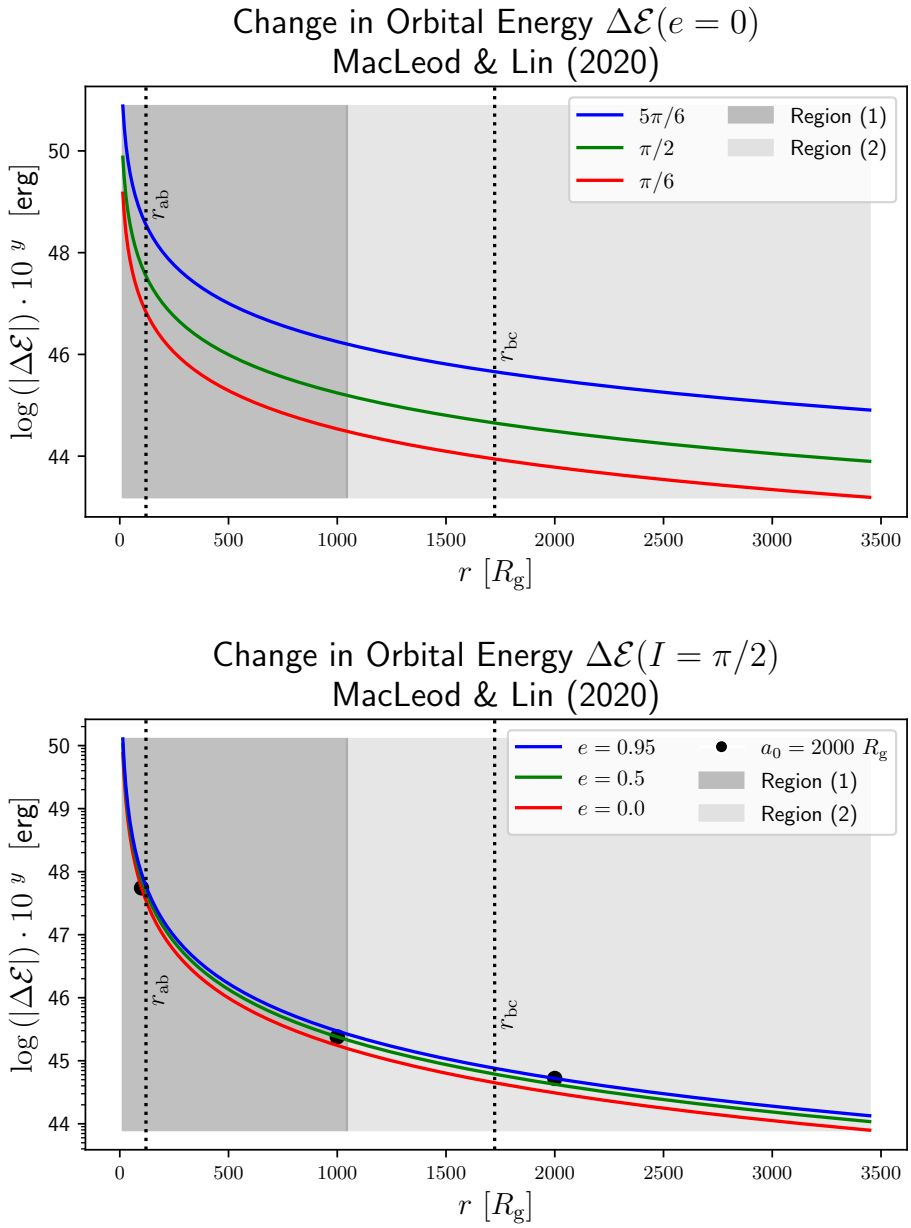

Figure 6.3: The logarithmic absolute change in orbital energy, $|\Delta\mathcal{E}|$, of a $M_\odot$ star due to impacts with the accretion disk for varying inclination angles I (first panel) and eccentricities e (second pannel) as functions of the radial impact site in terms of $R_{\rm g}$. The impactors are assumed to have an argument of periapsis $\omega = \pi$ (impact location is at the star's periapse), the SMBH mass is $M_\bullet = 10^8 M_\odot$, the anomalous viscosity parameter is $\alpha = 0.1$. For the first plot, the stars are assumed to be descending into the disk with eccentricity $e = 0$ (circular orbits). Whereas for the second plot, the stars are assumed to be descending into the disk with inclination $I = \pi/2$ (face-on or perpendicular impacts), and the black dots represent the radial position for a fixed semimajor axis of $a = 2000\ R_{\rm g}$ for the different eccentricities, which are 2000 $R_{\rm g}$ for $e = 0$, 1000 $R_{\rm g}$ for $e = 0.5$, and 100 $R_{\rm g}$ for $e = 0.95$. The dotted vertical black lines indicate the accretion disk's regional boundaries, $r_{\rm ab}$ and $r_{\rm bc}$, while the shaded areas are the SNC's regions (1) (dark gray) and (2) (light gray). The code to generate the plot was provided by the authors MacLeod & Lin (2020).

In both plots, r is given in unit $R_{\rm g}$ and $|\Delta\mathcal{E}|$ is measured in units of energy, erg, and log-scaled. Similar to $v_{\rm rel}$, the absolute change in orbital energy $|\Delta\mathcal{E}|$ is more dependent on the orbital inclination of the impactor than its orbital eccentricity. This is as expected, since the $\Delta\mathcal{E} \propto v_{\rm rel}$. While keeping the orbital eccentricity fixed at $e = 0$, stars along retrograde orbits have the greatest loss in their orbital energy, while those with prograde orbits have the smallest loss in their orbital energy. The calculation of $\Delta\mathcal{E}$ includes $2H_{\rm d}/\sin(I)$ and the drag force $F_{\rm drag}$, which are quantities that have larger values when the star follows a retrograde orbit. Due to the symmetry of the sine function between $I = 0$ and $I = \pi$, a star with a prograde orbit of $I = \pi/6$ has the same value for $2H_{\rm d}/\sin(I)$ as a retrograde orbit, but a slower $v_{\rm rel}$ (Figure 6.2) and thus experiences a weaker $F_{\rm drag}$. These subtle effects combine to produce a similar (but opposite) difference in $|\Delta\mathcal{E}|$ for the same angular deviation from $I = \pi/2$.

While keeping the orbital inclination angle fixed at $I = \pi/2$, impactors with highly eccentric orbits $e = 0.95$ experience a greater change in $|\Delta\mathcal{E}|$ than those on circular orbits $e = 0$, which is similar to what was found when investigating the effects of e on $v_{\rm rel}$. However the difference in $\Delta\mathcal{E}$ is negligible when varying the impactor's orbital eccentricity. For an impactor with a fixed semi-major axis of $a = 2000R_{\rm g}$, its radial position is $r = (2000, 1000, 100)R_{\rm g}$ for orbital eccentricities of $e = (0, 0.5, 0.95)$, respectively, which is indicated in the bottom plots of Figure 6.3 by the black dots. Since $I = \pi/2$ for each case, every value of e has the same value for $2H_{\rm d}/\sin(I)$, but they differ in $v_{\rm rel}$ (Figure 6.2) and consequently $F_{\rm drag}$. However, $\Delta\mathcal{E}$ is also dependent on the difference between the semimajor axis of the impactor before (a_i) and after (a_f) the collision, see Equation (6.10). More eccentric orbits have a grander difference between these values and thus experience a greater loss in their orbital energy.

6.4 Time-Averaged Collisional Bolometric Luminosity

If a collision at radius r deposits an average energy $\bar{E}(r)$, and all that energy is emitted as radiation, the average rate of energy deposition in dA equals the average luminosity (emitted energy per unit time) from dA:

$$dL = \frac{dE}{dt} = \bar{E}(r)\mathcal{R}_{\rm c} \tag{6.13}$$

and so using Eq.(3.15) for $\mathcal{R}_{\rm c}$, the luminosity per unit radius (erg s^{-1} cm^{-1}) is

$$\frac{dL}{dr}\ \left[\frac{\rm erg}{\rm s\cdot cm}\right] = 4\pi\bar{E}(r)n_5\ (2.4\times10^{-39}\ {\rm cm}^{-2}\ {\rm s}^{-1})\ \times \begin{cases} r_2^{9/4}r^{-5/4} \\ r_2^{1/2}r^{1/2} \end{cases} \tag{6.14}$$

where dr is taken to be 1 cm when cgs units are used. Figure 6.4 illustrates the average rate of energy deposition in dA for a sun-like star impacting the disk with an orbital inclination and eccentricity of $I = \pi/2$ and $e = 0$, respectively.

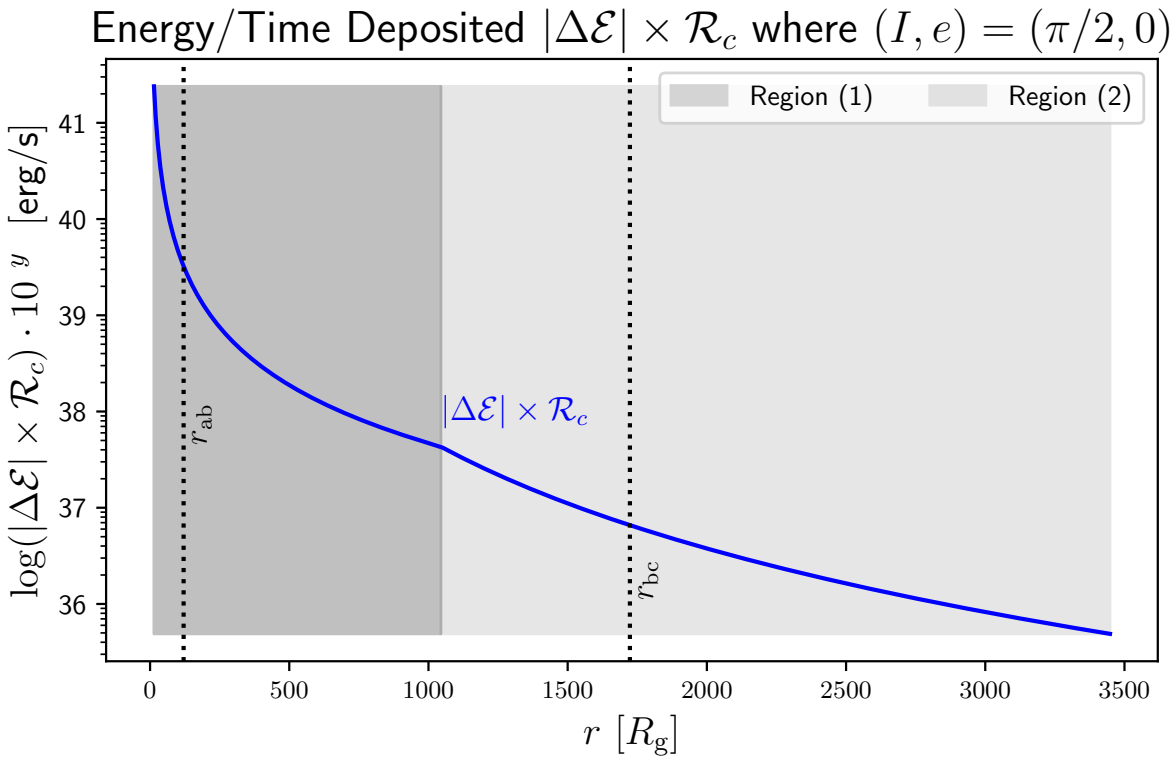

Figure 6.4: The logarithmic time averaged energy deposited into the disk as a function of radius in units of $R_{\rm g}$. The star-disk collision considered is for a single impactor with an orbital inclination and eccentricity of $I = \pi/2$ and $e = 0$, respectively. The dotted vertical black lines indicate the accretion disk's regional boundaries, $r_{\rm ab}$ and $r_{\rm bc}$, while the shaded areas are the SNC's regions (1) (dark gray) and (2) (light gray).

An impactor's change in orbital energy decreases with an increase in r (Figure 6.3), but the time-averaged collisional rate increases with r in region (1) (Figure 3.3). However, it is found that when these quantities are combined, the average energy deposition rate decreases with an increase of r.

Since the kinetic energy that is dissipated comes from gravitational motion with $v^2 \propto GM_\bullet/r$, we can say that $\bar{E} \propto r^{-1}$ (MacLeod & Lin, 2020, Eq. 30) and for convenience write $\bar{E} = E_0(r_2/r)$. The time-averaged collisional luminosity per unit radius $L_{\rm c}$ is then

$$L_{\rm c} = 4\pi E_0 n_5 \ (2.4 \times 10^{-39} \ {\rm cm}^{-2} \ {\rm s}^{-1}) \ \times \begin{cases} r_2^{13/4} r^{-9/4} \\ r_2^{3/2} r^{-1/2} \end{cases} \tag{6.15}$$

where E_0 is taken to be $|\Delta\mathcal{E}|$. Roughly speaking, over the range from 10 to 1000 $R_{\rm g}$ dL/dr drops by a factor of $10 = 100^{1/2}$; then, over the range from 1000 to 2000 $R_{\rm g}$ dL/dr drops by a factor of $2^{9/4} \simeq 5$, which is a much steeper dropoff. Figure 6.5 plots the time-averaged collisional luminosity L_c against the disk luminosity $L_{\rm d}$, given by Equation (4.19).

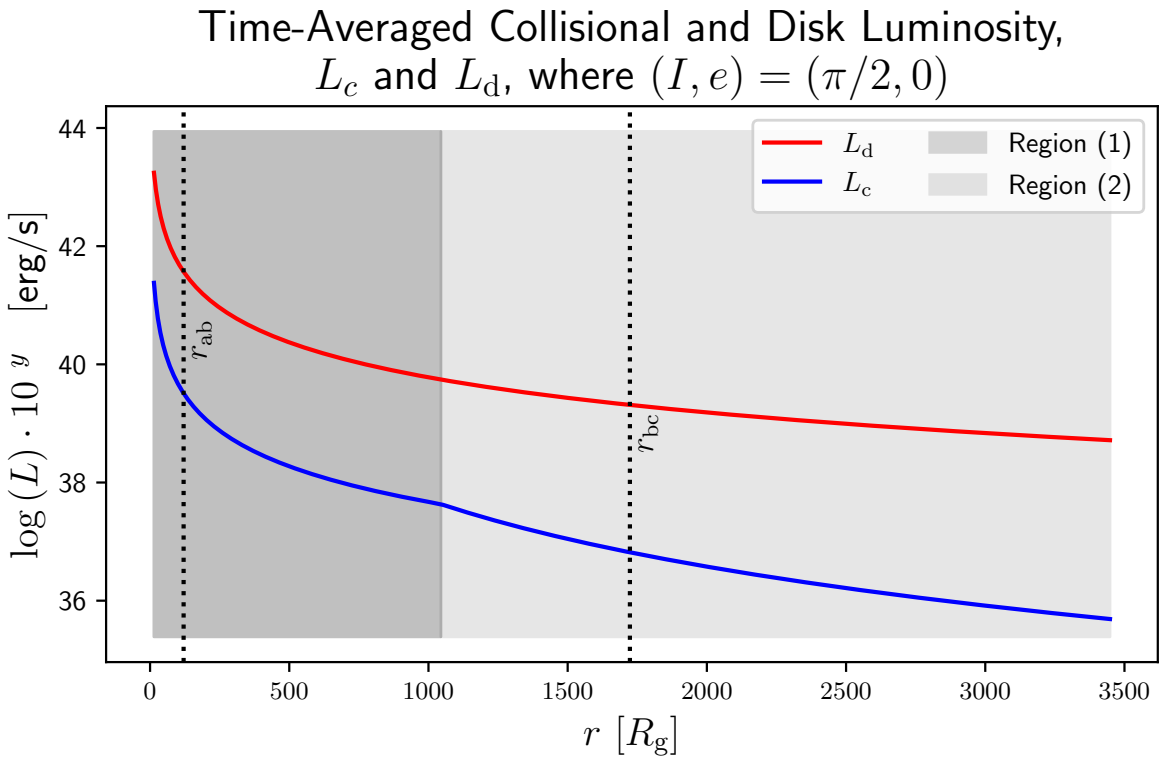

Figure 6.5: The time averaged energy deposited into the disk, $L_{\rm c}$, and the α-model disk's surface luminosity, $L_{\rm d}$ as functions of radius in units of $R_{\rm g}$. The star-disk collisions considered are for all impactors within a specified radius r with orbital inclinations and eccentricities of $I = \pi/2$ and $e = 0$, respectively. The SMBH mass is taken to be $M_\bullet = 10^8 M_\odot$, $\alpha = 0.1$, and $\dot{M}_{\rm d} = 0.1\dot{M}_{\rm Edd}$. The dotted vertical black lines indicate the accretion disk's regional boundaries, $r_{\rm ab}$ and $r_{\rm bc}$, while the shaded areas are the SNC's regions (1) (dark gray) and (2) (light gray).

For all radial impact locations r, the disk's surface luminosity is greater than the time-averaged collisional luminosity, i.e. $L_{\rm d} > L_{\rm c}$.

6.5 Summary

The relative velocity $v_{\rm rel}$ is affected more by an impactor's orbital inclination than its orbital eccentricity. The strong difference between orbital inclinations gives rise to a distinction between prograde and retrograde orbits. Impactors following retrograde orbits have xy-velocity components that are in the opposite direction to the xy-velocity components of the accretion disk, which cause them to experience a faster $v_{\rm rel}$ when compared to those following prograde orbits with xy-velocity components in the same direction as the disk. Eccentricity does affect the relative velocity, but very slightly as the difference in $v_{\rm rel}$ between an eccentricity of 0 and 0.95 is only $\sim \sqrt{2}$. Impactors with more eccentric orbits experience a faster $v_{\rm rel}$ since their largest velocity component in the z-direction is unaltered by the disk's z-velocity component, which is zero.

A change in specific orbital energy $\Delta\mathcal{E}$ is more dependent on the inclination of the orbit rather than its eccentricity. Impactors on retrograde orbits have larger values of $|\Delta\mathcal{E}|$ than those on prograde orbits, since the faster $v_{\rm rel}$ generates a stronger $F_{\rm drag}$. Whereas, impactors with more eccentric orbits experience a greater $|\Delta\mathcal{E}|$ because the calculation involves the change in their semimajor axis before and after the collision, which is more divergent than it is for impactors on circular orbits.

The time-averaged collisional luminosity $L_{\rm c}$ compared to disk luminosity $L_{\rm d}$ is insignificant, and is roughly $\sim$ 2 orders of magnitude dimmer on average when the radiation emitting region is assumed to be an annulus of width $R_{\rm g}$. When viewed in units of erg/s, dL/dr is $\sim$ 14 orders of magnitude dimmer than $L_{\rm c}$.

Overall, the eccentricity of a star's orbit has less of an effect on the relative velocity $v_{\rm rel}$ and the orbital energy loss $|\Delta\mathcal{E}|$ than its initial inclination angle relative to the disk. Varying I behaves similarly for both of these quantities and oppositely when e is varied. Finally, an impactor striking the disk with $(I, e) = (\pi/2, 0)$ at any radial impact location r within the disk cannot generate enough luminosity to outshine the luminosity of the

disk's surface.

7 Shock Tunnel

This section investigates the geometry of the region of the disk carved out by the impactor (hereafter the shock tunnel) as it completes its transit of the disk. Two sketches are made that depict the orientation of the shock tunnel in the disk's rotating frame, and the non-rotating frame of the disk. The orientation of the shock tunnel is depicted in two different frames of reference, both where the observer is looking through the plane of the disk towards the SMBH and the impactor is travelling across their line of sight. When the observer is travelling with the orbiting accretion disk it is referred to as the "rotating" frame, and when the disk is orbiting past the observer it is referred to as the "non-rotating" frame. The amount of time a impactor stays within the disk is determined for differing inclination angles, and the density of the disk is worked out in order to quantify how significant the drag-force that the disk exerts on the passing star is.

7.1 Impactor Depth as a Function of Time

The relative velocity between an impactor and the accretion disk was given in equation (6.3). The relative velocity definition is dependent on the inclination angle I, stellar velocity $v_\star$, and disk velocity v_d:

$$v_{\mathrm{rel},x} = v_\star \cos(I) - v_{\mathrm{d},x} \qquad \text{and} \qquad v_{\mathrm{rel},z} = v_\star \sin(I) - v_{\mathrm{d},z} \tag{7.1}$$

The time spent within the disk t_transit depends on disk half-thickness H_d and the stellar velocity in the $\hat{z}$-direction:

$$t_\mathrm{transit} = \frac{2H_\mathrm{d}}{v_\star \sin(I)} \tag{7.2}$$

While the impactor transits the disk it interacts with the gaseous disk material and experiences a deceleration which is assumed to be in the form of a drag force inspired by

MacLeod & Lin (2020),

$$\vec{a} = \frac{\vec{F}_{\rm drag}}{M_\star} = \frac{\pi \rho_{\rm d}}{M_\star} \left[R_\star^2 |\vec{v}_{\rm rel}|^2 + \frac{4(GM_\star)^2}{|\vec{v}_{\rm rel}|^2} \right] \left(-\frac{\vec{v}_{\rm rel}}{|\vec{v}_{\rm rel}|} \right) \tag{7.3}$$

where the factor within the parentheses is a unit vector confirming that $F_{\rm drag}$ is in the opposite direction of $\vec{v}_{\rm rel}$. Thus, for all times $0 \leq t \leq t_{\rm transit}$, in the $\hat{z}$-direction the impactor's temporal position $Z_\star(t)$ is

$$Z_\star(t) = H_{\rm d} - v_{\star,z} t + a_z t^2 \tag{7.4}$$

while in the $\hat{x}$-direction the impactor's temporal position $X_\star(t)$ is

$$X_\star(t) = H_{\rm d} - v_{\star,x} t + a_x t^2 \tag{7.5}$$

It is important to note, that even though the $\hat{z}$ component of $v_{\rm rel}$ is taken, the change is so negligible that there is no difference in transit times for retrograde or prograde orbits that have a symmetric angle with respect to the normal of the disk.

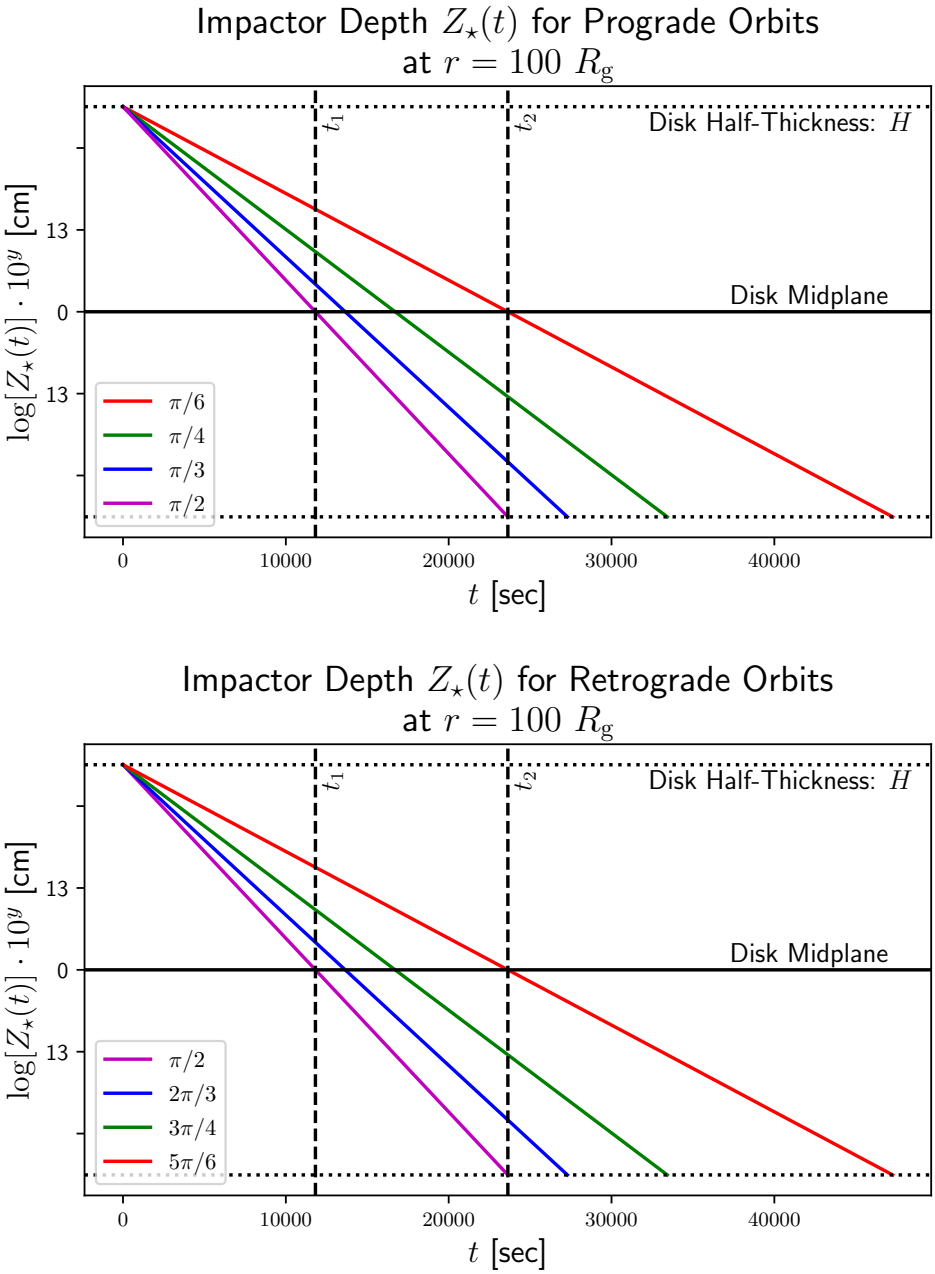

Figure 7.1: Impactor depth as a function of time $Z_\star(t)$ for prograde orbits (left) and retrograde orbits (right), with a impact velocity of $v_\star = \sqrt{GM_\bullet/r}$. The times t_1 and t_2 are the times at which the impactor with an inclination angle of $I = \pi/2$ has transited half of the disk and the entire disk, respectively. Notice that the time spent in the disk as well as the depth is symmetric with respect to the normal of the disk, i.e., $I = 5\pi/6$ and $I = \pi/6$ are the same plots.

An impactor with an inclination angle of $I = \pi/2$ has the fastest transit through the disk. The smaller the angle the impactor makes with the disk, the longer the transit time

is. Due to the symmetry of the system, inclination angles of $I = \pi/6$ and $I = 5\pi/6$, $I = \pi/4$ and $I = 3\pi/4$, and $I = \pi/3$ and $I = 5\pi/6$, yield the same transit times.

When an impactor with an inclination angle of $I = \pi/2$ is at the disk midplane, $Z_\star(t_{\rm transit}/2) = 0$, the $I = \pi/6,\ \pi/4,$ and $\pi/3$ tracks are 50%, $\sim 71\%$, and $\sim 87\%$ of the way through the "upper-half" of the disk. When this face-on impactor has completed its transit of the disk, $Z_\star(t_{\rm transit}) = -H$, the $I = \pi/6,\ \pi/4,$ and $\pi/3$ tracks are 0%, $\sim 41\%$, and $\sim 73\%$ of the way through the "lower-half" of the disk.

7.2 Sketches

When an impacting star traverses the accretion disk it temporarily carves out a cylindrical tunnel in the gaseous disk material. As time passes the tunnel is filled back in due to the hydrodynamical forces within the disk matter.

In the frame of the rotating disk (Figure 7.2) this tunnel is inclined at some angle with respect to the surface normal of the disk, due to both the relative velocity and the stellar orbital inclination angle. The rest-frame is taken as the viewpoint where the observer is moving with the gaseous disk material and looking towards the central SMBH.

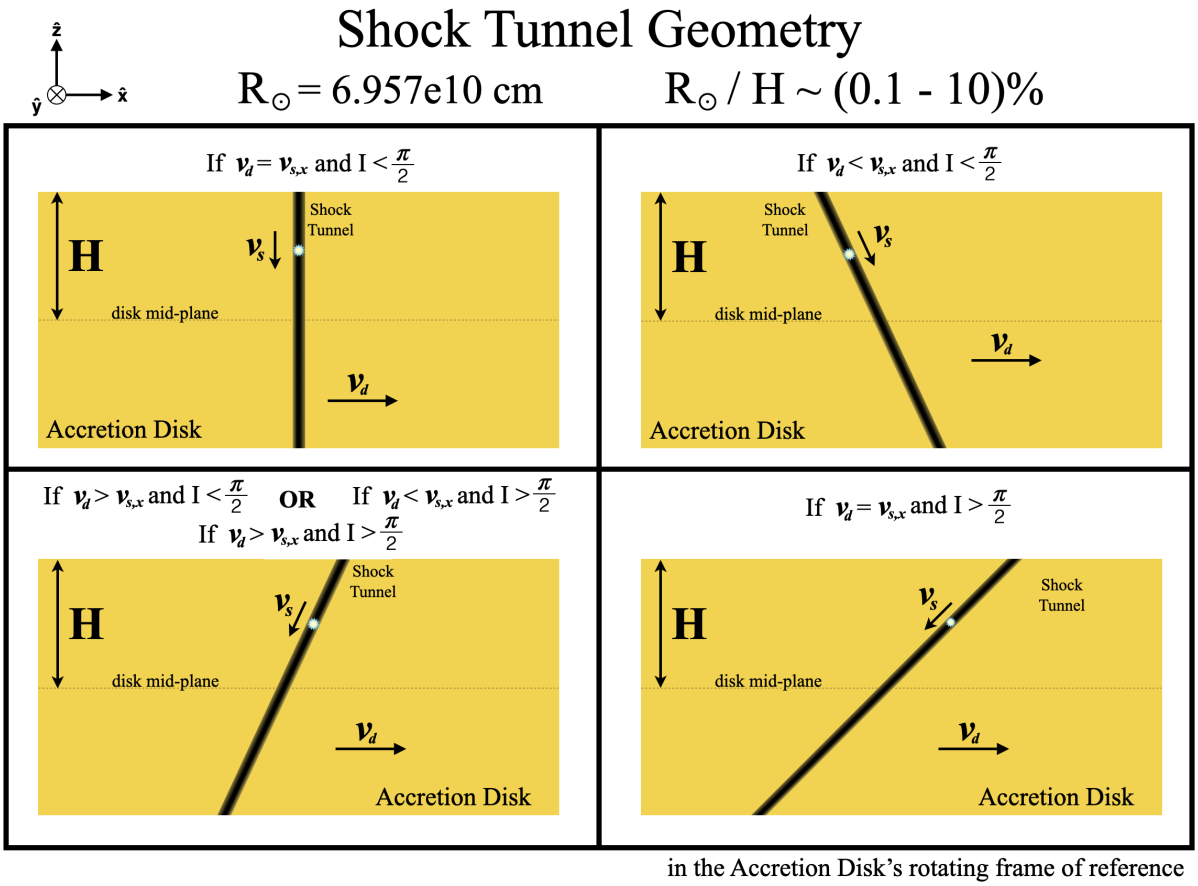

Figure 7.2: A sketch of the shock tunnel see in the rotating frame of the disk for varying relative velocities of prograde and retrograde orbits. The stellar radius $R_\star$ ($R_\odot$ in the sketch) is $\sim 10\%$ of the half-thickness of the disk $H_{\rm d}$ (H in the sketch). The y-axis is directed into the page where the mid-plane and the shock tunnel intersect, and the x-axis points to the right. It is assumed that SMBH is in the direction of the positive y-axis, and the disk's velocity is entirely in the x-direction.

The stellar velocity in the y direction is ignored and only the x and z components of its velocity are considered. The disk velocity is assumed to be entirely in the x direction, and thus only the x-component of the stellar velocity contributes to the inclination of the shock tunnel with respect to the surface normal of the disk.

Investigation of Figure 7.2 reveals that for prograde and retrograde orbits, if the x-component of the relative velocity is: (1) equal ($v_{\rm d} = v_\star$) the tunnel has no inclination (top left) or is highly inclined (bottom right), (2) positive, ($v_{\rm d} > v_\star$) the tunnel's trajectory will move away (bottom left) from the observer's inertial frame, or (3) negative ($v_{\rm d} < v_\star$) the tunnel's trajectory will move towards (top right) or away (bottom-left) from the observer's

inertial frame.

The shock tunnel takes on slightly different trajectories when viewed in the non-rotating frame of the disk (Figure 7.3). The length of the shock tunnel is at its shortest when $I = \pi/4$ since the impactor follows a prograde orbit causing it to travel more slowly through the disk. This frame of reference is taken as the viewpoint where the observer is not moving with respect to the SMBH, which is along their line of sight.

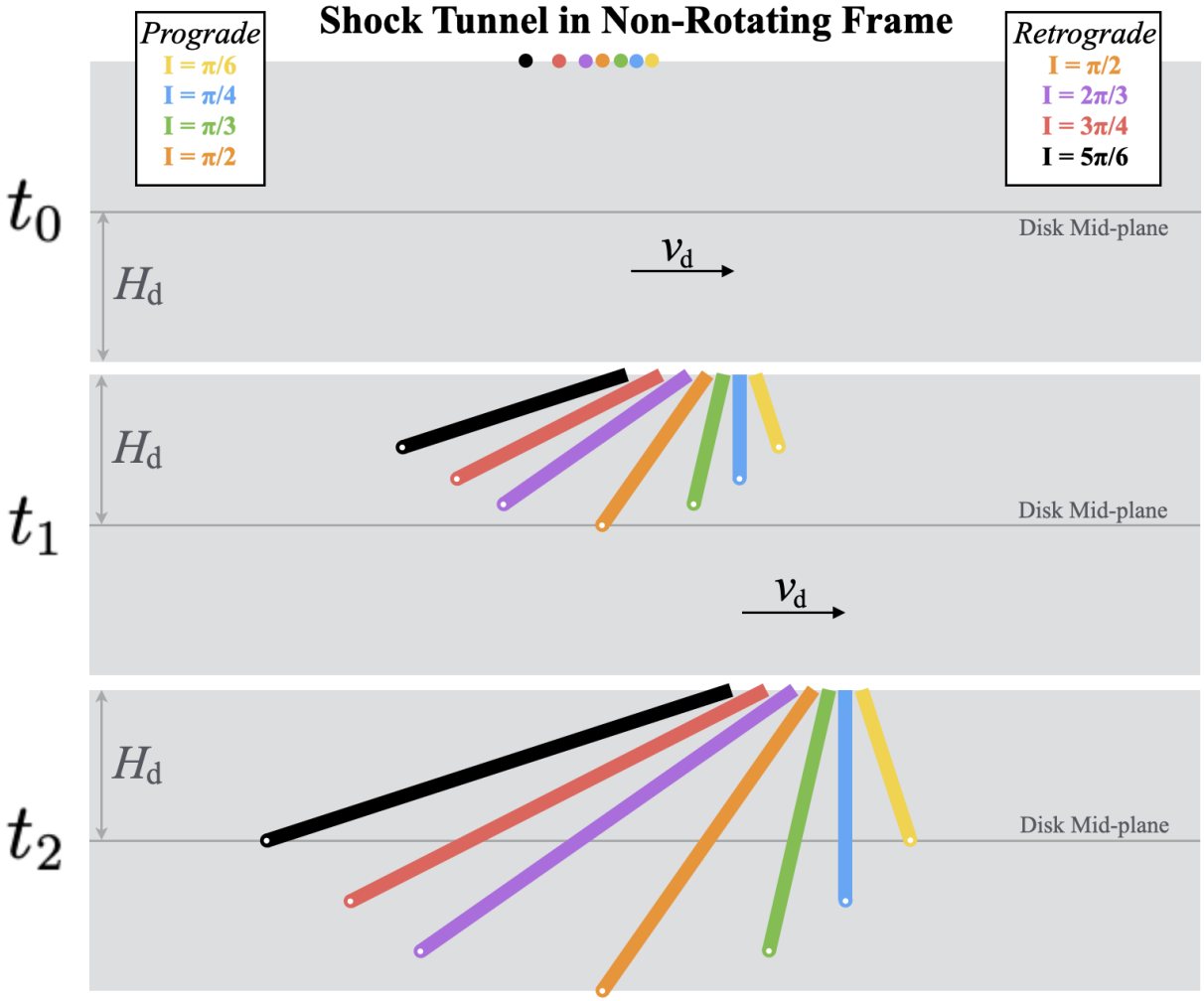

Figure 7.3: A sketch of the shock tunnel created by the impactor as seen from a non-rotating frame for varying orbital inclination angles, with respect to the disk's normal, at different times t_0, t_1, and t_2, where $t_0 < t_1 < t_2$. Time t_0 is when the impactor (with any angle) first strikes the disk, t_1 is the time at which the impactor with an inclination angle of $I = \pi/2$ has transited half of the disk, and t_2 is the time when it has transited the entire disk. The disk has velocity v_d and the magnitude of its arrow indicates how far the disk material has shifted between the respective times. The shock tunnel's size relative to the accretion disk's half-thickness is not drawn to scale, but the angle the shock tunnel makes in the disk is. The disk is rotating to the right of the figure, and the velocity of the impactor is $v_\star = \sqrt{2GM_\bullet/r}$.

7.3 Summary

As the impactor travels through the disk its position within the disk is compared for differing orbital inclination angles I. As expected, it is found that the quickest travel time occurs when $I = \pi/2$ and increases in duration the more I deviates from this value. The difference between prograde and retrograde orbits is indistinguishable, and the effect of $F_{\rm drag}$, when the geometric and gravitational effects are summed, make little difference. When an impactor striking the disk face-on has completed its transit, an impactor with a inclination angle of $I = \pi/6$ relative to the disk would be at the mid-plane of the disk.

The region of space carved out of the disk by an impactor is referred to as the shock tunnel. It is essentially a cylinder with a minimum radius of $R_\star$ that can be inclined, relative to the surfaces of the disk, depending on its $v_{\rm rel}$ and I. When looking towards the SMBH in the plane of the disk from a position greater than the impact location, modelling the geometry of the shock tunnel invokes two separate frames of reference; (1) where the observer is travelling with the rotation of the disk, and (2) where the observer remains stationary. In the first case, prograde orbits appear to create a perpendicular shock when $v_{\rm rel} = 0$ and a positively inclined tunnel (where the impactor emerges at an $+x$ position relative to its entry point) when $v_{\rm rel} > 0$. In all other cases the tunnel appears to be negatively inclined (where the impactor emerges at a $-x$ position relative to its entry point). In the second case, only impactors with $I = \pi/4$ create perpendicular tunnels. Impactors with greater I create negatively inclined tunnels, and those with smaller I create positively inclined tunnels. Impactors on highly retrograde orbits create the most negatively inclined tunnels and are therefore the longest tunnels that can be created.

8 Flare Profile

This section approximates the emission over time from both sides of the disk as the impactor plunges through it at specific radial collision sites.

As the impactor traverses the disk it deposits energy, and with the interior of the disk being optically thick, the imparted energy must travel to the photosphere of the disk in order to be observed. This requires calculations of the diffusion time of photons for the radiation dominated parts of the disk and the sound-crossing time for the gas-pressure-dominated regions of the disk.

Furthermore, the shock tunnel carved by the impactor is assumed to be a cylinder with a finite length that is constrained by the disk's thickness $2H_{\rm d}$. As the volume of the tunnel increases, the temperature of the shocked gas will decrease to a point at which it is comparable to the disk's temperature $T_{\rm d}$ at $\sim 1.01T_{\rm d}$. The amount of time required for this to occur is estimated as the thermal timescale $t_{1\%}$.

The unperturbed gas beside the tunnel is pushed out of the way by the recently shocked gas and its outward velocity is slowed as it sweeps up more unperturbed gas along its path. Thus, the shock tunnel can attain a maximum radius $R_{\rm stall}$ that is worked out to be slightly larger than the solar radius. At this time the shocked gas, which is still hot, surrounding the tunnel is comparable to the disk temperature and no longer distinguishable. However, the photons in the shocked gas region diffuse outwards.

8.1 Timescales

Various timescales are considered when determining the emission from the surfaces of the disk as the impactor impacts, transits, and ultimately emerges. The radial impact locations $r = (100, 500, 2000)\ R_{\rm g}$ will be used throughout this section and the general form will be used for calculated quantities for consistency. An example of this computes

the stellar velocities of circular Keplerian orbits around the fiducial SMBH mass,

$$v_\star = \sqrt{\frac{GM_\bullet}{r}} \sim (21.2, 9.48, 4.74) \times 10^3 \ \frac{\text{km}}{\text{s}} \tag{8.1}$$

Thus $v_\star(r = 100R_\text{g}) \sim 21,200$ km/s.

8.1.1 Transit Time

An impactor's transit time (Eq. 7.2) across a disk of thickness $2H_\text{d}$ can be worked out given its orbital velocity $v_\star$, For the fiducial disk and impactor parameters, along with the impact locations, the stellar escape velocities ($v_\infty = \sqrt{2}v_\star$) are worked out to be:

$$v_\infty = (30, 13, 6.7) \times 10^3 \ \frac{\text{km}}{\text{s}} \sim (0.1, 0.04, 0.02)c \tag{8.2}$$

The distance travelled by these impactors is twice the half-thickness of the disk which is provided by SS73 in Equation (4.9). Half of the distance travelled by the impactor is calculated to be

$$H_\text{d} = (2.47, 3.20, 12.9) \times 10^{13} \text{ cm} \tag{8.3}$$

As expected the thickness of the disk increases with r. The impactor that collides furthest from the SMBH ($2000R_\text{g}$) must go through nearly 5 times as much disk matter as the impactor colliding at $100R_\text{g}$.

Evaluation of the transit time for the fiducial disk parameters and radial impact positions yields,

$$t_\text{transit} = (1.65, 4.77, 38.4) \times 10^4 \text{ s} \sim (4.58, 13.3, 107) \text{ hrs} \sim (0.19, 0.55, 4.44) \text{ days} \tag{8.4}$$

Here the values for t_transit are under the assumption that the impactor is striking the disk face-on ($I = 90°$) with a velocity of v_∞ If the stars are instead striking the disk at

the same locations with bound circular orbital velocities of $v_\star = \sqrt{GM_\bullet/r}$ and all other parameters remain the same the transit time becomes $\sim (0.27, 0.78, 6.3)$ days.

8.1.2 Photon Diffusion Time

Following del Valle & Pohl (2018), the diffusion timescale of photons $t_{\rm diff}$ within a shocked region is dependent on the initial radius of the bow shock R_0 created by the impacting star and the diffusion coefficient D of the interacting medium

$$t_{\rm diff} \sim \frac{R_0^2}{D} \tag{8.5}$$

Derishev (2018) considers radiation-mediated shocks for arbitrary shock velocities and provides a formula for the diffusion coefficient

$$D = \frac{\lambda c}{3} \tag{8.6}$$

where λ is dependent on the physical properties of the interacting medium. For our case, where we assume that the photons interact with the disk's plasma mostly via Thompson scattering, $\lambda = 1/(\sigma_{\rm Tot} n_e)$ where n_e is the total number density of electrons and positrons.

Combining equations (8.5) and (8.6) yields a final relation for the diffusion timescale

$$t_{\rm diff} \sim \frac{R_0^2}{D} = \frac{3R_0^2}{\lambda c} = \frac{3R_0^2 \sigma_{\rm Tot} n_e}{c} \tag{8.7}$$

We assume that the shock boundary lies where the large headwind pressure of the gaseous disk material balances with the stellar atmospheric pressure giving $R_0 \sim R_\star$ (McKernan et al., 2021).

For the total cross section, we use the Thomson cross section $\sigma_{\rm T}$ multiplied by 1 plus the ratio of the frequency-averaged, emission-weighted absorption opacity $\kappa_{\nu,{\rm abs}}$ and the

electron scattering opacity $\kappa_{\rm es}$ (Hall et al., 2018, Eq. 1). In their notation,

$$\sigma_{\rm Tot} = \frac{\sum_\nu F_\nu \left(1 + \frac{\kappa_{\nu,{\rm abs}}(r)}{\kappa_{\rm es}}\right)}{\sum_\nu F_\nu} \sigma_{\rm T} \equiv \left(1 + \frac{\kappa_{\rm abs}(r)}{\kappa_{\rm es}}\right) \sigma_{\rm T} \ . \tag{8.8}$$

For F_ν we use the geometric mean of the blackbody emission functions B_ν for the central disk temperature $T_{\rm cen}(r)$ and the surface temperature $T_{\rm surf}(r)$:

$$F_\nu = \sqrt{B_\nu(T_{\rm cen}(r)) B_\nu(T_{\rm surf}(r))} \ . \tag{8.9}$$

The multiplicative factor in equation (8.8) asymptotes to 1 when electron scattering dominates and becomes increasingly proportional to the absorption opacity when absorption dominates. For a SMBH mass of $M_\bullet = 10^8\ M_\odot$ with $\alpha = 0.1$ accreting at 10% of the Eddington limit at radii $r = (100, 500, 2000)\ R_{\rm g}$ this factor is evaluated to be 1.57, 419, and 109 000, respectively.

The correction factors are very different for the fiducial radii, reflecting the fact that electron scattering is important in the disk at small radii but not at large radii. So the cross-section is >1,000 times higher than the Thomson cross section at large radii. (For diffusion in a fully ionized plasma, Thomson scattering is a reasonable assumption, but not for diffusion in a disk where many atoms will still have electrons bound to them which will be able to absorb and re-emit photons.)

Equation (4.17) provides n_e, which for the fiducial parameters and impact radii is worked out to be:

$$n_e = (12.1, 44.0, 5.28) \times 10^{14}\ {\rm cm}^{-3}$$

Evaluation of the diffusion timescales for the fiducial disk parameters and radial positions of $r = (100, 500, 2000)\ R_{\rm g}$ yields,

$$t_{\rm diff} \sim (0.17, 165, 5151)\ {\rm hrs} \sim (0.007, 6.87, 215)\ {\rm days}$$

8.1.3 Sound Crossing Time

Following Netzer (2013), the time required for a sound wave to travel through the accretion disk out to a distance r from the SMBH is dependent on the SMBH mass $M_\bullet$, the temperature of the disk $T_\mathrm{d} = T_\mathrm{cen}$, and the radial distance from the SMBH r:

$$t_{s,r} = 0.3 \left(\frac{M_\bullet}{10^8\ M_\odot}\right) \left(\frac{r}{R_\mathrm{g}}\right) \left(\frac{T_\mathrm{d}}{10^4\ \mathrm{K}}\right)^{-1/2} \ \mathrm{yrs} \tag{8.10}$$

For the fiducial parameters and radii used in this report the T_d is calculated to be:

$$T_\mathrm{d} \sim (14.1, 4.76, 1.29) \times 10^4\ \mathrm{K} \tag{8.11}$$

Inputting these values into Eq.(8.10), the sound-crossing times for our fiducial parameters and radii are calculated to be

$$t_{s,r} \sim (15.4, 68.7, 528)\ \mathrm{yrs} \tag{8.12}$$

It is important to realize that these timescales are for a distance r from the SMBH, hence why the amount of time elapsed is so long. The vertical sound crossing time (the amount of time required to travel a distance of H_d) for the same fiducial parameters is worked out to be

$$\begin{aligned} t_{s,H_\mathrm{d}} &= 0.3 \left(\frac{M_\bullet}{10^8\ M_\odot}\right) \left(\frac{r}{R_\mathrm{g}}\right) \left(\frac{H_\mathrm{d}}{r}\right) \left(\frac{T_\mathrm{d}}{10^4\ \mathrm{K}}\right)^{-1/2} \ \mathrm{yrs} \\ &\sim (0.067, 0.149, 1.150)\ \mathrm{yrs} \sim (24.4, 54.4, 420)\ \mathrm{days} \end{aligned} \tag{8.13}$$

The half shock tunnel sound-crossing time (the amount of time required for a sound

wave to travel a distance of R_0) for the same fiducial parameters is worked out to be

$$\begin{aligned} t_{s,R_0} &= 0.3 \left(\frac{M_\bullet}{10^8\ M_\odot}\right)\left(\frac{r}{R_{\rm g}}\right)\left(\frac{R_0}{r}\right)\left(\frac{T_{\rm d}}{10^4\ {\rm K}}\right)^{-1/2}\ {\rm yrs} \\ &\sim (1.65, 2.84, 5.44)\ {\rm hrs} \end{aligned} \tag{8.14}$$

Thus $t_{\rm diff} < t_{s,R_0}$ at small radii and $t_{\rm diff} > t_{s,R_0}$ at large radii.

8.1.4 Thermal Timescale

A volume of gas shock-heated to $T_{\rm g} = T_{\rm sh}$ per unit time is that of a cylinder expanding in length at a rate of the stellar velocity $v_\star$

$$\pi R_0^2 v_\star \tag{8.15}$$

The volume occupied by that gas at a later time is approximately an expanding cylinder with a leading hemispherical end cap:

$$\left[\pi R_0^2 v_\star t + \frac{2}{3}\pi R_0^3\right]\left(\frac{t}{t_{\rm diff}}\right)^{3/2} \tag{8.16}$$

The temperature difference $\Delta T_{\rm gs} = T_{\rm g} - T_{\rm sh}$ will decrease with the ratio of the volumes. If $\Delta T_{\rm gs} < 0.01 T_{\rm d}$, energy output will be within $\sim 4\%$ of the normal disk output and will probably be undetectable. Energy put into gas in time dt is:

$$\left(\pi R_0^2 v_\star\right)\left(\frac{3}{2}\frac{\rho_{\rm d} k_B T_{\rm sh}}{m_p}\right)\ dt \rightarrow \left(\pi R_0^2 v_\star\right)\left(\frac{3}{2} n_{\rm H} k_B T_{\rm sh}\right) \tag{8.17}$$

where $n_{\rm H} = \rho_{\rm d}/m_p$ is the number density of hydrogen atoms assuming that the disk is void of any metallicity [5].

The characteristic temperature was defined earlier in equation (6.2), and it is assumed to be that of the shocked gas temperature $T_{\rm sh} = T_{\rm char}$. If impactors with the fiducial parameters are striking the disk at the fiducial radii the characteristic temperature is worked out to be:

$$T_{\rm char} \sim (181, 36.3, 9.07) \times 10^8 \text{ K} \tag{8.19}$$

For stars on circular orbits ($e = 0$) striking the disk at and inclination angle of $I = \pi/4$ at radii $r = (100, 500, 2000)\ R_{\rm g}$, the characteristic temperature is

$$T_{\rm char} \sim (90.7, 18.1, 4.53) \times 10^8 \text{ K} \tag{8.20}$$

which is roughly half the values obtained when the star is plunging into the disk at the escape velocity.

The temperature of the gas as a function of time is assumed to be:

$$T_{\rm g}(t) = T_{\rm d} + \Delta T_{\rm g}(t) = (T_{\rm d} + T_{\rm sh})\,\frac{V_0}{V(t)} \tag{8.21}$$

where V_0 is the initial volume of the shocked gas, and $V(t)$ is the volume of the gas at some time t later.

It is useful to define the thermal timescale as the amount of time that must elapse in order for $\Delta T_{\rm g}(t) < 0.01 T_{\rm d}$, or equivalently $T_{\rm g}(t) < 1.01 T_{\rm d}$. Rearranging this relation yields an expression to characterize the amount of time required to reach this inequality,

[5] The volumetric mass densities $\rho_{\rm d}$ for each disk region are defined in Eq. 4.16, following the α-disk model of SS73. For the fiducial parameters and radii the disk densities are calculated to be:

$$\rho_{\rm d} \sim (20.2, 74.2, 8.80) \times 10^{-10}\ \frac{\rm g}{\rm cm^3} \tag{8.18}$$

which we define as the thermal timescale:

$$t_{1\%} = \frac{T_{\rm g}(t)}{T_{\rm d}} = \frac{T_{\rm d} + T_{\rm sh}}{T_{\rm d}} \frac{V_0}{V(t)} < 1.01 \tag{8.22}$$

where the temperature factor is fixed for a given impactor striking the disk at a given r and $V(t)$ will grow with time t.

It is assumed that the initial volume is that of the shock tunnel carved out of the disk after an impactor has completed a full transit through the disk, i.e. $V_0 = 2\pi H_{\rm d} R_0^2$, and that the volume later at some time t behaves as

$$V(t) = 2\pi H_{\rm d} R(t)^2 = 2\pi H_{\rm d} R_0^2 \frac{t}{t_{\rm diff}} \qquad \text{where} \quad R(t) = R_0 \sqrt{\frac{t}{t_{\rm diff}}} \tag{8.23}$$

as long as the shock tunnel is formed at a radii where $t_{\rm diff}$ is the shortest timescale. For the fiducial parameters $t_{\rm diff} \sim 10$ minutes is the shortest timescale that the deposited energy escapes in at the fiducial radius of 100 $R_{\rm g}$, and the amount of diffusion timesecales needed for $t_{1\%} < 1.01$ is $\sim 127483 t_{\rm diff} \sim 2.47$ years. Which implies that the region of shocked gas takes an incredibly long time until its energy output is within 4% of the normal disk output. As the photons diffuse through the disk material they will interact with neighbouring atoms that will effectively lower their energy, thereby cooling the disk as they reach the surface of the disk. Both of these effects were ignored during the analysis, but when considered should make $t_1\%$ an upper limit.

At the larger radii the photons are assumed to travel with the shock at the sound speed, since $t_{s,R_0} < t_{\rm diff}$. The volume at some time later t when the shock tunnel expands at the sound speed v_s in 2-dimensions is

$$V(t) = 2\pi H_{\rm d} R(t)^2 \qquad \text{where} \quad R(t) = R_0 + v_s t \tag{8.24}$$

The sound speed in an ideal monatomic gas comprised of hydrogen is

$$v_s = \sqrt{\frac{\gamma R T(r)}{M_H}} \tag{8.25}$$

where $\gamma = 5/3$ is the adiabatic constant of a monatomic gas, $R = 8.314 \times 10^7$ erg mol^{-1} K^{-1} is the universal gas constant, $T(r)$ is the radially dependent absolute temperature of the disk gas, and $M_H = 1.00794$ g mol^{-1} is the molecular weight of hydrogen. Thus the sound speed for our fiducial parameters and at radii $r = (100, 500, 2000)\ R_{\rm g}$ is calculated to be:

$$v_s = (4.40, 2.56, 1.33) \times 10^6\ \frac{\rm cm}{\rm s}\ . \tag{8.26}$$

For the fiducial parameters the half-shock sound crossing timescale t_{s,R_0} is shorter for the fiducial radii $r = (500, 2000)\ R_{\rm g}$ and the amount of half-shock sound crossing timesecales needed for $t_{1\%} < 1.01$ at these radial distances is $\sim (729, 700)\, t_{s,R_0} \sim (86.1, 159)$ days, respectively. The thermal timescale in the cases where the shocked gas expands at the speed of sound is far shorter than when the shocked gas expands at the photon diffusion velocity, implying that the energy output decreases to within 4% of the normal accretion disk output much faster. This result is most likely more accurate, since there are less physical phenomena in the transfer of the energy that are being ignored.

8.2 Maximum Shock Tunnel Radius

As the impactor shocks the gas while it travels through the disk, the newly shocked gas will exert a pressure on the un-shocked gas and push it out of the way. This pushed gas will have a transverse velocity on the order of $R_0/v_\star$ that will slow down as it sweeps up other gas. This will lead to a maximum cylindrical radius of the shocked gas

$$R_{\rm stall} = R_0 \sqrt{\mathcal{M}} \quad \text{where} \quad \mathcal{M} = \frac{v_\star}{v_s} \tag{8.27}$$

is the Mach number of the shock, defined as the ratio of the impactor's velocity $v_\star$ and the sound speed of the gas v_s.

An equation for this radius is derived by assuming the conservation of momentum and solving for $R_{\rm stall}$:

$$\begin{aligned} \mathrm{p}_i &= \mathrm{p}_f \\ \rho\pi R_0^2 v_\star &= \rho\pi R_{\rm stall}^2 v_s \\ R_0^2 v_\star &= R_{\rm stall}^2 v_s \\ R_{\rm stall} &= R_0\sqrt{\frac{v_\star}{v_s}} \end{aligned} \tag{8.28}$$

Using the fiducial values and radial impact locations, $R_{\rm stall}$ is calculated to be:

$$R_{\rm stall} \sim (11.5, 10.1, 9.86) \times 10^{11}\ \mathrm{cm} \tag{8.29}$$

which is $\sim 14.2 - 16.5$ times larger than the solar radius $R_\odot$.

When an impactor strikes the disk at the same sites with a bound orbital velocity of $v_\star = \sqrt{GM_\bullet/r}$, and all other fiducial values remain the same, the size of $R_{\rm stall}$ becomes

$$R_{\rm stall} \sim (9.7, 8.5, 8.3) \times 10^{11}\ \mathrm{cm} \tag{8.30}$$

which are $\sim 13.9 - 11.9$ times larger than $R_\odot$.

8.3 Emission Profile

Consider a star that is travelling vertically through a disk at a speed of $v_\star$ from time $t = 0$ to time $t = 2H_{\rm d}/v_\star$. The luminosity of the shock is L_w between these times and zero before and after. We define the 'front' side of the accretion disk as the side that the star first strikes and the 'back' side as the side where it emerges from. Its position along the

z-axis is $z(t) = H_{\rm d} - v_\star t$ and its depth relative to the front side is $d_f(t) = v_\star t$, while its depth relative to the back side is $d_b(t) = 2H_{\rm d} - v_\star t$. For brevity, the placeholder d_x will be used in place of d_f and d_b, where $x = (f, b)$.

The amount of luminosity emitted by the star at depth z that emerges between the surface radii r_1 and r_2 on the front (or back) side of the disk between times t_1 and t_2 can be worked out. It is important to note that this approach ignores the gradual change of the photon's wavelength as the shock energy diffuses into a larger volume of gas and the emitting gas cools.

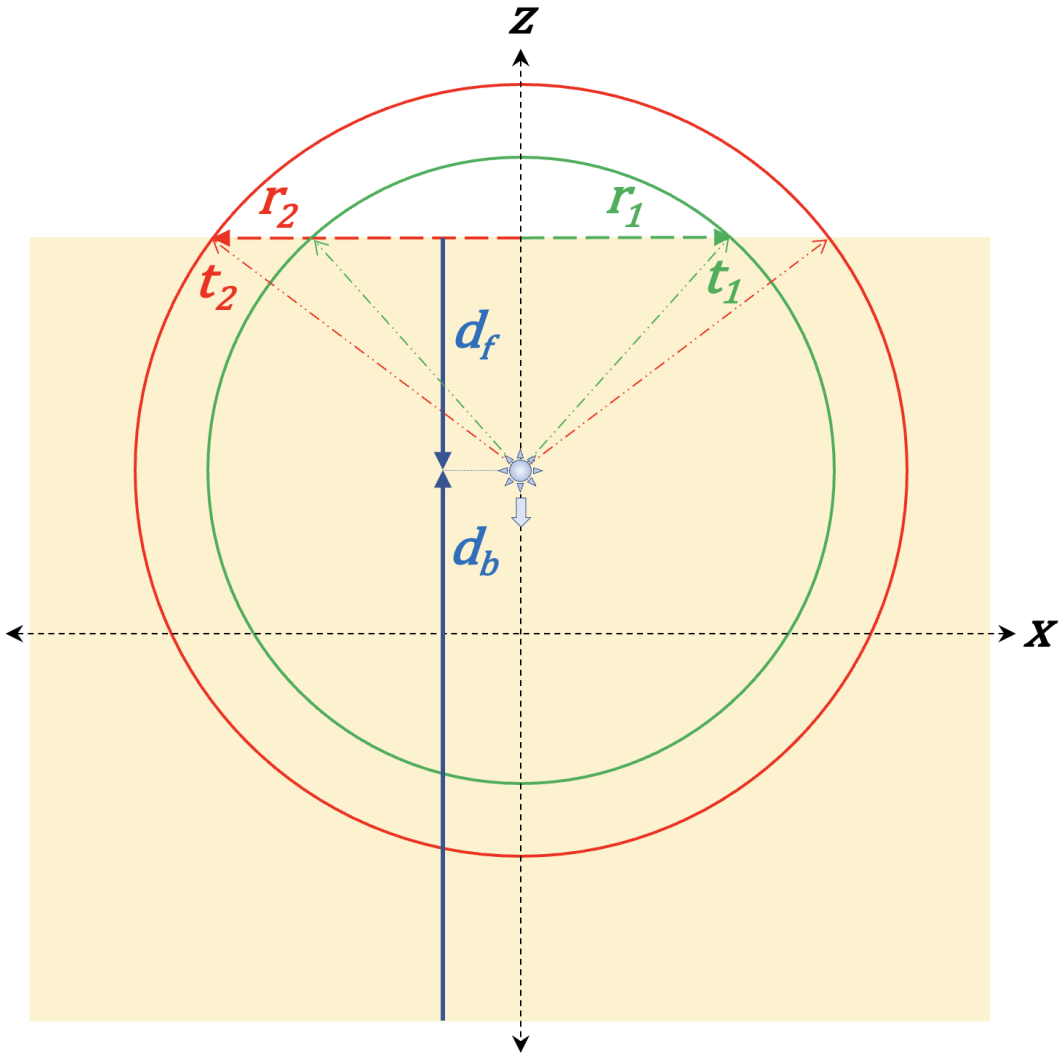

Figure 8.1: Sketch of the diffusion of photons from a point source. The stellar impactor is travelling in the $-z$-direction and at any given point in time is at depth z with its distance from the front and back side of the disk being d_f and d_b, respectively. The shocked photons released at time t_1 and later time t_2 make their way to the disk's surface where they emerge between the surface radii r_1 and r_2.

To calculate this we assume that at every dt in time, an energy of $L_w dt$ is emitted from the shock and diffuses outwards in a spherical shell. After some time interval t_{later} the energy has travelled a distance of

$$R\left(t_{\text{later}}\right) = \begin{cases} R_0 \sqrt{\frac{t_{\text{later}}}{t_{\text{diff}}}} & \text{if } t_{\text{diff}} < t_{s,R_0} \\ R_0 + v_s t_{\text{later}} & \text{if } t_{\text{diff}} > t_{s,R_0} \end{cases} \tag{8.31}$$

from its origin. Approximating the average surface radius as $\langle r \rangle = (r_1 + r_2)/2$, an energy per unit area of

$$\frac{L_w dt d\Omega}{4\pi(\langle r \rangle^2 + d_x^2)} \tag{8.32}$$

is emitted between r_1 and r_2 from the impact site on the front side of the disk between times

$$t_i = \begin{cases} t(d_x) + \frac{t_{\rm diff}}{R_0^2}\left(d_x^2 + r_i^2\right) & \text{if } t_{\rm diff} < t_{s,R_0} \\ t(d_x) + \frac{t_{s,R_0}}{R_0}\sqrt{d_x^2 + r_i^2} & \text{if } t_{\rm diff} > t_{s,R_0} \end{cases} \tag{8.33}$$

where $i = (1, 2)$ is the placeholder for times t_1 and t_2, and

$$t(d_x) = \begin{cases} \frac{d_f}{v_\star} & \text{when } x = f \\ \frac{2H_{\rm d} - d_b}{v_\star} & \text{when } x = b \end{cases} \tag{8.34}$$

is the time required for the impactor to reach depths d_f and d_b, and

$$d\Omega = \int_{r_1}^{r_2} \frac{2\pi r d_x}{(r^2 + d_x^2)^{3/2}}\, dr = \left.\frac{-2\pi d_x}{\sqrt{r^2 + d_x^2}}\right|_{r_1}^{r_2} = -2\pi\left(\frac{1}{\sqrt{1 + (r_2/d_x)^2}} - \frac{1}{\sqrt{1 + (r_1/d_x)^2}}\right) \tag{8.35}$$

which comes from rewriting $d\Omega = 2\pi \int \sin\theta_x \, d\theta_x$, where $\theta_x = 0$ is the direction from the star towards the surface of the disk, so that $\sin\theta_x = r/\sqrt{d_x^2 + r^2}$ for $d_x > 0$

The flare profile can be determined by summing the luminosities from all depths $d_x > 0$. A time interval dt is chosen such that $t_1 = 0$, $t_2 = dt$; then $t_1 = dt$, $t_2 = 2dt$; etc. The energy escaping between times t_1 and t_2 are calculated by determination of the radii

$$r_i\left[\text{cm}^2\right] = \begin{cases} \sqrt{\frac{R_0^2}{t_{\rm diff}}\left[t_i - t(d_x)\right] - d_x^2} & \text{for } \; t_{\rm diff} < t_{s,R_0} \\ \sqrt{\left[\frac{R_0}{t_{s,R_0}}\left(t_i - t(d_x)\right)\right]^2 - d_x^2} & \text{for } \; t_{\rm diff} > t_{s,R_0} \end{cases} \tag{8.36}$$

where $i = (1, 2)$ is the placeholder for r_1 and r_2, similar to the placeholder for

The emission from each depth at timestep dt is calculated and summed together to provide a value of the emission as a function of time using the formula:

$$E(dt) = \sum_{d_x} \frac{L_w dt d\Omega [r_2(d_x)^2 - r_1(d_x)^2]}{4\pi(\langle r(d_x)\rangle^2 + d_x^2)} \ . \tag{8.37}$$

8.3.1 Code Steps

We developed a python script to determine the flare profile, and a brief explanation of its operation follows. The code takes an array of different radial impact locations and returns various plots of the emission profile and a csv text file for further manipulation. Before it determines the flare profiles it must first calculate various parameters involved in the collision. These include the density $\rho_{\rm d}$, surface temperature $T_{\rm d}$, electron number density n_e, and half-thickness $H_{\rm d}$ of the disk. The shock radius R_0, the diffusion time $t_{\rm diff}$, the sound crossing time out to the radial impact location $t_{s,r}$, the vertical sound crossing time $t_{s,H_{\rm d}}$, the shock radius sound crossing time t_{s,R_0}, and the transit time $t_{\rm transit}$.

The timestep dt is chosen such that

$$dt = \begin{cases} \frac{t_{\rm diff}}{N} & \text{if} \quad t_{\rm diff} < t_{s,R_0} \\ \frac{t_{s,R_0}}{N} & \text{if} \quad t_{\rm diff} > t_{s,R_0} \end{cases} \tag{8.38}$$

where N is a chosen number controlling the amount of time elapsed in each time interval. The larger N is the smaller the timestep is and the better the approximation of the profile becomes. A for loop runs through these timesteps using a chosen index variable t, such that when $t = 0$ the impactor is assumed to be just striking the disk and when $t = t_{\rm transit}$ the impactor is assumed to be emerging from the disk. The amount that it runs through to is determined by

$$N_{dt} = \frac{2H_{\rm d}}{dt\ v_\star} \ . \tag{8.39}$$

For each timestep dt, times t_1 and t_2 are chosen such that

$$t_1 = dt \times t \quad \text{and} \quad t_2 = dt \times (t+1) \tag{8.40}$$

A second (nested) for loop then runs through all the possible depths within the disk that the impactor can be at for a given timestep dt relative to the front d_f and back d_b side of the disk. This loop begins with $d_f = 0$ ($d_b = 2H_\mathrm{d}$) and ultimately ends with $d_f = 2H_\mathrm{d}$ ($d_b = 0$). The possible depths that the emission originates from depends on the timestep, such that when the impactor first enters the disk the emission can only originate from $d_f = 0$ and at some time $dt \times t$ later the emission can originate from $d_f = 0$ to $d_f = v_\star(dt \times t)$. Once the impactor has completed its transit of the disk the emission can originate from all depths, $d_f = 0$ to $d_f = 2H_\mathrm{d}$, for all times.

The emission from each depth at timestep dt is calculated and summed together to provide a value of the emission as a function of time using Equation (8.37) divided by dt to convert to a luminosity before plotting.

8.3.2 Results

Figure 8.2 serves as an approximation to the flare profile over time. When the star first strikes the disk radiation is emitted from the front-side of the disk, but due to the mathematical approximation at this point in time $t = 0$ and therefore $d_f = 0$ which in turn makes $d\Omega = 0$, thus causing the luminosity of the flare to be calculated as zero. This is obviously not true, and as the length of the timestep dt is decreased the approximation improves. Because of this discrepancy, the profile exhibits a sharp increases in luminosity every time the emission from a previous depth reaches either of the disk's surfaces, similar to a decreasing sawtooth wave, which is most notable in the profile of the impact furthest from the SMBH at $r = 2000\ R_\mathrm{g}$. The other two radial impact locations of $r = 100\ R_\mathrm{g}$ and $r = 500\ R_\mathrm{g}$ also have this feature, however the larger amount of timesteps involved

in their calculation cause the profiles to appear smoother.

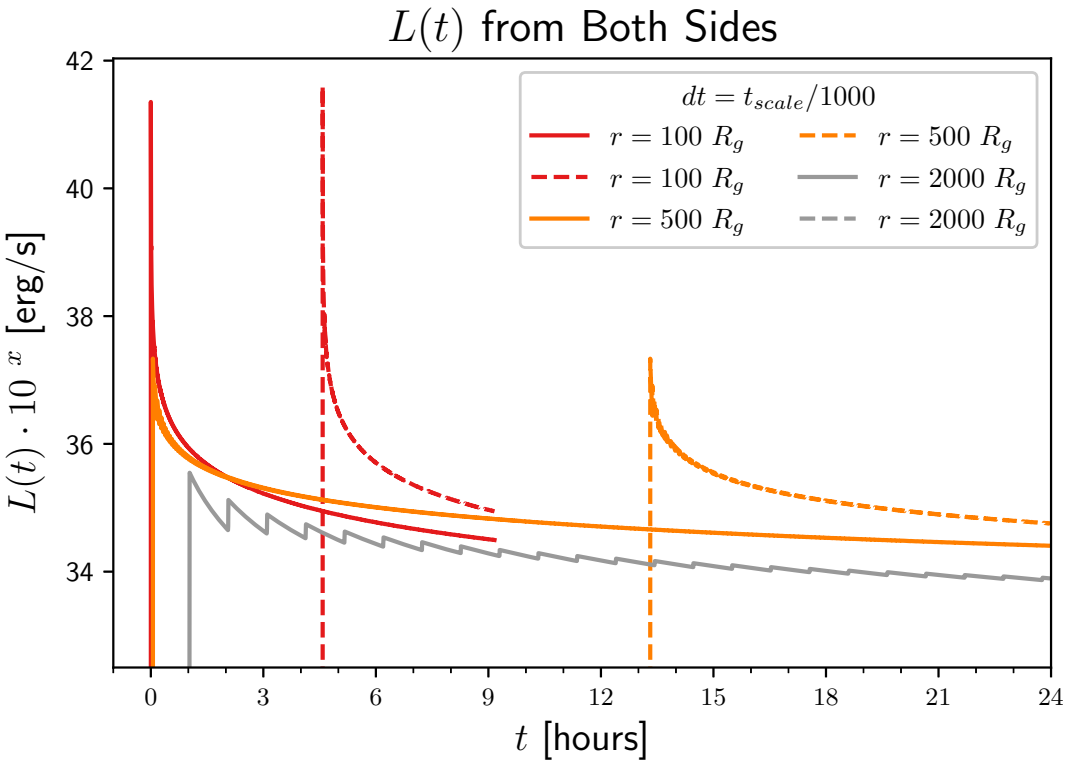

Figure 8.2: Logarithmic plot of the energy output of the flare on the front side (solid lines) and back side (dashed lines) of the accretion disk as a function of time for the fiducial accretion disk values of SMBH mass $M_\bullet = 10^8\ M_\odot$, mass accretion rate $\dot{M} = 0.1\ \dot{M}_{\rm Edd}$, viscosity parameter $\alpha = 0.1$. The impactor is assumed to be impacting the disk with a velocity of $v_\star = \sqrt{2GM_\bullet/r}$, such that it makes a vertical transit through the disk. The value of the timestep is dependent on the radial position of the impact site such that $dt = t_{\rm diff}/10^3$ when $r = 100\ R_{\rm g}$ and $dt = t_{s,R_0}/10^5$ when $r = (500, 2000)\ R_{\rm g}$. The amount of time elapsed is twice the disk crossing time $2t_{\rm transit} = 2H_{\rm d}/v_\star$. The emission from the back side of the disk for the most extreme radial impact of $r = 2000\ R_{\rm g}$ occurs after ~ 4.5 days and is not depicted. There is a very quick rise time to the peak emission involving a few timesteps, however this is not easily seen and one must examine the profile on incredibly short timescales to observe it.

8.4 Summary

The time of travel through the disk that an impactor experiences is dependent on its initial orbital velocity $v_\star$ and the thickness of the disk, $2H_{\rm d}$. When the impactor is on a unbound parabolic orbit it can reach speeds of $0.1c$ with a travel time of $t_{\rm transit} \sim 0.2$ days and would become bound to the SMBH after losing orbital energy to the disk. On bound circular orbits it is $t_{\rm transit} \sim 0.27$ days.

The shock heated gas releases photons that are assumed to random walk their way out to the surface of the disk. The photon diffusion time $t_{\rm diff}$ is defined as the amount of time required for the photons to random walk a distance R_0. It is dependent on the initial radius of the shock R_0, the total scattering cross section $\sigma_{\rm Tot}$, the number density of electrons n_e. Close to the SMBH $t_{\rm diff} \sim 0.2$ hrs and far from the SMBH $t_{\rm diff} \sim 215$ days.

If it is assumed that the photons released by the shocked gas travel with a sound wave propagating through the disk material, then the travel time is referred to as the sound crossing time t_s. When the distance travelled is the shock radius R_0, the time required is $t_{s,R_0} \sim 1.65$ hrs close to the SMBH and $t_{s,R_0} \sim 5.44$ hrs far from it. This makes t_{s,R_0} shorter (longer) than $t_{\rm diff}$ at large (small) radii.

When a volume of gaseous disk material is shock heated it will expand and cool to a point where its temperature is comparable to the surface temperature of the disk, where the time required to reach this is defined as the thermal timescale $t_{1\%}$. At small radii the expansion occurs on a timescale $t_{\rm diff}$ and at larger radii the expansion occurs on a timescale t_{s,R_0} yielding $t_{1\%} \sim 2.47$ years and $t_{1\%} \sim 86-159$ days, respectively. Since these timescales are longer than $t_{\rm transit}$ the shocked region of gas is still cooling long after the impactor has left the disk. The shocked volume is assumed to be that of a cylinder with a maximum length of $2H_{\rm d}$, where the radius of the cylinder is expanding on the shorter of the two timescales, t_{s,R_0} or $t_{\rm diff}$.

The shocked gas will push un-shocked gas out of the way as the impactor passes through the disk, and eventually slow down as it sweeps up more and more gas. This leads to a maximum cylindrical radius of $R_{\rm stall} \sim (8.3 - 11.5) \times 10^{11}$ cm depending on $v_\star$ and where the radial impact location is.

When an impactor is within the disk the photons emitted from the shock make their way to the surfaces of the disk where they can be observed. A code was developed to

model this emission profile for different radial impact locations, where the photon travel time is either $t_{\rm diff}$ or t_{s,R_0}. When the star first strikes the front side of the disk, there is an initial bright flare that quickly dims as the star plungers deeper into the disk. Once the star has emerged from the disk, energy is no longer deposited into the disk and the emission will fade until it reaches the disk's unperturbed surface luminosity.

As for the back side of the disk, the impactor is travelling at supersonic speeds and is thereby able to outpace the photons released from the shocked gas that are travelling in directions different than the star's trajectory. Since the photons random walk their way to the surface of the disk, photons that initially had their trajectories aligned with that of the impactors take on different trajectories that render them outpaced by the impactor. Thus, there is a very quick rise time to the peak emission which occurs when the impactor emerges from the back side of the disk. As expected, the back side emission peaks at a time $t_{\rm transit}$ later than the front side emission. Furthermore, the impactor is no longer inside the disk after the peak emission so the emission from the back side of the disk fades until it too reaches the unperturbed surface luminosity of the disk.

9 Most extreme scenarios

This section aims to investigate how most of the previously defined star-disk collisional phenomena are affected when the fiducial parameters are altered. When choosing how much the fiducial parameters should be altered by, we refer back to what is currently accepted in the literature. We start with parameters that affect the SMBH and it's efficiency at accreting matter, namely $M_\bullet$, $\dot{M}_{\rm d}$, and α.

SMBHs at the centres of AGNs have masses in the range of $M_\bullet \sim 10^6 - 10^{10}\ M_\odot$ (Trakhtenbrot, 2021). Rarely massive host galaxies harbour overmassive SMBHs with mass $M_\bullet \sim 10^{12}\ M_\odot$ (Hu et al., 2022). However, the overmassive $M_\bullet \sim 10^{12}\ M_\odot$ is difficult to accept and is not considered for the subsequent calculations, limiting the range we will use to $M_\bullet \sim 10^6 - 10^{10}\ M_\odot$.

The radiative efficiency of a quasar is related to the SMBH's mass accretion rate, which in Eddington ratios is given as $\dot{m} = \dot{M}_{\rm d}/\dot{M}_{\rm Edd}$. Typical $\dot{m}$ values are $0.01 - 0.1$, but some AGN have been observed to accrete matter at the Eddington limit $\dot{m} = 1$ (e.g. Lanzuisi et al., 2016; Wu et al., 2018), so we will use a range of $\dot{M}_{\rm d} = (0.01 - 1)\dot{M}_{\rm Edd}$.

The viscosity parameter α has been fiducially set to 0.1, so we use a range of $0.01 \leq \alpha \leq 1$ for our investigations. This parameter also aids in characterizing how effective the accretion disk is at transferring angular momentum outwards so that the matter within the disk loses energy and travels inwards.

Since the SNC is the source of impacting stars, it is worth exploring the effects of scaling its stellar density $n_{\rm SNC}$, varying the star's orbital parameters e and I, and altering the makeup of its stellar constituents, $M_\star$ and $R_\star$. Thus, we initially scale the SNC's density amplitude $n_{\rm SNC}$ (Pariev & Colgate, 2007) by $0.1 \leq n_{\rm SNC} \leq 10$.

The orbital inclination angle, relative to the accretion disk, of the impactors has been assumed to be face-on $I = \pi/2$, in most cases. More extreme values of the prograde $I = \pi/6$ and retrograde $I = 5\pi/6$ orbits cover a more realistic environment and are

therefore applied to scenarios where they had not been previously. It is noted that the inclination angle should not bring the star too close to the plane of the disk since this would cause them to be captured very quickly and not repeat a collision. Furthermore, the effects of a star skimming the surface of the disk before the collision are complicated and not fully investigated within this report.

The orbital eccentricity of the impactors, fiducially assumed to be parabolic, is also reduced to include less eccentric and circular orbits, which conforms closer to observed astrophysical environments. Evidently, this e and I have a minimal effect on the studied results and are only included when the outcomes are substantial.

Finally, we consider the individual impactor parameters by considering main sequence stars other than the fiducial sun-like impactor with $M_\star = M_\odot$ and $R_\star = R_\odot$. It is important to stick with MS stars since they can be approximated as solid rigid bodies that undergo negligible mass loss upon a star-disk collision, allowing them to have repeated collisions. A red giant star may have a dramatic first strike, where its outer envelope would more likely be torn away and a repeated collision of its core would not be as eventful, but cases such as these are excluded from this report.

9.1 Regional Boundaries

In this section we consider how the boundaries of both the accretion disk and SNC models change when various parameters are altered. These boundaries delineate the radial extent of their respective regions and so we compare these investigations to the fiducial values. However, before we begin a brief discussion of how the Schwarzschild radius is affected is required to properly interpret our subsequent findings.

The Schwarzschild radius $R_{\rm g}$, which is only dependent on $M_\bullet$, is a seemingly trivial

calculation.

$$R_{\rm g}[\rm cm] = \frac{2GM_\bullet}{c^2} \sim \begin{cases} 2.95 \times 10^{11} & \text{if } M_\bullet = 10^6 M_\odot \\ 2.95 \times 10^{13} & \text{if } M_\bullet = 10^8 M_\odot \\ 2.95 \times 10^{15} & \text{if } M_\bullet = 10^{10} M_\odot \end{cases} \tag{9.1}$$

This distance is directly proportional to $M_\bullet$ and scales accordingly, as the mass of the SMBH increases so does the Schwarzschild radius. Unfortunately, With $R_{\rm g}$ changing for different values of $M_\bullet$ some ambiguity is introduced when using it as a radial (spatial) measurement for comparison between altered parameters. For this reason we provide the results of our subsequent investigations in both unit $R_{\rm g}$ and unit cm for clarity.

9.1.1 Disk Boundaries

The boundary between region (a) and region (b) for the α-disk model of Shakura & Sunyaev (1973) lies at the radius $r_{\rm ab}$ and is dependent on $M_\bullet$, $\dot{M}_{\rm d}$, and α. In both regions the main source of scattering is due to Thompson scattering, however the pressure is dominated by radiation in region (a) and gas in region (b).

Increasing (decreasing) any of the dependent quantities results in a larger (smaller) value for $r_{\rm ab}$, which in turn means a larger (smaller) radiative region (a). For the range in which we are allowing the parameters to vary, the largest value that $r_{\rm ab}$ can attain is $\sim 1344 R_{\rm g} \sim 3.96 \times 10^{18}$ cm when $M_\bullet = 10^{10} M_\odot$, $\dot{M}_{\rm d} = \dot{M}_{\rm Edd}$, and $\alpha = 1$, while the smallest value that $r_{\rm ab}$ can attain is $\sim 10.79 R_{\rm g}$ ($\sim 3.18 \times 10^{12}$ cm) when $M_\bullet = 10^6 M_\odot$, $\dot{M}_{\rm d} = 0.01 \dot{M}_{\rm Edd}$, and $\alpha = 0.01$. Compared to the fiducial value of $r_{\rm ab} \sim 120.5 R_{\rm g}$ ($\sim 3.55 \times 10^{15}$ cm), these new values bring the boundary to ~ 1115 times further and closer to the SMBH in unit cm. The aforementioned ambiguity is first revealed here where the change in $r_{\rm ab}$ is only ~ 11 times further and closer to the SMBH when considering unit $R_{\rm g}$.

The change in the spatial extent of the gaseous region (b) is not as straightforward

due to the outer boundary $r_{\rm bc}$ delineating where region (c) begins. The pressure of region (c) is also mainly due to the gaseous disk material, but its opacity is dominated by free-free absorption. This outer boundary's only dependence is $\dot{M}_{\rm d}$, and thus takes on only 3 values for the three different mass accretion rates that are being investigated,

$$r_{\rm bc}[R_{\rm g}] = 8000\ \dot{m}_{\rm ss}^{2/3} \sim \begin{cases} 371 & \text{if } \dot{M}_{\rm d} = 0.01\dot{M}_{\rm Edd} \\ 1723 & \text{if } \dot{M}_{\rm d} = 0.1\dot{M}_{\rm Edd} \\ 8000 & \text{if } \dot{M}_{\rm d} = \dot{M}_{\rm Edd} \end{cases} \tag{9.2}$$

Here the results are given in unit $R_{\rm g}$. If the boundary is instead represented in unit cm then for each $\dot{M}_{\rm d}$ $r_{\rm bc}$ takes on 3 different values for each $M_\bullet$, yielding a total of 9 unique radii.

To estimate the radial extent of region (b) for each of the 3 $\dot{M}_{\rm d}$ cases we give the range of values that $r_{\rm ab}$ can be.

$$r_{\rm ab} \sim \begin{cases} (10.8 - 40.2)R_{\rm g} \approx (0.318 - 18700) \times 10^{13}\ \text{cm} & \text{if } \dot{M}_{\rm d} = 0.01\dot{M}_{\rm Edd} \\ (62.4 - 232.6)R_{\rm g} \approx (1.84 - 68600) \times 10^{13}\ \text{cm} & \text{if } \dot{M}_{\rm d} = 0.1\dot{M}_{\rm Edd} \\ (360.6 - 1344)R_{\rm g} \approx (1.06 - 39600) \times 10^{14}\ \text{cm} & \text{if } \dot{M}_{\rm d} = \dot{M}_{\rm Edd} \end{cases} \tag{9.3}$$

Here the minima correspond to $M_\bullet = 10^6 M_\odot$ and $\alpha = 0.01$, while the maxima correspond to $M_\bullet = 10^{10} M_\odot$ and $\alpha = 1$ (see Table A.1 in Appendix A for a more detailed breakdown). The difference between these two boundaries, $r_{\rm bc} - r_{\rm ab}$, defines the radial extent of region (b). Therefore, when changing $M_\bullet$ and α, in the same manner as equation (9.3), the

radial size of region (b) is able to be:

$$r_{\rm bc} - r_{\rm ab} \sim \begin{cases} (331 - 360) R_{\rm g} \approx (1.063 - 9757) \times 10^{14} \text{ cm} & \text{if } \dot{M}_{\rm d} = 0.01 \dot{M}_{\rm Edd} \\ (1661 - 1490) R_{\rm g} \approx (4.899 - 43970) \times 10^{14} \text{ cm} & \text{if } \dot{M}_{\rm d} = 0.01 \dot{M}_{\rm Edd} \\ (7639 - 6656) R_{\rm g} \approx (2.254 - 1964) \times 10^{15} \text{ cm} & \text{if } \dot{M}_{\rm d} = \dot{M}_{\rm Edd} \end{cases} \tag{9.4}$$

Comparing to the fiducial radial extent of region (b) $r_{\rm bc} - r_{\rm ab} \sim 1602 R_{\rm g}$ ($\sim 4.73 \times 10^{16}$ cm), the smallest radial extent, when $M_\bullet = 10^6$ and $\alpha = 0.01$, is ~ 445 (~ 4.8) times smaller in unit cm ($R_{\rm g}$) while the largest radial extent, when $M_\bullet = 10^{10}$ and $\alpha = 1$, is ~ 415 (~ 4.2) times larger in unit cm ($R_{\rm g}$).

9.1.2 SNC Boundaries

Much like the accretion disk model the SNC has two boundaries, r_1 and r_2, that delineate three regions. However, only two of its three regions, region (1) and (2), contain a stellar population, the inner most being void of stars. An increase (decrease) in r_1 corresponds to an increase (decrease) in the radial extent of the stellar void and a decrease (increase) of the radial extent of region (1).

As described earlier in section §3.1.1, the inner SNC boundary r_1 is dependent on r_t which is dependent on $M_\bullet$ and the parameters of the orbiting star (see equation (3.7)). When considering other stars as impactors, it is important to stick with main-sequence (MS) stars since they can be approximated as solid rigid bodies that undergo negligible mass loss upon a star-disk collision, allowing them to have repeated collisions. Albeit, a red giant star may have a dramatic first strike, its outer envelope would more likely be torn away and a repeated collision of its core would not be as eventful (Kieffer & Bogdanović, 2016). We consider only late-type MS stars as impactors, so that we can employ the upper limits of their masses and radii, which along with the MS population fraction, are provided in table 9.1. Both late K and M stars are chosen for making up

Spectral Class	MS Mass $[M_\odot]$	MS Radius $[R_\odot]$	MS Fraction [%]
A	2.1	1.8	0.6
K	0.8	0.96	12.1
M	0.45	0.7	76.45

Table 9.1: Different values for late main-sequence (MS) stars. Habets & Heintze (1981) provides the masses and radii, and the population fraction is provided by Ledrew (2001).

$\sim 88\%$ of all MS stars, whereas late A stars are chosen because both their mass and radius are about double that of solar units.

When the SNC is comprised of a collection of one of these late-type MS stars, instead of a sun-like star, r_1 is altered. The results of which are listed in table 9.2

$M_\bullet$ $[M_\odot]$	$10^6 M_\odot$			$10^8 M_\odot$			$10^{10} M_\odot$		
Spectral Class	M	K	A	M	K	A	M	K	A
r_1 $[R_\mathrm{g}]$	271	307	417	12.6	14.2	19.3	0.58	0.66	0.90
r_1 $[\times 10^{13}$ cm]	7.99	9.06	12.3	37.2	41.9	56.9	171	195	266

Table 9.2: The inner SNC boundary r_1 for differing SMBH masses $M_\bullet$ and main-sequence spectral classes, in units of R_g and cm. The mass and radius for each spectral class M, K, and A are $M_\mathrm{M} = 0.45 M_\odot$ and $R_\mathrm{M} = 0.7 R_\odot$), ($M_\mathrm{K} = 0.8 M_\odot$ and $R_\mathrm{K} = 0.96 R_\odot$), and ($M_\mathrm{A} = 2.1 M_\odot$ and $R_\mathrm{A} = 1.8 R_\odot$), respectively.

Compared to the fiducial value of $r_1 \sim 14 R_\mathrm{g}$ ($\sim 40.7 \times 10^{13}$ cm), these altered values, in unit cm, are at least ~ 5.09 times smaller when $M_\bullet = 10^6 M_\odot$ and $M_\star = M_\mathrm{M}$, and are at most ~ 6.54 times larger when $M_\bullet = 10^{10} M_\odot$ and $M_\star = M_\mathrm{A}$.

Unlike the other boundaries covered so far, the outer boundary of the SNC r_2 is at a fixed radial location of 10^{-2} pc. This value can be reinterpreted in unit cm or, for the differing SMBH masses, in unit R_g,

$$r_2 \approx 3.086 \times 10^{16} \text{ cm} \approx \begin{cases} 10.45 \times 10^4 R_\mathrm{g} & \text{if } M_\bullet = 10^6 M_\odot \\ 10.45 \times 10^2 R_\mathrm{g} & \text{if } M_\bullet = 10^8 M_\odot \\ 10.45 R_\mathrm{g} & \text{if } M_\bullet = 10^{10} M_\odot \end{cases} \tag{9.5}$$

Thus, r_2 does not change when any of the considered parameters are altered, but appears to when viewed in unit $R_{\rm g}$.

It is important to keep these changing boundaries (regions), for both the SNC and the accretion disk, in mind when reading further into our investigations. Graphical representations of affected quantities will have these different boundaries depicted. Thus, the information provided here will prove useful when interpreting these visual depictions.

9.2 Change in Models

This section covers how the accretion disk and SNC models are affected when varying $M_\bullet$, $\dot{M}_{\rm d}$, α, and the amplitude of $n_{\rm SNC}$.

9.2.1 SNC Number Density Amplitude

The SNC density profile's amplitude is scaled to a tenth and ten times its fiducial value, thereby effectively increasing and decreasing the total number of stars in regions (1) and (2), depicted in Figure 9.1.

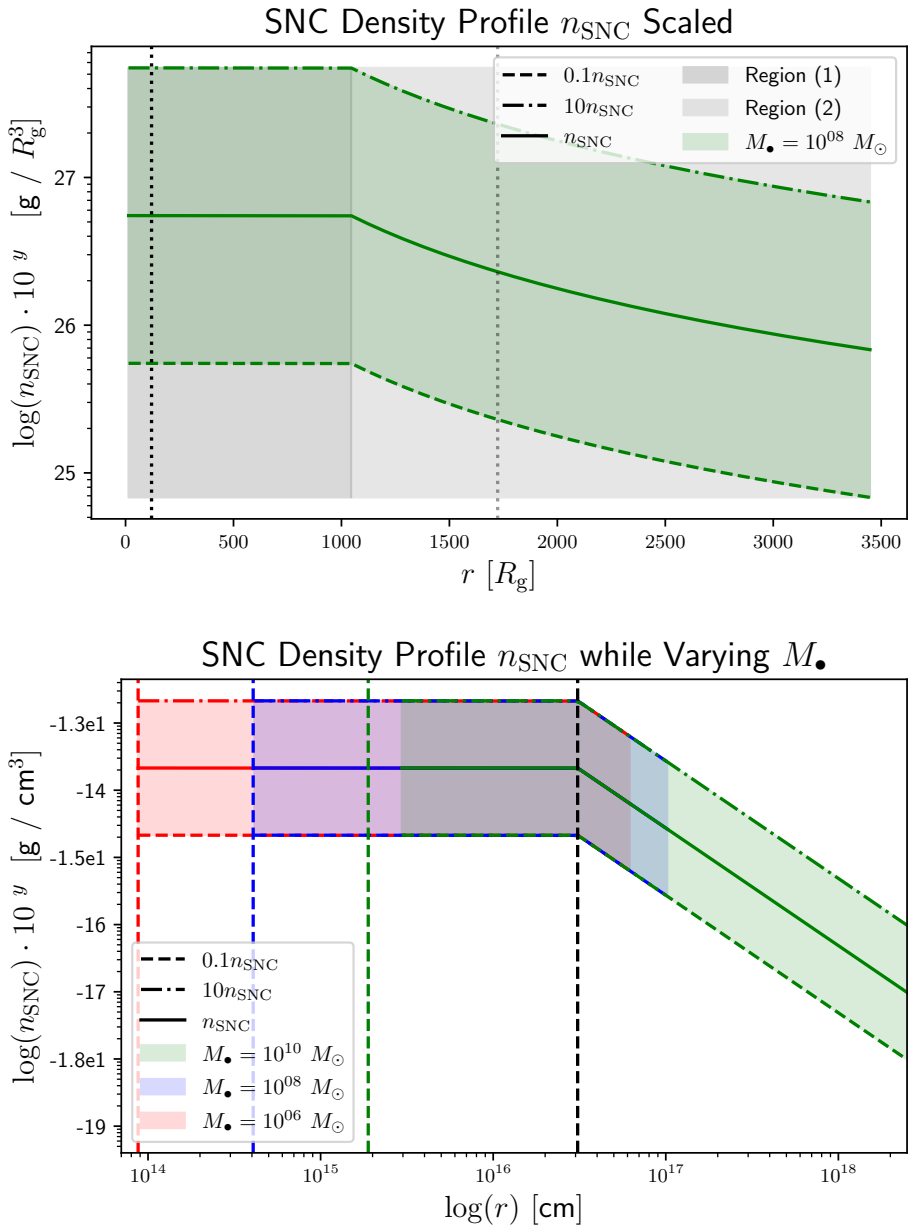

Figure 9.1: SNC density profile n_{SNC} as a function of R_{g} surrounding the fiducial SMBH mass of $10^8 M_\odot$ with scaled amplitudes, where the solid line is the fiducial (unscaled) n_{SNC}, the dashed line is $0.1n_{\mathrm{SNC}}$, and the dash-dotted line is $10n_{\mathrm{SNC}}$. The vertical lines indicate the disk's regional boundaries (dotted), r_{ab} (darker) and r_{bc} (lighter), and the SNC regional boundaries (dashed), r_1 (darker) and r_2 (lighter), where region (1) (dark-gray) is bounded by r_1 and r_2 and region (2) (light gray) has a lower bound of r_2. When these boundaries change they are assigned a colour, respective of which parameter value is being altered, and are black when the boundary is unaffected by the parameter change. In the rightmost plot the scaled n_{SNC} is plotted as a function of radius r in unit cm and the value of $M_\bullet$ is varied to $10^6 M_\odot$ (blue), $10^8 M_\odot$ (green), and $10^{10} M_\odot$ (red). The r_2 boundary is the same for all $M_\bullet$, but r_1 increases with $M_\bullet$. Note that the y-axis in both plots is log scaled, as well as the x-axis of the right plot.

Altering the values for both α and $\dot{M}_{\rm d}$ had no effect on the $n_{\rm SNC}$, so there is no graphical representation for these changes. However changing $M_\bullet$ alters where the stars are radially found, due to the r_1 boundary being dependent on the mass of the SMBH (Figure 9.1). As $M_\bullet$ increases, the inner boundary of the SNC r_1 becomes further from the SMBH, which causes the starless core to become larger, while r_2 remains the same thereby truncating the extent that region (1) covers.

9.2.2 Accretion Disk Half-Thickness

The α-model accretion disk's half-thickness $H_{\rm d}$ is dependent on α, $\dot{M}_{\rm d}$, and $M_\bullet$. Figure 9.2 graphically shows how $H_{\rm d}$ is affected when changing the values of these parameters.

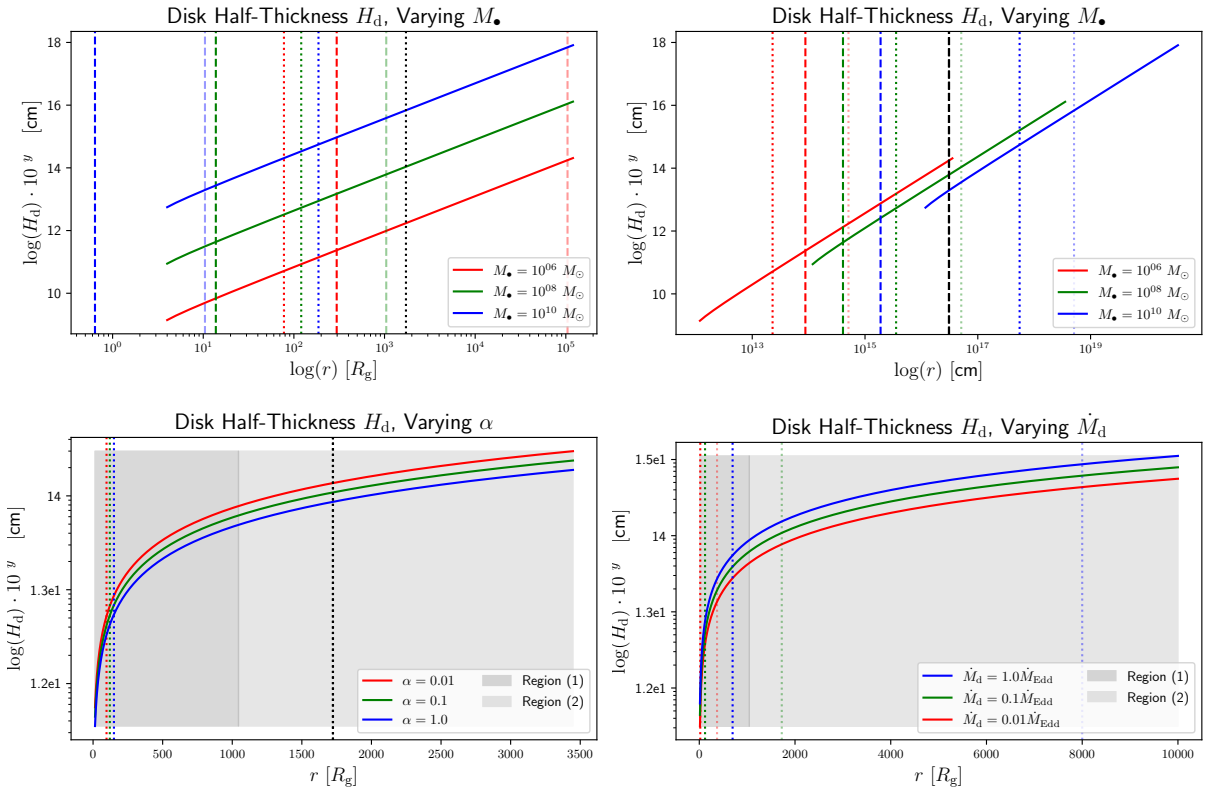

Figure 9.2: The half-thickness $H_{\rm d}$ of the accretion disk as a function of radius r for varying SMBH mass $M_\bullet$ (first and second panel) viscosity α parameter (third panel) and mass accretion rate $\dot{M}_{\rm d}$ (fourth panel). An increase of $M_\bullet$ and $\dot{M}_{\rm d}$ result in a thicker disk, while increasing α thins the disk. The vertical lines indicate the disk's regional boundaries (dotted), $r_{\rm ab}$ (darker) and $r_{\rm bc}$ (lighter), and the SNC regional boundaries (dashed), r_1 (darker) and r_2 (lighter), where region (1) (dark-gray) is bounded by r_1 and r_2 and region (2) (light gray) has a lower bound of r_2. When these boundaries change they are assigned a colour, respective of which parameter value is being altered, and are black when the boundary is unaffected by the parameter change. Note that the y-axis is log scaled for all plots, as well as the x-axis when varying $M_\bullet$, and the x-axis is given in unit cm for the top-right plot and unit $R_{\rm g}$ for all others.

As $M_\bullet$ and $\dot{M}_{\rm d}$ are increased so does $H_{\rm d}$, however an increase of α decreases the thickness of the disk. When varying α and $\dot{M}_{\rm d}$ the thickness of the disk is comparable at the fiducial radii ($H_{\rm d} \sim (10^{12}, 10^{13}, 10^{14}$ cm at $r = (100, 500, 2000) R_{\rm g}$). In both of these cases the difference at its greatest plotted radial extent is less than an order of magnitude, indicating that these parameters do not have a great effect on $H_{\rm d}$. Whereas a change in $M_\bullet$ has a greater effect on the disk's half-thickness, yielding $H_{\rm d} \sim (4.3, 270, 1700) \times 10^{11}$ cm for $M_\bullet = (10^6, 10^8, 10^{10}) M_\odot$ at $500 R_{\rm g}$.

9.2.3 Accretion Disk Mass Density

The α-model accretion disk's volumetric mass density ρ_{d} is dependent on $M_{\bullet}$, $\dot{M}_{\mathrm{d}}$, and α. Figure 9.3 illustrates how altering these parameters affects ρ_{d}.

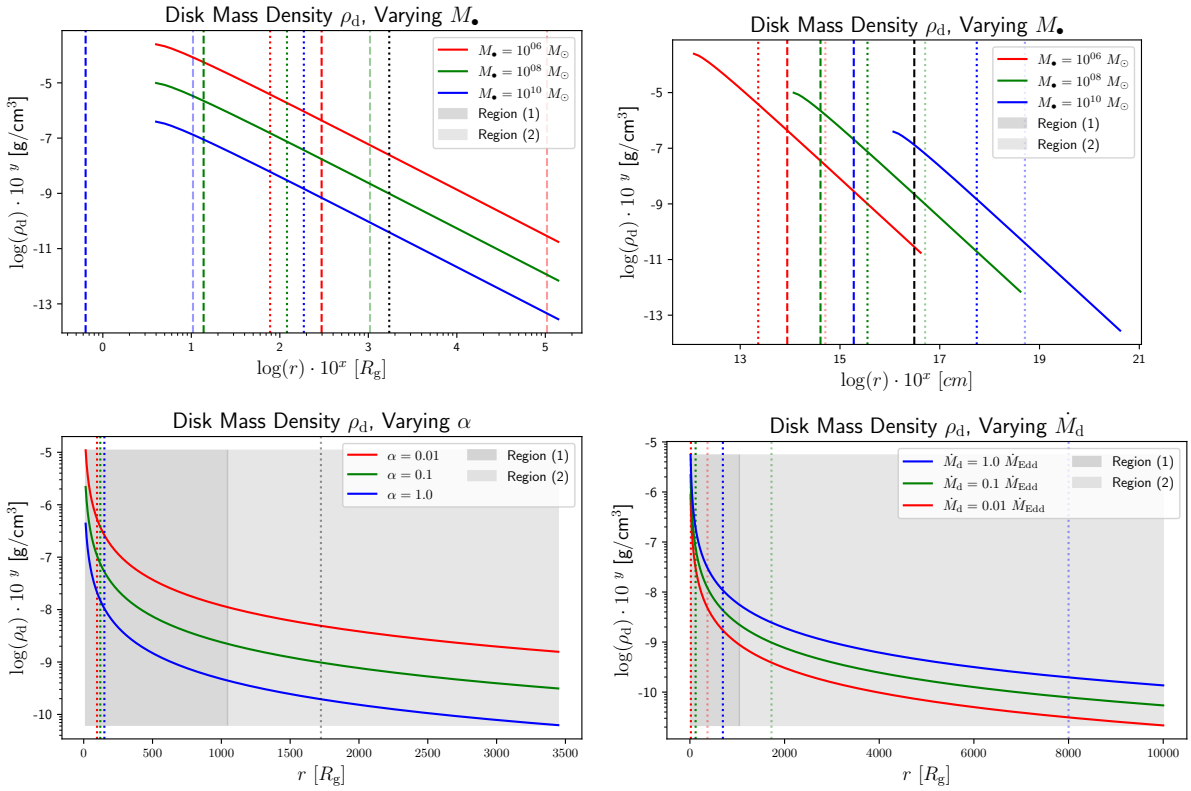

Figure 9.3: The volume mass density ρ_{d} of the accretion disk as a function of r for varying $M_{\bullet}$ (first and second panel), α (third panel), and $\dot{M}_{\mathrm{d}}$ (fourth panel). The vertical lines indicate the disk's regional boundaries (dotted), r_{ab} (darker) and r_{bc} (lighter), and the SNC regional boundaries (dashed), r_1 (darker) and r_2 (lighter), where region (1) (dark-gray) is bounded by r_1 and r_2 and region (2) (light gray) has a lower bound of r_2. The colours of the vertical lines are respective of which parameter value is being altered, and are black when the boundary is unaffected by the parameter change. Note that the y-axis is log scaled for all plots, as well as the x-axis when varying $M_{\bullet}$, and the x-axis is given in unit cm for the top-right plot and unit R_{g} for all others.

The mass density is densest at small radii and decreases further away from the SMBH, Varying $M_{\bullet}$ is displayed in unit r_{g} and unit cm for clarity. Disks that orbit larger $M_{\bullet}$ have less density ($\rho_{\mathrm{d}} \sim 2.9 \times 10^{-10}$ g cm^{-3} at $500R_{\mathrm{g}}$), and smaller $M_{\bullet}$ results in more dense disks ($\rho_{\mathrm{d}} \sim 1.8 \times 10^{-7}$ g cm^{-3} at $500R_{\mathrm{g}}$). The mass density of the disk is also decreased when $\dot{M}_{\mathrm{d}}$ is decreased ($\rho_{\mathrm{d}} \sim 10^{-8} - 10^{-9}$ g cm^{-3} at $500R_{\mathrm{g}}$) or α is increased

($\rho_{\rm d} \sim 10^{-8} - 10^{-9}$ g cm^{-3} at $500R_{\rm g}$), and much like $H_{\rm d}$ is comparable at all fiducial radii. A change in α affects $\rho_{\rm d}$ significantly more than $\dot{M}_{\rm d}$.

More dense disks generate a stronger drag force felt by the transiting impactor, since $F_{\rm drag} \propto \rho_{\rm d}$, and would slow the impactor more.

9.3 Changes in Collisional Phenomena

This section covers how phenomena strictly related to a star-disk collision are affected by altering the values of $M_\bullet$, α, $\dot{M}_{\rm d}$, and the amplitude of $n_{\rm SNC}$.

9.3.1 Relative Velocity

The velocities of both the disk $v_{\rm d}$ and the impactor $v_\star$ are affected by the SMBH mass since $v \propto \sqrt{M}$, and thus the difference between them, the relative velocity $v_{\rm rel}$, is also affected. Figure 9.4 contains two plots of the relative velocity for an impactor on a bound circular orbit striking the disk at different inclination angles I.

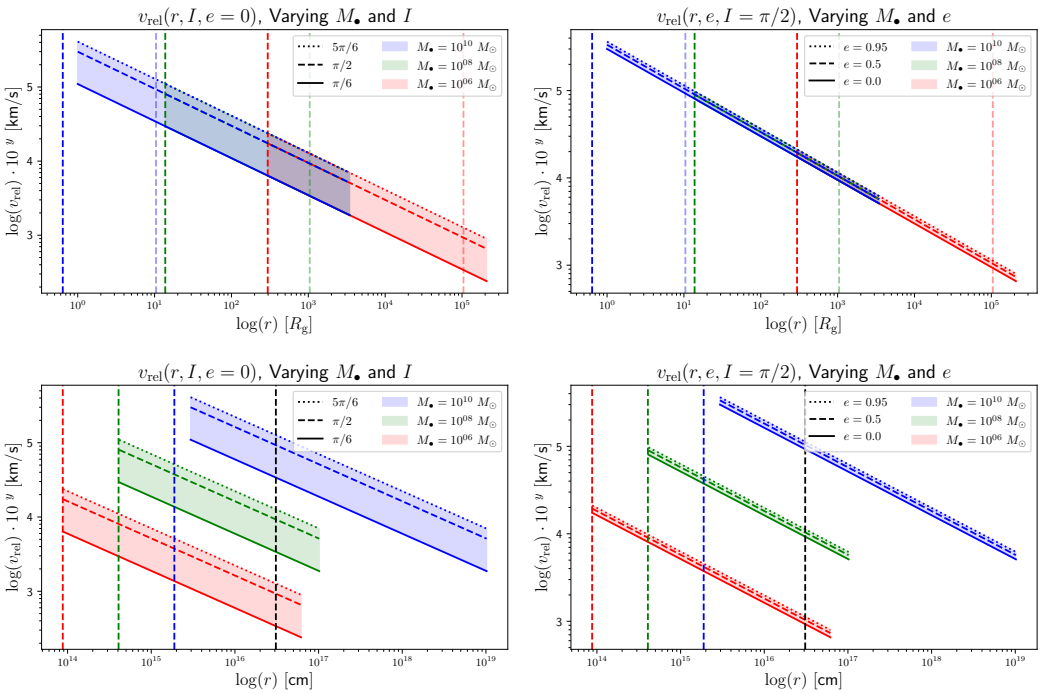

Figure 9.4: Relative velocity $v_{\rm rel}$ between the disk and an impactor on a bound orbit with varying orbital inclination angles I (first column), orbital eccentricities e (second column), and SMBH mass $M_\bullet$ in unit $R_{\rm g}$ (first row) and unit cm (second row). The vertical dashed lines indicate the SNC regional boundaries, r_1 (darker) and r_2 (lighter), where region (1) is bounded by r_1 and r_2 and region (2) has a lower bound of r_2. When these boundaries change they are assigned a colour, respective of which parameter value is being altered, and are black when the boundary is unaffected by the parameter change. The solid curve represents the $I = \pi/6$ and $e = 0$, the dashed curve represents the $I = \pi/2$ and $e = 0.5$, and the dotted curve represents the $I = 5\pi/6$ and $e = 0.95$, for changing the orbital inclination angle and eccentricity, respectively.

As the mass of the SMBH increases so does the relative velocity, with the entire distribution of $v_{\rm rel}$ (either changing I or e) being faster for all r, in unit cm, for a more massive $M_\bullet$. This effect is obscured when r is in unit $R_{\rm g}$, where the $v_{\rm rel}$ plots are overlaid for differing $M_\bullet$, but is clearly visible when viewed in unit cm.

Impactors striking the disk with a retrograde orbital inclination experience the quickest $v_{\rm rel}$, while those with a prograde orbital inclination experience the slowest $v_{\rm rel}$. It is assumed that the disk is rotating in the positive x direction at $y = 0$ and retrograde orbits have negative x, y velocity components while prograde orbits have positive x, y velocity components. Since $v_{\rm rel}$ is defined as the difference between the two velocities,

these velocities sum when the $I > \pi/2$ and are subtracted from each other when $I < \pi/2$. Interestingly, the difference from a face-on ($I = \pi/2$) collision is greater for prograde orbits than retrograde orbits, which is due to the negative x, y velocity components of retrograde orbits.

When considering different eccentricities, impactors colliding with the disk on highly eccentric ($e = 0.95$) orbits experience a faster $v_{\rm rel}$ than those on circular ($e = 0$) orbits. Impactors are assumed to strike the disk face-on at periapse where $z = 0$. Highly eccentric orbits have most of their velocity in the z direction, with little in the x, y directions, so the relative velocity ends up being greater than circular orbits that have most of their velocity in the x, y directions with little in the z direction. The difference in $v_{\rm rel}$ between $e = 0$ and $e = 0.95$ is $\approx \sqrt{2}$, but effects of this result in the eccentricity having far less of an effect on an impactor's transit through the disk than the maximum effects of the inclination angle.

9.3.2 Average Time Between Collisions

As seen in Figure 9.1, the number of stars in the populated regions of the SNC decreases as r increases, so one may naively assume that the average time between collisions would decrease as they moved away from the SMBH. One must remember that $\Delta T_c(r)$ considers all star-disk collisions out to a radius r, such that as r increases a greater total number of stars are encompassed by the greater distance and $\Delta T_c(r)$ decreases. This is visualized by imagining an observer at a specific r looking back towards the SMBH and counting the amount of observed impacts over a given time period.

Since $\Delta T_c(r)$ only changes when varying the amplitude of $n_{\rm SNC}$ and adjusting $M_\bullet$ only these two variations are depicted in Figure 9.5, where r is depicted in unit cm and unit $R_{\rm g}$.

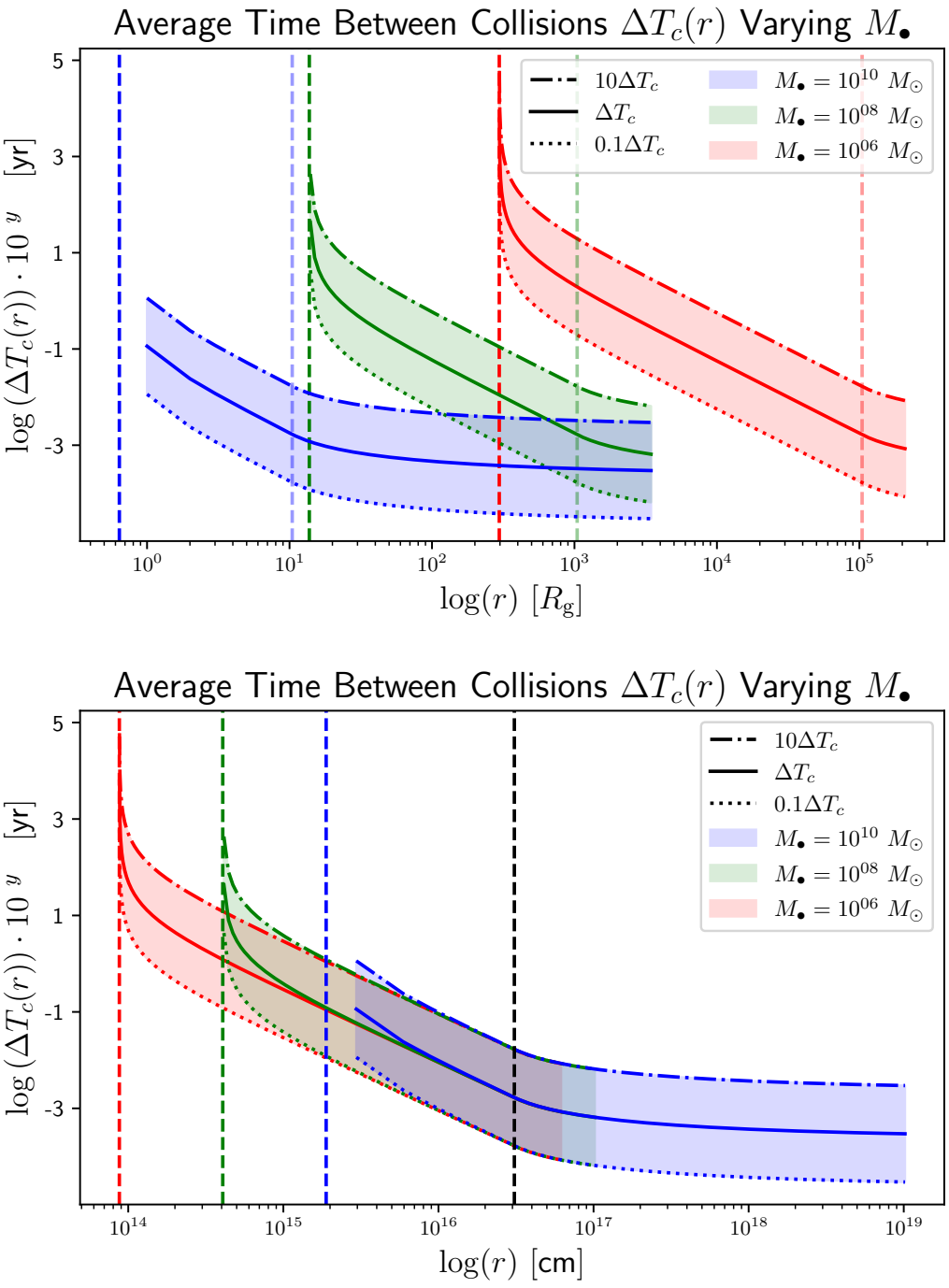

Figure 9.5: Average Time Between Collisions $\Delta T_c(r)$ with scaled SNC profile amplitudes $(0.1-10)N_{\rm SNC}$. Here $M_\bullet$ is being varied and it is displayed in unit $R_{\rm g}$ (first panel) and unit cm (second panel). The vertical dashed lines indicate the SNC regional boundaries, r_1 (darker) and r_2 (lighter), where region (1) is bounded by r_1 and r_2 and region (2) has a lower bound of r_2. When these boundaries change they are assigned a colour, respective of which parameter value is being altered, and are black when the boundary is unaffected by the parameter change. Note that the y-axis is log scaled for all plots, as well as the x-axis when varying $M_\bullet$, and the x-axis is given in unit cm (right) and unit $R_{\rm g}$ (left).

In both graphs the amplitude of $n_{\rm SNC}$ is scaled by a factor of 0.1,1, and 10 times the fiducial value (dotted, solid, and dash-dotted lines), the range of which is indicated by the shaded coloured regions for each of the chosen $M_\bullet$ values.

When the amplitude of $n_{\rm SNC}$ is scaled to greater values there is a greater number of stars that can collide with the disk. Thus $\Delta T_c(r)$ decreases when $n_{\rm SNC}$ is scaled upward, and increases when $n_{\rm SNC}$ is scaled downwards.

When the SMBH mass is increased (decreased) the starless core of the SNC increases (decreases) in radial extent, which is reflected in the differing location of r_1 and the behaviour of $\Delta T_c(r)$. Larger values of $M_\bullet$ result in larger values of r_1, and hence a larger core and smaller region (1), when viewed in unit cm. When viewed in unit $R_{\rm g}$ both r_1 and r_2 appear to decrease in value when $M_\bullet$ increases, due to that somewhat arbitrary value of $R_{\rm g}$ also changing. Although these units are ambiguous, this representation clearly illustrates differing values of $M_\bullet$ do not change the overall shape of $\Delta T_c(r)$, but instead reduce it.

A larger core reduces the amount of collisions at small r, but at sufficiently large radii ($r > r_2$) this effect averages out and $\Delta T_c(r)$ becomes indistinguishable for differing $M_\bullet$. The orbital velocities of the impactor are proportional to the SMBH mass, $v_\star \propto M_\bullet$, so when $M_\bullet$ is larger so are the stellar velocities. Therefore, even though there are less stars in region (1) of the SNC when $M_\bullet$ is greatest, $v_\star$ is greater and the average time between their collisions with the disk is decreased at small r.

9.3.3 Collisional Rate

Like $\Delta T_c(r)$ the collisional rate $\mathcal{R}_c$ also takes into account all star-disk collisions that occur within a radius r, such that $\mathcal{R}_c$ increases in the constant stellar number region (1) and decreases beyond r_2. The collisional rate, which is derived from $\Delta T_c(r)$, is also changed when varying the amplitude of $n_{\rm SNC}$ and adjusting $M_\bullet$, Figure 9.6.

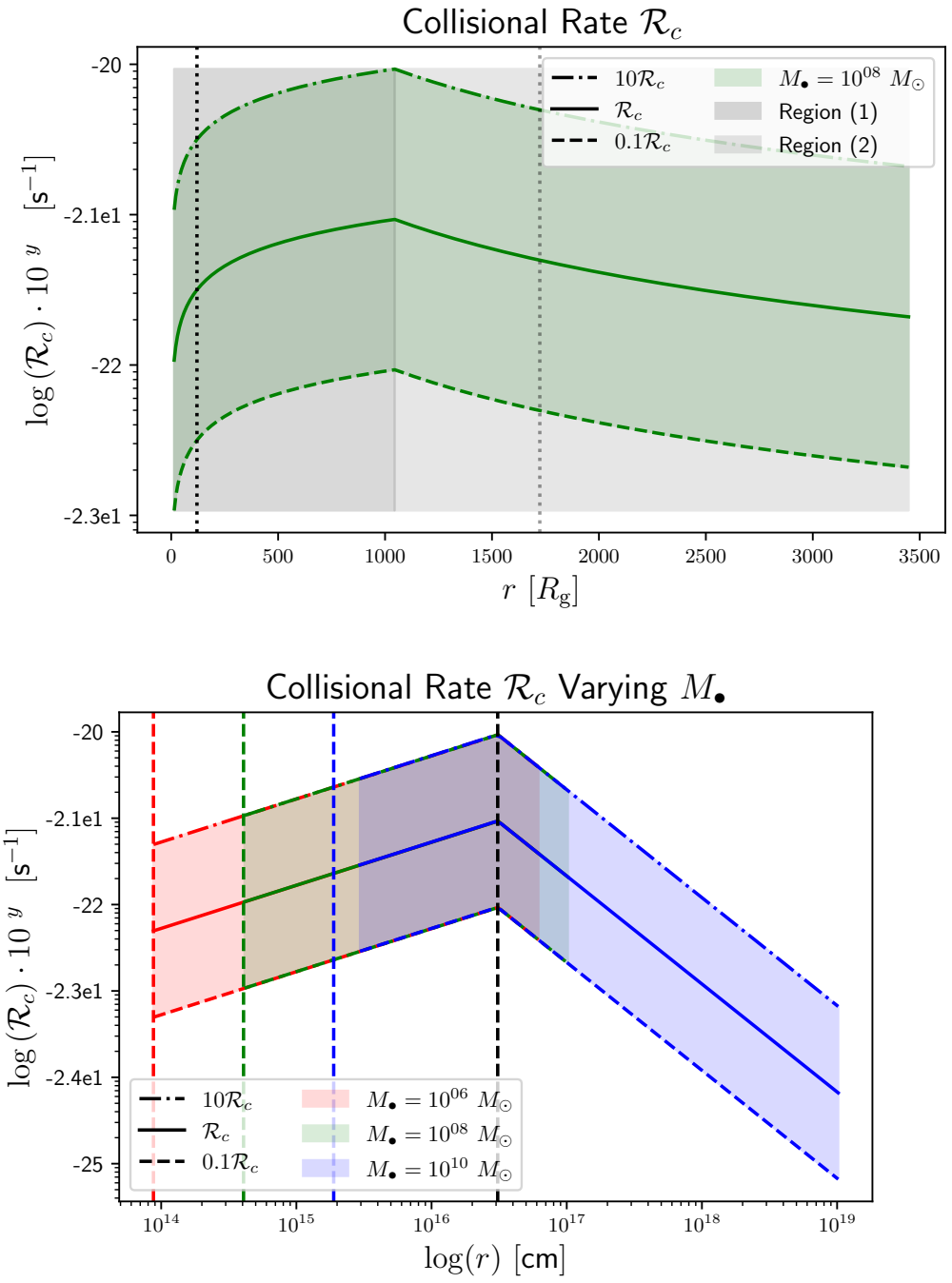

Figure 9.6: Collision Rate $\mathcal{R}_c$ with scaled SNC profile amplitudes as a function of radius R when varying n_{SNC} (left) and $M_\bullet$ (right). The vertical lines indicate the disk's regional boundaries (dotted), r_{ab} (darker) and r_{bc} (lighter), and the SNC regional boundaries (dashed), r_1 (darker) and r_2 (lighter), where region (1) (dark-gray) is bounded by r_1 and r_2 and region (2) (light gray) has a lower bound of r_2. When these boundaries change they are assigned a colour, respective of which parameter value is being altered, and are black when the boundary is unaffected by the parameter change. Note that the y-axis is log scaled for all plots, as well as the x-axis when varying $M_\bullet$, and the x-axis is given in unit cm (right) and unit R_g (left).

In both plots the amplitude of $n_{\rm SNC}$ is scaled by a factor of 0.1,1, and 10 times the fiducial value (dashed, solid, and dash-dotted lines, respectively), the range of which is indicated by the shaded coloured regions for each of the chosen $M_\bullet$ values. Increasing the total amount of stars within the SNC increases the amount of stars available to collide with the disk, which increases the $\mathcal{R}_c$.

An increased value of $M_\bullet$ (larger region (1) and SNC core) changes the radial location of r_1, which in turn causes the non-zero values of $\mathcal{R}_c$ to occur in different radial regions. However, unlike $\Delta T_c(r)$, this causes no change in the behaviour or $\mathcal{R}_c$, since the collisional rate is indistinguishable for all $M_\bullet$ at radii where stars are present.

9.3.4 Change in Orbital Energy

The change in orbital energy $\Delta\mathcal{E}$ is dependent on all parameters, Figure 9.7.

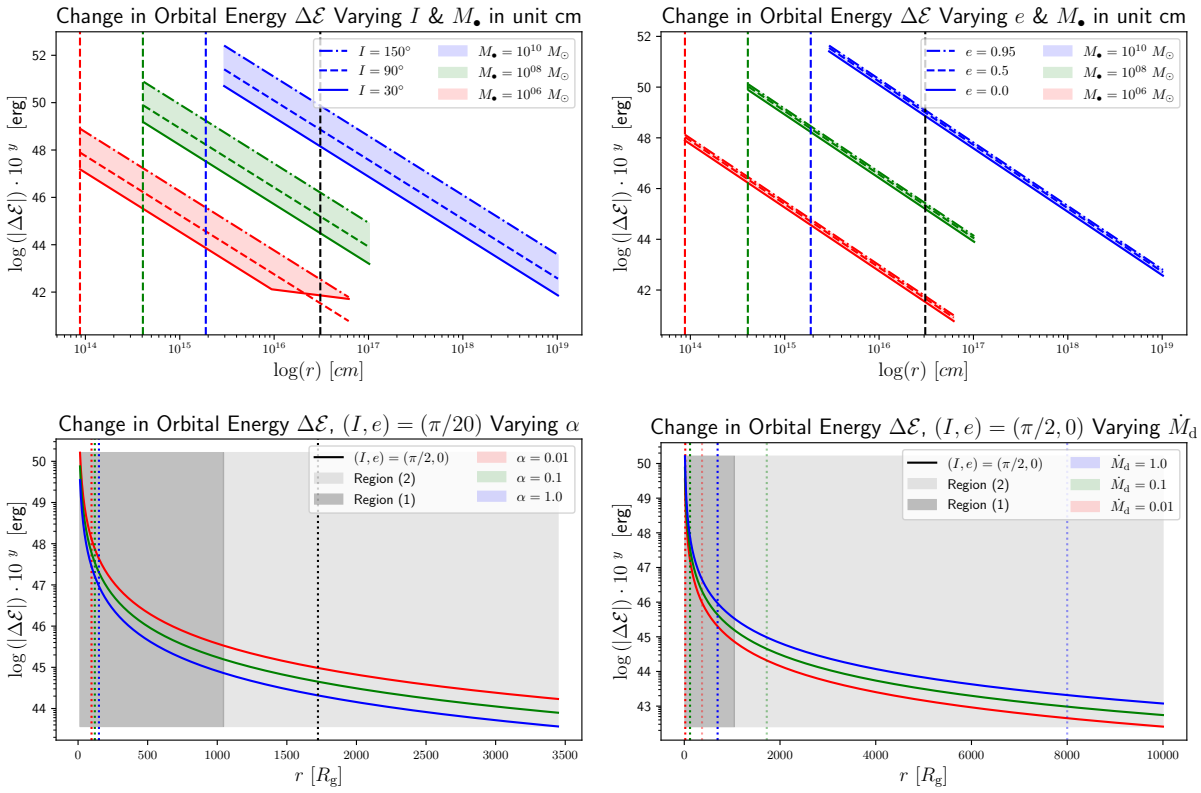

Figure 9.7: The absolute change in orbital energy $|\Delta\mathcal{E}(r)|$ with different orbital inclinations and eccentricities as a function of radius r. The parameters being varied are $M_\bullet$ (first and second panel), α (third panel), and $\dot{M}_d$ (fourth panel). The orbital and inclination angle is set to $I = \pi/2$ and $e = 0$ when changing α and $\dot{M}_d$ to highlight the variation. The vertical lines indicate the disk's regional boundaries (dotted), r_{ab} (darker) and r_{bc} (lighter), and the SNC regional boundaries (dashed), r_1 (darker) and r_2 (lighter), where region (1) (dark-gray) is bounded by r_1 and r_2 and region (2) (light gray) has a lower bound of r_2. When these boundaries change they are assigned a colour, respective of which parameter value is being altered, and are black when the boundary is unaffected by the parameter change. The plotted solid line represents the $I = \pi/6$ and $e = 0$, dashed line represents the $I = \pi/2$ and $e = 0.5$, and dotted line represents the $I = 5\pi/6c$ and $e = 0.95$, for the different orbital inclinations angle and eccentricities, respectively. Note that the y-axis is log scaled for all plots, as well as the x-axis when varying $M_\bullet$, and the x-axis is given in unit cm (top) and unit R_g elsewhere.

The stellar orbital inclination and eccentricity take on differing values when changing $M_\bullet$ to determine the change in orbital energy, depicted in the top graphs in Figure 9.7. Larger values of $M_\bullet$ result in greater amounts of orbital energy being lost from the impactor, in all cases. When the impactor is on a bound Keplerian circular orbit ($e = 0$),

the amount of energy lost is greatest for retrograde orbits (dash-dotted curve) and the least for prograde orbits (solid curve). When the impactor is instead striking the disk at $I = \pi/2$ with respect to the disk plane, the amount of energy lost is greatest for highly eccentric orbits (dash-dotted curve) and the least for circular orbits (solid curve).

When varying α and $\dot{M}_{\rm d}$ the orbital inclination and eccentricity (solid curves) were set to $I = \pi/2$ and $e = 0$ to clearly illustrate how $\Delta\mathcal{E}$ changes. Accretion disks with smaller α and larger $\dot{M}_{\rm d}$ increase the amount of orbital energy that is lost from an impactor upon colliding with the disk. However, altering these parameters does not have as great of an effect as varying $M_\bullet$.

Thus a star on a highly eccentric ($e \sim 0.95$) retrograde ($I \sim 5\pi/6$) orbit that collided with an accretion disk accreting at the Eddington rate ($\dot{M}_{\rm d}$) with a low viscosity $\alpha \sim 0.01$), orbiting an overly massive SMBH ($M_\bullet \sim 10^{10} M_\odot$) would incur the greatest $|\Delta\mathcal{E}|$.

9.3.5 Time Averaged Collisional & Disk Luminosity

The disk luminosity $L_{\rm d}$ is dependent on $M_\bullet$, α, and $\dot{M}_{\rm d}$, and the time-averaged collisional luminosity $L_{\rm c}$ is the product of the $\mathcal{R}_{\rm c}$ and $|\Delta\mathcal{E}|$. Thus both luminosities are different when any of the parameters are altered, Figure 9.8.

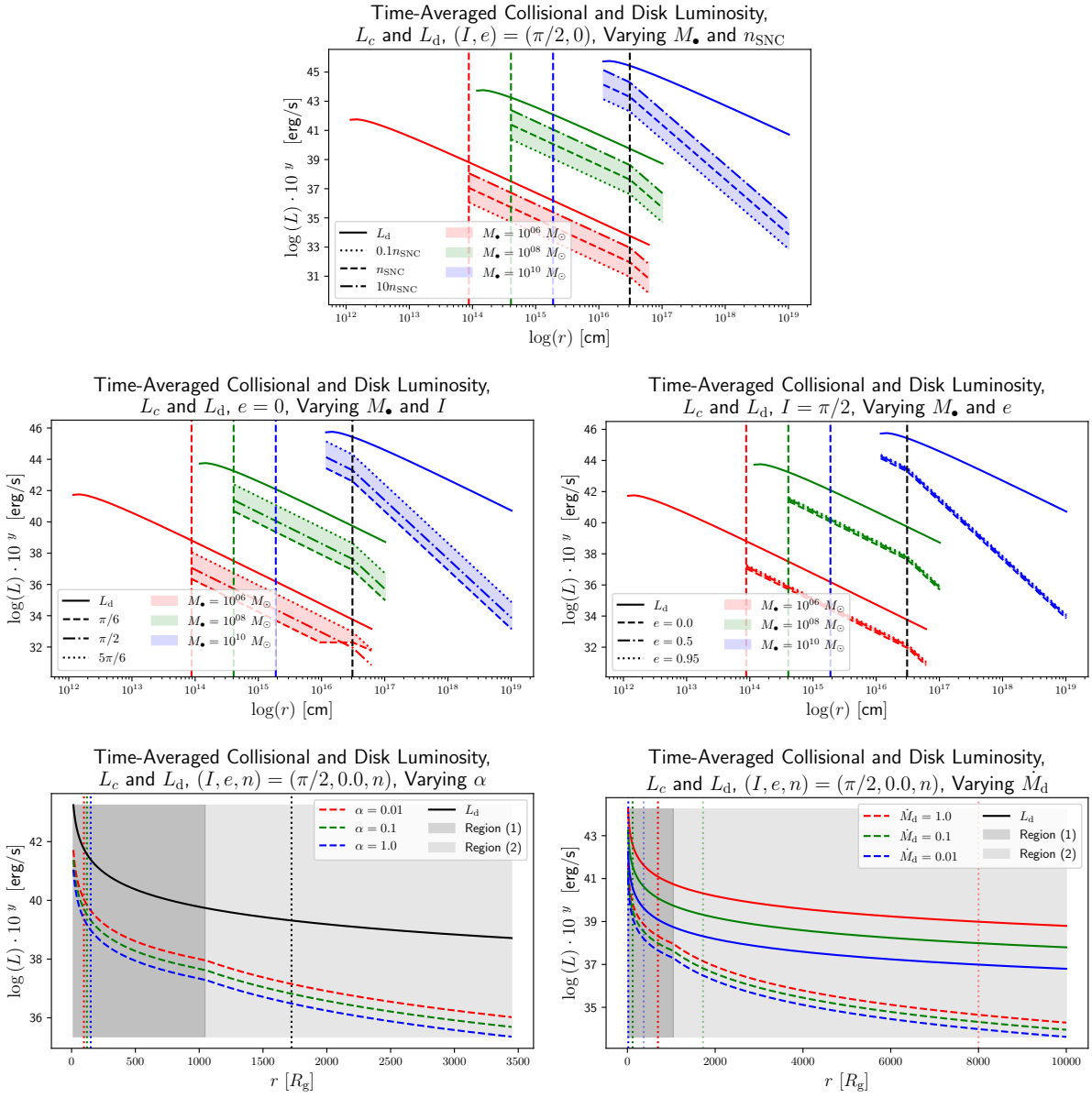

Figure 9.8: The time-averaged collisional luminosity L_c (solid line) and accretion disk surface temperature L_d (shaded colours) plotted against each other while varying $M_\bullet$ (first, second, and third panel), α (fourth panel), and $\dot{M}_d$ (fifth panel). The vertical lines indicate the disk's regional boundaries (dotted), r_{ab} (darker) and r_{bc} (lighter), and the SNC regional boundaries (dashed), r_1 (darker) and r_2 (lighter), where region (1) (dark-gray) is bounded by r_1 and r_2 and region (2) (light gray) has a lower bound of r_2. When these boundaries change they are assigned a colour, respective of which parameter value is being altered, and are black when the boundary is unaffected by the parameter change. The plotted dashed line represents the $0.1n_{SNC}$, $I = \pi/6$ and $e = 0$, the plotted dash-dotted line represents the n_{SNC}, $I = \pi/2$ and $e = 0.5$, and dotted line represents the $I = 5\pi/6$ and $e = 0.95$, for the different stellar scaling, and orbital inclination angles and eccentricities, respectively. Note that the y-axis is log scaled for all plots, as well as the x-axis when varying $M_\bullet$, and the x-axis is given in unit cm when varying $M_\bullet$ and unit R_g elsewhere.

In each plot $L_{\rm d}$ is displayed as a solid line at the top for easy comparison to $L_{\rm c}$. Throughout each investigation, there was no parameter that could be changed in a way that brought the collisional luminosity to a greater value than the surface of the accretion disk.

While keeping $M_\bullet$ at our fiducial value, we allow $n_{\rm SNC}$, I, and e to vary. For clarity, when altering α and $\dot{M}_{\rm d}$ the impactor is assumed to be striking the disk face-on ($I = \pi/2$) on a circular orbit ($e = 0$), and the profile of the SNC is left at its fiducial value.

When varying $M_\bullet$ it was found that larger massed SMBHs increased the luminosities of the disk and the collision. The brightest time-averaged collisions were found to occur when an impactor on a retrograde circular orbit struck the disk surrounding a $10^{10} M_\odot$ massed BH, and when the stellar population was scaled by 10 for the same SMBH. While the dimmest time-averaged collisions were when an impactor on a circular orbit struck the disk face-on while orbiting a $10^6 M_\odot$ massed BH.

When the value of α is altered $L_{\rm d}$ (black curve) is unaffected, and the collisional luminosity is reduced as α is increased. As with the change in orbital energy $|\Delta\mathcal{E}(r)|$, a smaller α and a larger $\dot{M}_{\rm d}$ results in a greater collisional luminosity, where the disk luminosity also decreases with $\dot{M}_{\rm d}$. The change in L_c is comparable when altering the accretion dynamics of the disk, and these parameters appear to have a far weaker effect than the mass of the SMBH does on producing time-averaged flares.

Thus, an accreting $10^{10} M_\odot$ SMBH with accretion parameters of $\alpha \sim 0.01$ and $\dot{M}_{\rm d}$ is surrounded by a $10 n_{\rm SNC}$ SNC whose stars are striking the accretion disk on circular retrograde orbits should create the right scenario for the time-averaged collisional luminosity to be comparable to the disk's surface luminosity.

9.3.6 Transit Time

The transit time $t_{\rm transit}$ for an impactor orbiting differing values of $M_\bullet$, α, and $\dot{M}_{\rm d}$ at $r = 500\ R_{\rm g}$ is given in table 9.3. Larger values of α and smaller values of $\dot{M}_{\rm d}$ both

I	$M_\bullet$			α			$\dot{M}_{\rm d}$		
rad	$10^6 M_\odot$ min	$10^8 M_\odot$ hrs	$10^{10} M_\odot$ weeks	0.01 hrs	0.1 hrs	1 hrs	0.01 hrs	0.1 hrs	1 days
$\pi/6$	58.4	38.6	14	48.6	38.6	30.7	23.1	38.6	13.5
$\pi/4$	41.3	27.3	10	34.4	27.3	21.7	16.3	27.3	9.5
$\pi/3$	33.7	22.3	8.2	28.1	22.3	17.7	13.3	22.3	7.8
$\pi/2$	29.2	19.3	7.1	24.3	19.3	15.4	11.5	19.3	6.7
$2\pi/3$	33.7	22.3	8.2	28.1	22.3	17.7	13.3	22.3	7.8
$3\pi/4$	41.3	27.3	10	34.4	27.3	21.7	16.3	27.3	9.5
$5\pi/6$	58.4	38.6	14	48.6	38.6	30.7	23.1	38.6	13.5

Table 9.3: When one parameters is altered the other two take on their fiducial value, i.e. $M_\bullet = 10^8\ M_\odot$, $\alpha = 0.1$, and $\dot{M}_{\rm d} = 0.1$.

decrease the transit time of an impactor. Conversely, more massive SMBHs increase the transit time, and for all cases the quickest transit times occur when a star has a face-on ($I = \pi/2$) collision with an accretion disk, and its journey lengthens as it's inclination angle deviates from this value.

9.3.7 Impactor Mass Loss & Gain

The amount of mass lost or gained by a YREC impactor is modelled in Figure 9.9, for a SMBH of mass $M_\bullet = 10^{10} M_\odot$, $\alpha = 0.1$, and $\dot{M}_{\rm d} = 0.1 \dot{M}_{\rm Edd}$. This collisional model assumes that an impactor strikes the disk with an inclination of $I = \pi/2$, relative to the disk, and does not consider the star's transit through the disk. It simply compares the mid-plane surface density of the disk at some radial position r to the column density of the impactor to determine how much star matter is stripped off by the more dense disk and how much of the disk material is pushed out of the disk by the star (see §5.1). The mass loss is greatest at small radii within region (b) of the accretion disk, and decreases as r increases. The mass added to the impactor is always greater than what is stripped

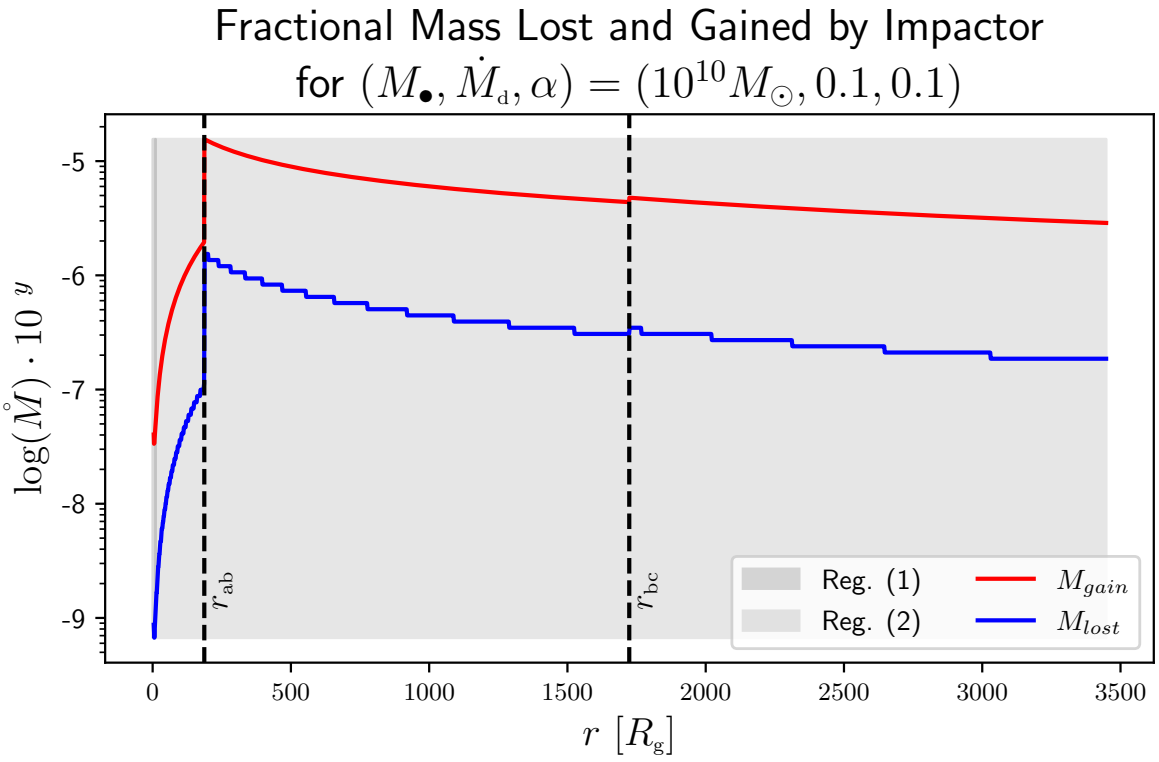

Figure 9.9: The fractional amount of mass lost (blue) and mass gained (red) by a YREC modelled impactor colliding with the disk at different r away from the SMBH. It is assumed that $M_\bullet = 10^{10} M_\odot$, $\alpha = 0.1$, and $\dot{M}_\mathrm{d} = 0.1 \dot{M}_\mathrm{Edd}$.

from it, but this plot does not take into account the escape velocity of the stripped star nor does it consider the temperature of the added gas. As discussed in §5.2 the disk gas that is pushed from the star is shock heated and is mostly too energetic to remain bound to the impactor after its emergence.

9.4 Final Attempt

The previous alteration of various parameters did not yield a situation where the time-averaged collisional luminosity outshone the disk's luminosity, i.e., $L_\mathrm{c} < L_\mathrm{d}$ for all r. Thus, to determine what would theoretically be needed to have $L_\mathrm{c} > L_\mathrm{d}$ these parameters were taken to values that may not be in accordance with the observational evidence of AGNs and the SMBH environment. Initially, scaling the stellar number density profile

by 10^6 gave $L_{\rm c} > L_{\rm d}$ for $r \leq 1000 R_{\rm g}$. Decreasing the disk's mass accretion rate, $\dot{M}_{\rm d}$, and viscosity parameter α, while increasing the impactors' orbital eccentricity and inclination, allowed for the scale of $n_{\rm SNC}$ to be brought down while keeping $L_{\rm c} \geq L_{\rm d}$ (Figure 9.10).

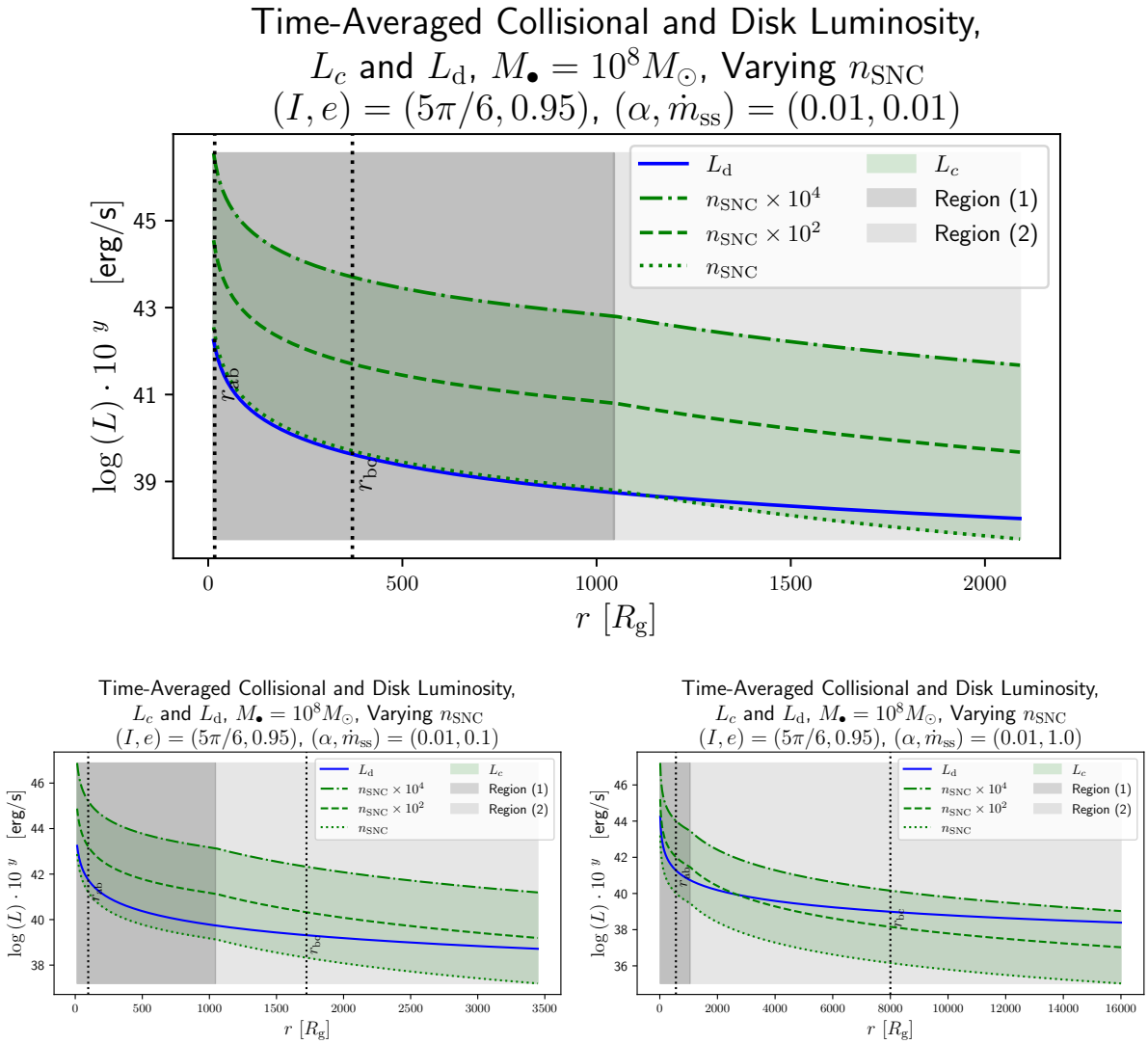

Figure 9.10: Disk's Luminosity (blue) compared to time-averaged collisional luminosity (green). The impactors follow retrograde elliptical orbits that orbit a SMBH of mass $M_\bullet = 10^8 M_\odot$. The disk has a viscosity of $\alpha = 0.01$ and a mass accretion rate of $\dot{M}_{\rm d} = 0.01 M_{\rm Edd}$ (fist panel), $\dot{M}_{\rm d} = 0.1 M_{\rm Edd}$ (second panel), and $\dot{M}_{\rm d} = M_{\rm Edd}$ (third panel). The stellar number density of the SNC has been multiplied by 10^4 (dash-dotted line), 10^2 (dashed line), and 1 (dotted line). The disk's regional boundaries $r_{\rm ab}$ and $r_{\rm bc}$ are indicated by the dotted vertical lines, and the SNC regions (1) and (2) are indicated by the gray shaded regions.

For all the different values of $\dot{M}_{\rm d}$ and all r, $L_{\rm c} > L_{\rm d}$ when $n_{\rm SNC} \geq n_{\rm SNC} \times 10^4$.

Interestingly, when $\dot{M}_{\rm d} = 0.01\dot{M}_{\rm Edd}$ $L_{\rm c}$ is comparable to $L_{\rm d}$ for $r \lesssim 1000R_{\rm g}$ when the number density profile of the stellar nuclear cluster is not altered.

9.5 Summary

The intention of this chapter was to determine how the models and the phenomena of star-disk collisions were affected when the parameters defining the SMBH ($M_\bullet$), accretion disk (α and $\dot{M}_{\rm d}$), SNC ($n_{\rm SNC}$), and impactors ($M_\star$, $R_\star$, I, and e) were altered.

When it comes to the SMBH and accretion disk parameters, $M_\bullet$, α, and $\dot{M}_{\rm d}$, it is found that $M_\bullet$ is the most influential quantity. Throughout this paper the impact location has been given in radial units of $R_{\rm g}$, which becomes ambiguous when the SMBH mass is altered. Larger $M_\bullet$ results in larger $R_{\rm g}$, so radii are given in units of cm to see how things change in real space.

The distribution of stars in the SNC is only dependent on $M_\bullet$, namely the inner boundary r_1 defining the radial extent of the starless core which increases as $M_\bullet$ increases. While the outer boundary r_2 is unchanging in real space, it appears to change when viewed in units of $R_{\rm g}$. The accretion disk regional boundary $r_{\rm bc} \propto \dot{m}_{\rm ss}^{2/3}$ so it is unaffected by a change in $M_\bullet$, however $r_{\rm ab}$ is affected such that region (a) is larger and region (b) is smaller when $M_\bullet$ is larger.

Larger $M_\bullet$ values increase $H_{\rm d}$, $t_{\rm transit}$, $\Delta\mathcal{E}$ and decreases $\rho_{\rm d}$, $\Delta T_c(r)$, $v_{\rm rel}$, L_c, $L_{\rm d}$. The change in $\Delta T_c(r)$ is ambiguous. For the most part, the average time between collisions is the same at any given radii. However, the spatial extent of the SNC core grows with $M_\bullet$ and at sufficiently small r there are fewer stars contained within the space to average out $\Delta T_c(r)$ causing it to be longer when compared with other values of $M_\bullet$ at these r.

The $\dot{M}_{\rm d}$ and α parameters are directly related to the accretion flow, and have opposite effects on the various star-disk properties. In other words, an increase in α is inversely proportional to an increase in $\dot{M}_{\rm d}$. As the viscosity parameter increases the accretion disk

becomes thinner and less dense, thus an impacting star interacts with less matter, travels through the disk quicker, and experiences a smaller change in its orbital energy which results in L_c decreasing. It also slightly changes the value of $r_{\rm ab}$ causing the disk's regions (a) and (b) to be larger and smaller, with an larger value of α. Conversely, an increase in the mass accretion rate causes the disk to become denser and thicker. Disks with larger $\dot{M}_{\rm d}$ are denser and thicker causing transiting stars to interact with more matter for a longer time, increase their orbital energy loss, and create brighter L_c. Furthermore, the $L_{\rm d}$ is proportional to the mass accretion rate and is higher when the SMBH is able to accrete matter more efficiently. Finally, both $r_{\rm ab}$ and $r_{\rm bc}$ take on larger values when $\dot{M}_{\rm d}$ increases, however the effect is stronger in $r_{\rm bc}$.

Scaling the amplitude of $n_{\rm SNC}$ by an order of magnitude simply increases or decreases the amount of stars within the SNC by a factor of ten. When the amplitude of $n_{\rm SNC}$ is multiplied by 10 there is a greater number of stars and thus more impacts of the disk, which trivially increases $\mathcal{R}_c$ and decreases $\Delta T_c(r)$. This higher rate of star-disk collisions, or less time between said collisions, also causes the L_c to be brighter, but it still remains dimmer than $L_{\rm d}$. The amplitude scaling of $n_{\rm SNC}$ ultimately scales the rate, the average time between collisions, and the time-averaged collisional luminosity by an order of magnitude, the same scaling as $n_{\rm SNC}$.

None of the other star-disk collisional phenomena are dependent on the total number of stars with a given region, but are instead dependent on the individual stellar parameters $R_\star$, $M_\star$, I, e. The physical properties of the star, $M_\star$ and $R_\star$, have a direct effect on the physical size of the SNC core, since r_1 is a scalar multiple of the tidal radius r_t. Thus, when the stellar constituents of the SNC are switched for more massive and larger MS spectral classes the SNC core has a larger radial extent, and when the stars are less massive and smaller MS spectral classes the SNC core has a smaller radial extent.

An impactor's orbital inclination and eccentricity influence its experienced $v_{\rm rel}$, which

shortens or lengthens $t_{\rm transit}$, and affects $\Delta\mathcal{E}$ during the disk passage, thus affecting L_c. The relative velocity is fastest for impactors striking the disk on retrograde or highly elliptical orbits, and slowest for those on circular or prograde orbits. This is a result of the calculation of $v_{\rm rel}$, where the disk's z-velocity component is zero. When calculating $v_{\rm rel}$ impactors on retrograde orbits have negative velocity components that result in a sum and impactors on prograde orbits have positive velocity components that result in a difference. Impactors with highly elliptical orbits have most of their velocity in the z direction, which is unaltered by the disk's velocity, and those with circular orbits have most of their velocity in the x, y directions, which is greatly affected by the disk's velocity.

Even though as $e \to 1$ the orbital velocity increases, and thus $t_{\rm transit}$ decreases, we focus on the effects of the orbital inclination angle I. Impactors are able to pass through the disk in the shortest amount of time when they strike the disk face-on, and their time spent inside the disk lengthens as their impact inclination, relative to the disk, deviates from this angle. There is no notable difference in $t_{\rm transit}$ between retrograde and prograde orbits.

Like $v_{\rm rel}$ the orbital energy $\Delta\mathcal{E}$ lost from an impactor is more affected by its value of I than its e value. Changing the value of e results in a negligible change in the loss of orbital energy, where highly eccentric orbits lose more energy than circular orbits, since the calculation of $\Delta\mathcal{E}$ involves the change in semimajor axis which is a larger difference for more eccentric orbits. Whereas impactors on retrograde orbits have a greater loss in $\Delta\mathcal{E}$ than those on prograde orbits, since a stronger $F_{\rm drag}$ is generated for retrograde orbits with larger $v_{\rm rel}$.

The time-averaged collisional luminosity is the product of $\mathcal{R}_c$ and $\Delta\mathcal{E}$, thus, for the same reasons as given for the changes in orbital energy, L_c is more affected by I than e. A collection of impactors striking the disk with retrograde or highly eccentric orbits will create a higher L_c than those striking the disk with prograde or circular orbits.

10 Conclusion

This thesis aims to investigate how much of an effect stars colliding with accretion disks orbiting SMBH in AGN have on quasar variability. We assume a SMBH mass of $M_\bullet = 10^8 M_\odot$ and use the unit $R_g = 2GM_\bullet/c^2 \sim 3 \times 10^{13}$ cm to express the radial distance.

The upper outer atmosphere of an impactor has an integrated surface density that is less than that of the accretion disk's surface density. This difference in densities results in some of the atmosphere being stripped off of the star as it transits the disk. It was found that when a solar mass impactor struck the disk the greatest amount of mass that was stripped from the star was only $\sim 6 \times 10^{-6} M_\star$ (see §5.1 for a detailed calculation).

As mass is stripped from the impactor its radial extent decreases and the remaining star is able to push matter out of the disk. We refer to this matter as mass gained by the star, which for all r considered is $\sim 10 - 100$ times greater than the amount of mass lost to the disk. However, this matter is shock heated to temperatures that are greater than the escape temperature of the emerging impactor and, even though it was not explicitly calculated, most of this matter is assumed to fall back onto the disk and not remain bound to the star.

A three-dimensional model is used to describe the structure of the star-disk collisions. The thin circular accretion disk is assumed to be situated on the xy-plane at $z = 0$ and the stars populating the SNC have specified orbital elements, including their eccentricities e, inclination angles I, relative to the disk plane, and semimajor axes a, derived from their radial impact location.

We define the relative velocity $v_{\rm rel}$ as the difference between the stellar velocity $v_\star$ and the disk velocity $v_{\rm d}$, and we define prograde and retrograde as impactors striking the disk with orbital inclination angles of $I < \pi/2$ and $I > \pi/2$ respectively. The relative velocity is greatest for impactors following circular retrograde orbits and least for those on circular prograde orbits. Differing the eccentricity of an impactor's orbit has far less of an effect

on $v_{\rm rel}$ than altering its orbital inclination, but $v_{\rm rel}$ is greater for more elliptical orbits.

The disk material generates a drag force that is experienced by a transiting impactor, that effectively slows the star and reduces its orbital energy. Like the relative velocity more energy is lost for circular retrograde orbits than for circular prograde orbits, and a range of eccentricity has less of an effect on the change in orbital energy than a range of inclination angles.

This orbital energy can be combined with the average rate of collisions to be reinterpreted as a time-average collisional luminosity and compared to the surface luminosity of the disk. Unfortunately, no matter the orbital eccentricity or inclination, impactors colliding with the disk are not able to reach values that bring them higher than $L_{\rm d}$.

The thickness of the disk is measured along the z-axis of a cylindrical coordinate system, and the position of an impactor with respect to time is measured along the same axis. It is found that impactors striking the disk with $I = \pi/2$ traverse the disk fastest, and once they emerge an impactor striking the disk with $I = \pi/6$ or $I = 5\pi/6$ would be at the disk's midplane. Although the drag force is assumed to be a deceleration term that factors into an impactor's position, it does not make a notable difference between prograde and retrograde orbits.

A region of space within the accretion disk, referred to as the "shock tunnel" in this paper, is carved out by an impactor as it proceeds through its transit and shock heats the gaseous disk material. The geometry of the shock tunnel is provided in two reference frames (Figures 7.2 and 7.3), where an observer is situated within the disk looking towards the central SMBH along the y-axis.

An impactor traversing the disk can reach speeds of $\sim 0.1c$ when on an unbound parabolic orbit, however this speed is reduced as the impactor loses orbital energy and becomes bound to the SMBH after a single pass. For this speed the time that an impactor is within the accretion disk is $t_{\rm transit} \sim 0.2$ days and is only slightly longer for bound

circular orbits with a time of $t_{\rm transit} \sim 0.27$ days.

An impactor travels through the disk at a speed greater than the sound speed of the gas, thereby shock heating the disk material to high temperatures. This shock heated gas releases photons that can be observed as a bright X-ray flare when the impactor enters the disk, followed by emission of infrared and visual light from the photons being absorbed and re-emitted by the disk material, and ending with fading black-body emission long after the star has emerged from the disk.

Depending on the impact location of the star-disk collision, the shock heated gas releases photons that either diffuse by randomly-walking or travel with a sound wave to reach the surface of the disk where their emission is observable. Whichever process achieves this in the least amount of time is the determining factor. The diffusive process is fastest for $100R_{\rm g}$ yielding $t_{\rm diff} \sim 0.2$ hrs, and the sound-speed is fastest for $500R_{\rm g}$ and $1000R_{\rm g}$ which yield $t_{s,R_0} \sim 1.65$ hrs and $t_{s,R_0} \sim 5.44$ hrs, respectively.

The shock tunnel created by an impactor is assumed to radially expand and sweep up un-shocked gas until it reaches a point where the un-shocked gas has effectively stopped the expansion of the shocked gas. We define this maximum radius of radial expansion as $R_{\rm stall}$, and for the fiducial radial impactor locations, $r = (100, 500, 2000)R_{\rm g}$, the expansion stops at $R_{\rm stall} \sim (9.7, 8.5, 8.3) \times 10^{11}$ cm.

Furthermore, we assume that as the photons from the shock travel outwards, the shocked gas cools until it reaches a temperature of $\sim 1\%$ above the disk surface temperature. We define this time as the thermal time $t_{1\%}$, and for the fiducial radial impactor locations the amount of time required is worked out to be $t_{1\%} \sim (2.47 \text{ yrs}, 86 \text{ days}, 159 \text{ days})$. The incredibly long time span at $100R_{\rm g}$ implies that photons travelling at the sound speed cool the shock tunnel faster than those travelling with the diffusion timescale.

The times that it takes for the photons released by the shocked gas to reach the disk's front (entrance side) and back (emergence side) surfaces are used to estimate an emission

profile, with respect to time, of an impactor striking the disk at the fiducial radial impact locations. The emission profiles for each side are similar with a time-lag between the two, where the front side emission occurs before the back side emission. The profiles show an initial flare when the star enters (emerges) from the disk, that quickly dims as the star goes deeper into (moves away from) the disk.

An investigation was conducted to determine which parameters, when altered, could yield more dramatic results of star-disk collisions. The parameters altered govern the SMBH and its accretion disk ($M_\bullet$, α, and $\dot{M}_{\rm d}$), and the stellar nuclear cluster ($n_{\rm SNC}$, I, e, and the main sequence spectral class of the impactors).

Since the starless core of the SNC is dependent on r_t, an increase (decrease) of $M_\bullet$ increases (decreases) the extent of the core while reducing (increasing) the extent of region (1). Scaling the amplitude of $n_{\rm SNC}$ to higher (lower) values yielded longer (shorter) times for $\Delta T_c(r)$ and quicker (slower) values of $\mathcal{R}_c$. Stars on highly elliptical orbits, or those that struck the disk with retrograde inclination angles, increased the values of $v_{\rm rel}$, $\Delta\mathcal{E}$, and L_c

Higher (lower) values of α resulted in higher (lower) values of $H_{\rm d}$ and $L_{\rm d}$ while producing lower (higher) values of $\rho_{\rm d}$ and L_c Higher (lower) values of $\dot{M}_{\rm d}$ resulted in higher (lower) values of $\rho_{\rm d}$ and $H_{\rm d}$ Larger (smaller) values of $M_\bullet$ resulted in larger (smaller) values of $H_{\rm d}$, $\rho_{\rm d}$, $\Delta\mathcal{E}$, L_c, $L_{\rm d}$, and $v_{\rm rel}$.

However, of the parameters altered, there were none that could bring the time-averaged collisional luminosity higher than the disk's surface luminosity, i.e. $L_c < L_{\rm d}$. Thus, a final calculation was performed where the impactors on highly elliptical orbits, $e = 0.95$, struck the disk at highly retrograde inclination angles, $I = 5\pi/6$, where $\alpha = 0.01$, $\dot{M}_{\rm d} = (0.01, 0.1, 1.0)\dot{M}_{\rm Edd}$ and $M_\bullet = 10^8 M_\odot$, which resulted in $L_{\rm c} > L_{\rm d}$ for all r when $n_{\rm SNC} = n_{\rm SNC} \times 10^4$.

To summarize, the main findings of this investigation are:

1. When an impactor has completed its transit of the disk only a negligible amount of its mass ($\sim 6 \times 10^{-6} M_\star$ at most) is stripped off by the accretion disk. Although some of the disk material is pushed out of the disk by the emerging impactor most of it is assumed to be unbound to the star since the material is shock heated to temperature greater than the escape temperature of the star.

2. The gaseous disk material contributes to a drag force felt by the transiting impactor, that effectively reduces its orbital energy. The drag force is dependent on the relative velocity of the impactor which is greatest for retrograde and highly elliptical orbits.

3. The shock tunnel, a region of space carved out of the accretion disk by an impactor, has nearly the same radius as the impactor and is depicted in two reference frames. Depending on the chosen reference frame, the inclination of the tunnel with respect to the plane of the disk is affected by the orbital inclination of the impactor and its relative velocity, or just its orbital inclination.

4. A time-dependent emission profile of a transiting impactor is modelled for different radial impact locations, which determines the process by which the photons make their way to both surfaces of the disk where they can be observed. For both sides of the disk an initial bright flare is preceded by a very quick increase in luminosity and followed by a drawn out decreases in luminosity before reaching the luminosity of the disk.

5. Altering the parameters of the accretion disk, supermassive black hole, steller nuclear cluster, and impactor within accepted ranges found within the literature revealed that star-disk collisions are unable to match the accretion luminosity of the disk. However, when the number density profile of the stellar nuclear cluster is scaled to values that may be outside of the literature regarding AGN and the SMBH environment, the time-averaged collisional luminosity becomes brighter than the disk's

surface luminosity.

Bibliography

Bañados, E., Venemans, B. P., Mazzucchelli, C., et al. 2018, Nature, 553, 473

Bellovary, J. M., Mac Low, M.-M., McKernan, B., & Ford, K. E. S. 2016, Astrophys. J. Lett., 819, 5

Cho, H. & Narayan, R. 2022, Astrophys. J., 932, 97

Dai, L. J., Fuerst, S. V., & Blandford, R. 2010, MNRAS, 402, 1614

del Valle, M. V. & Pohl, M. 2018, Astrophys. J., 864, 14

Demarque, P., Guenther, D. B., Li, L. H., et al. 2008, Astrophysics & Space Science, 316, 31

Derishev, E. 2018, Astronomy Reports, 62, 868, presented at The Third Zeldovich meeting, April 23-27, 2018, Minsk, Belarus

Event Horizon Telescope Collaboration, Akiyama, K., Alberdi, A., et al. 2022, Astrophys. J. Lett., 930, L12

—. 2019a, Astrophys. J. Lett., 875, L5

—. 2019b, Astrophys. J. Lett., 875, L6

Fabj, G., Nasim, S. S., Caban, F., et al. 2020, MNRAS, 499, 2608

Filiz Ak, N., Brandt, W. N., Hall, P. B., et al. 2013, Astrophys. J., 777, 29

Frank, J., King, A., & Raine, D. J. 2002, Accretion Power in Astrophysics: Third Edition, 3rd edn. (Cambridge University Press)

Gilbaum, S. & Stone, N. C. 2022, Astrophys. J., 928, 26

Goicovic, F. G., Cuadra, J., Sesana, A., et al. 2016, MNRAS, 455, 1989

Goodman, J. 2003, MNRAS, 339, 937

Goodman, J. & Tan, J. C. 2004, Astrophys. J., 608, 108

Grier, C. J., Hall, P. B., Brandt, W. N., et al. 2015, Astrophys. J., 806, 15

Habets, G. M. H. J. & Heintze, J. R. W. 1981, Astron. Astrophys. Suppl. Ser., 46, 193

Hall, P. B., Sarrouh, G. T., & Horne, K. 2018, Astrophys. J., 854, 10

Hopkins, P. F., Torrey, P., Faucher-Giguère, C.-A., et al. 2016, MNRAS, 458, 816

Hu, H., Inayoshi, K., Haiman, Z., et al. 2022, Astrophys. J., 935, 140

Huré, J.-M. 1998, Astron. Astrophys., 337, 625

Jermyn, A. S., Dittman, A. J., McKernan, B., et al. 2022, Astrophys. J., 929, 9

Kelly, B. C., Bechtold, J., & Siemiginowska, A. 2009, Astrophys. J., 698, 895

Kieffer, T. F. & Bogdanović, T. 2016, Astrophys. J., 823, 155

King, A. 2020, MNRAS, 493, L120

King, A. R., Pringle, J. E., & Livio, M. 2007, MNRAS, 376, 1740

Kormendy, J. & Ho, L. C. 2013, Annu. Rev. Astron. Astrophys., 51, 511

Lanzuisi, G., Perna, M., Comastri, A., et al. 2016, Astron. Astrophys., 590, A77

Lauer, T. R., Ajhar, E. A., Byun, Y. I., et al. 1995, Astrophys. J., 110, 2622

Ledrew, G. 2001, Journal of the Royal Astronomical Society of Canada, 95, 32

MacLeod, M. & Lin, D. N. C. 2020, Astrophys. J., 889, 13

McKernan, B., Ford, K. E. S., Cantiello, M., et al. 2021, manuscript submitted for publication

McKernan, B., Ford, K. E. S., O'Shaugnessy, R., & Wysocki, D. 2020, MNRAS, 494, 1203

Miniutti, G., Saxton, R. D., Giustini, M., et al. 2019, Nature, 573, 381

Nayakshin, S., Cuadra, J., & Sunyaev, R. 2004, Astron. Astrophys., 413, 173

Netzer, H. 2013, The Physics and Evolution of Active Galactic Nuclei (USA: Cambridge University Press)

Neumayer, N., Seth, A., & Böker, T. 2020, Astron. & Astrophys. Rev., 28

Novikov, I. D. & Thorne, K. S. 1973, in Black Holes (Les Astres Occlus), 343–450

Osterbrock, D. E. 1989, Astrophysics of Gaseous Nebulae and Active Galactic Nuclei (USA: University Science Books)

Pan, X., Li, S.-L., Cao, X., et al. 2022, Astrophys. J. Lett., 928, L18

Pariev, V. I. & Colgate, S. A. 2007, Astrophys. J., 658, 114

Perry, J. J. & Williams, R. 1993, MNRAS, 260, 437

Pihajoki, P. 2016, MNRAS, 457, 1145

Pinsonneault, M. H. 1988, PhD thesis, Yale University, Connecticut

Rauch, K. P. 1995, MNRAS, 275, 628

Rogerson, J. A., Hall, P. B., Ahmed, N. S., et al. 2018, Astrophys. J., 862, 23

Schindler, J.-T., Fan, X., Novak, M., et al. 2021, Astrophys. J., 906, 12

Shakura, N. I. & Sunyaev, R. A. 1973, in X- and Gamma-Ray Astronomy, ed. H. Bradt & R. Giacconi, Vol. 55, 155

Smith, K. L., Mushotzky, R. F., Boyd, P. T., et al. 2018, Astrophys. J., 857, 141

Sun, L., Jiang, N., Wang, T., et al. 2020, Astrophys. J., 898, 129

Trakhtenbrot, B. 2021, in Nuclear Activity in Galaxies Across Cosmic Time, ed. M. Pović, P. Marziani, J. Masegosa, H. Netzer, S. H. Negu, & S. B. Tessema, Vol. 356, 261–275

Wang, F., Yang, J., Fan, X., et al. 2021, Astrophys. J. Lett., 907, L1

Wu, J., Jun, H. D., Assef, R. J., et al. 2018, Astrophys. J., 852, 96

Xian, J., Zhang, F., Dou, L., et al. 2021, Astrophys. J. Lett., 921, 8

Zentsova, A. S. 1983, Astrophysics & Space Science, 95, 11

A Accretion Disk's Inner Regional Boundary

Here is a table showing the results of taking $M_\bullet$, α, and $\dot{M}$ to their extremes for the accretion disk's inner regional boundary $r_{\rm ab}$:

$M_\bullet$ $[M_\odot]$	$\dot{M}_{\rm d}$ $[\dot{M}_{\rm Edd}]$	α	$r_{\rm ab}$ $[R_{\rm g}]$
10^6	0.01	0.01	10.79
		0.1	13.44
		1	16.74
	0.1	0.01	62.39
		0.1	77.69
		1	96.74
	1	0.01	360.6
		0.1	449.0
		1	559.1
10^8	0.01	0.01	16.74
		0.1	20.84
		1	25.95
	0.1	0.01	96.74
		0.1	120.5
		1	150.0
	1	0.01	559.1
		0.1	696.2
		1	866.9
10^{10}	0.01	0.01	25.95
		0.1	32.32
		1	40.24
	0.1	0.01	150.0
		0.1	186.8
		1	232.6
	1	0.01	866.9
		0.1	1079
		1	1344

Table A.1: Inner accretion disk regional boundary $r_{\rm ab}$ in units of $R_{\rm g}$ for differing values of $M_\bullet$, α, and $\dot{M}_{\rm d}$